Crystal nonlinear optics: with SNLO examples

2nd edition

Arlee V. Smith

Arlee V. Smith, PhD
AS-Photonics, LLC
Albuquerque, New Mexico 87109, USA
arlee.smith@as-photonics.com

Published by: AS-Photonics
Albuquerque, NM, USA

ver. 3.5.20
ISBN 978-0-69-205678-3

Cover art is a $|d_{\text{eff}}|$ surface with phase match loci for the crystal BIBO. It was generated using the Bmix function in the matlab version of SNLO.

Preface to the Second Edition

Chapter 9 on optical parametric generation (OPG) is entirely new in this second edition. It is based on modeling with two SNLO functions PW-mix-BB for plane waves and OPG for diffractive waves. The plane wave modeling might be appropriate for OPG in a waveguide. The OPG function is included in the Matlab version of SNLO but not in the free version where it runs too slowly to be practical.

Other changes from the first edition are minor, consisting of several corrections of typographical errors and occasional attempts to improve the presentation clarity.

Preface to the First Edition

My goal in writing this book is to provide an intuitive understanding of the principles that are important in designing crystal nonlinear optical devices. I explain how the complicating effects of dispersion, diffraction, birefringence, spectra, and three dimensional pulse envelopes, can all strongly influence the performance of real devices. Over one hundred examples, based on the SNLO modeling software, are presented to illustrate physical concepts. These examples provide guidance for numerical experiments to help develop intuition. They also serve as starting points for designing real devices and predicting their performance.

The book is also intended as a users guide to the crystal nonlinear optics software SNLO. It is essential to understand the theory underlying the numerical models, and this book is also general text on second-order crystal nonlinear optics. The theory should aid readers in developing their own models, as well as documenting the capabilities and limitations of the SNLO models. It is my intent that SNLO should contain the best information on crystal properties so this book contains few specific crystal properties.

I try to keep the mathematics at the undergraduate level to emphasize physical intuition, sometimes at the expense of mathematical elegance. This is not a broad brush treatment. Judging from the number of pages, I consider details to be important. SI units are used exclusively, and I have tried diligently to maintain a consistent and standard nomenclature throughout. Most of the important quantities are defined in the Introduction.

The interaction of three monochromatic plane-waves in a nonlinear crystal is treated in several text books on nonlinear optics. In particular, Sutherland's *Handbook of nonlinear optics* has an extensive collection of useful analytical solutions that apply to a variety of specific cases. I will describe only a few such analytic solutions, emphasizing qualitative understanding. Quantitative evaluations will be from numerically integrating the mixing equations. Not only is this approach often faster, it is far more general because there are few restrictions on parameters such as linear absorption, phase mismatch, etc.

This book goes far beyond the usual introductory discussion of plane wave, monochromatic, low conversion mixing to include extensive discussions of mixing with realistic beams and pulses, including mixing in optical cavities. I include only parametric processes, defined as frequency mixing processes that do not involve significant energy transfer to the crystal. Based on the many questions I receive about SNLO, one of the more confusing topics in crystal nonlinear optics is the connection between walk offs and acceptance bands. These are identical concepts described in the alternative languages of space or time on the one hand, or their Fourier transforms of k-space or frequency on the other. I will show how to relate the two, but will emphasize the more intuitive space/time picture. This contrasts with most introductions to nonlinear optics that emphasize the k/ω description. I also point out the strong symmetry between spatial and temporal effects, and show how this equivalence can be used to translate understanding from spatial to temporal effects and *vice versa*.

Despite the occasional use of the word photon, I do not discuss quantum optics in any depth - it is outside my area of expertise, and it is a broad enough topic to require another book the size of this one. However, the ideas presented here are often essential in understanding the quantum optics of devices based on second order optical nonlinearity.

Because of the vast number of papers published over the last forty years on the topic of crystal nonlinear optics, comprehensive citations are impossible. I make no attempt to cite all the important original papers on a topic. I try to cite some of the classic papers, but mostly I cite recent papers that can serve as recent entry points to the literature.

I owe many thanks to Binh Do and Xuan Liu for reviewing the text of this book, to Jesse Smith for help with typesetting and figures, and to my Sandia colleagues Darrell Armstrong, W. J. (Joe) Alford, T.D. Raymond, Binh Do, Michael V. Pack, Russell Gehr, Mark C. Phillips, and Steven Wilkinson for numerous collaborations and discussions over the years. I also owe thanks to long time non-Sandia collaborators Mark Bowers and Gunnar Arisholm, and to my thesis advisor John F. Ward.

Arlee V. Smith *Albuquerque, New Mexico, USA*

Contents

Preface to the Second Edition **iii**

Preface to the First Edition **v**

1 Introduction **1**
- 1.1 Maxwell's equations in linear medium 1
- 1.2 Variable names and units 3
- 1.3 Conversion factors & definitions 3
- 1.4 Definition of mixing strength $S_\circ$ 4
- 1.5 Gaussian profiles 5
  - 1.5.1 $S_M/\mathrm{e}^{\,2}$ definitions 5
  - 1.5.2 FWHM definitions 6
  - 1.5.3 Supergaussians 7
  - 1.5.4 Sech squared pulses 7
  - 1.5.5 Rayleigh and dispersion lengths 7
- 1.6 Field expansions 8
  - 1.6.1 Fourier transform definitions 8
  - 1.6.2 Fourier transform properties 9
- 1.7 Abbreviations 10

2 Linear crystal optics for monochromatic plane waves **11**
- 2.1 A geometrical description 13
  - 2.1.1 Relating $\boldsymbol{D}$ to $\boldsymbol{E}$ 13

2.1.2 Finding the eigenpolarizations 15
2.1.3 Optical axes of biaxial crystals 16
2.1.4 Propagation outside the principal planes 17
2.1.5 Poynting vector walk off 18
2.1.6 Hi and lo index surfaces 19
2.1.7 Uniaxial crystals 19
2.1.8 Isotropic crystals 21
2.2 Mathematics of the geometrical description 22
2.2.1 Finding the D-ellipsoid 22
2.2.2 Defining the eigenpolarizations 25
2.2.3 Finding the optic axes 26
2.2.4 Computing the eigenpolarizations and refractive indices 27
2.2.5 General expression for the walk off angle ρ 30
2.3 Derivations direct from Maxwell's equations 32
2.3.1 Finding the Cartesian components of $\boldsymbol{E}$ and $\boldsymbol{D}$ . . . 32
2.3.2 Finding n_{lo} and n_{hi} 34
2.3.3 Finding the walk off angles 35
2.4 Optical activity 36
2.5 Entering and exiting crystals 37
2.5.1 Refraction angles 37
2.5.2 Electric field reflection and transmission coefficients 39
2.6 Exercises 46

3 Monochromatic, plane-wave mixing 49
3.1 Mixing equations 50
3.1.1 Derivation of mixing equations 50
3.1.2 Energy conservation 56
3.1.3 Manley-Rowe relation 56
3.2 Integrating the mixing equations 57
3.3 Weak mixing 58
3.3.1 Phase matched, two input waves 58
3.3.2 Phase mismatched, two input waves 58
3.4 Intermediate mixing 63
3.4.1 Strong blue wave: Parametric gain 63
3.4.2 Strong red wave 68
3.4.3 Summary of intermediate mixing 70
3.5 Strong mixing 70
3.5.1 Cyclic mixing 71
3.5.2 Photon-balanced mixing 72
3.5.3 Phase evolution 73
3.5.4 Eigenmode mixing 78
3.6 Higher order nonlinear effects 83
3.6.1 Self phase modulation and two-photon absorption . 84

3.6.2 Cross phase modulation and two-photon absorption 86
3.6.3 Stimulated Raman scattering 87
3.6.4 $\boldsymbol{\chi}^{(2)}$:$\boldsymbol{\chi}^{(2)}$ cascade effects 88
3.7 Mixing in waveguides 90
3.7.1 Higher order nonlinearity in waveguides 95
3.8 Exercises 96

4 Phase matching **103**
4.1 Birefringent phase matching 105
4.1.1 Collinear phase matching 105
4.1.2 Uniaxial noncollinear phase matching with fixed k_3 . 111
4.1.3 Uniaxial noncollinear phase matching with fixed k_1 . 115
4.1.4 Biaxial noncollinear phase matching 116
4.1.5 Noncritical phase matching 117
4.2 Quasi phase matching (QPM) 118
4.2.1 General periodic quasi phase matching 119
4.2.2 Periodic modulation of d_{eff} 121
4.2.3 Nonperiodic modulation of d_{eff} 125
4.2.4 Ferroelectric domains 126
4.2.5 Wafer stacking and patterned crystal growth 128
4.2.6 Total internal reflection 130
4.3 Compensated phase matching (CPM) 131
4.4 Wave guide modal phase matching 135
4.5 Photonic lattice phase matching 139
4.6 Acceptance bandwidths 148
4.6.1 Frequency bandwidths 149
4.6.2 Angle bandwidths 154
4.6.3 Crystal tilt tolerance 158
4.6.4 Temperature bandwidth 158
4.7 Temperature tuning 159
4.8 Exercises 160

5 Propagation & mixing equations for structured waves **167**
5.1 Diffractive propagation equations 169
5.1.1 Isotropic crystal 169
5.1.2 Uniaxial crystal 172
5.1.3 Fourier shift rule and birefringent walk off 179
5.1.4 Huygen's construction of birefringent walk off 179
5.1.5 Uniaxial propagator from Maxwell's equations . . . 181
5.1.6 Biaxial crystal 184
5.2 Dispersive propagation equations 185
5.3 Diffractive and dispersive propagation equations 190
5.3.1 In (k_x, k_y, ω) space 190
5.3.2 In (x, y, t) space 191

5.3.3 Uniaxial coefficients A-H . . . 192
5.3.4 Biaxial coefficients A-H . . . 193
5.3.5 Discussion of A-H coefficients . . . 194
5.3.6 Tilted beams . . . 195
5.4 Mixing equations for structured waves . . . 198
5.4.1 Time convolution . . . 199
5.4.2 Angle convolution . . . 202
5.4.3 Time and angle convolution . . . 203
5.5 Integrating the equations . . . 205
5.5.1 Analytical/semi-analytical methods . . . 205
5.5.2 Beam propagation methods . . . 206
5.5.3 Time domain integration . . . 207
5.5.4 Limitations of numerical models . . . 208
5.5.5 Noise simulation . . . 208

6 Mixing temporally structured plane waves 213
6.1 Short pulse/broadband mixing equations . . . 214
6.2 Gaussian pulse propagation . . . 215
6.2.1 Motion of the nonlinear polarization pulse . . . 217
6.3 Short-pulse SHG . . . 218
6.3.1 Group velocity walk off and spectra . . . 218
6.3.2 Group velocity and efficiency . . . 220
6.3.3 Group delay dispersion . . . 222
6.3.4 Strong short-pulse SHG . . . 224
6.4 Chirped-pulse SHG . . . 224
6.5 Short-pulse sum & difference frequency mixing . . . 226
6.5.1 Group velocity effect . . . 227
6.5.2 Triple chirped pulses . . . 227
6.6 Broadband parametric amplification . . . 228
6.6.1 Short pump, weak mixing . . . 229
6.6.2 Short pump, strong mixing . . . 229
6.7 Multimode mixing . . . 229
6.7.1 Sum frequency mixing . . . 230
6.7.2 Parametric amplification . . . 234
6.8 Pulse shaping methods . . . 235
6.9 Short pulse measurement . . . 238
6.10 Self phase modulation . . . 241
6.11 Exercises . . . 242

7 Mixing spatially structured, monochromatic beams 253
7.1 Diffractive mixing equations . . . 254
7.2 Gaussian beam propagation fundamentals . . . 256
7.2.1 Cylindrical focus . . . 256
7.2.2 Spherical focus . . . 257

7.3 Mixing weakly focused beams ($z_R \gg L$) 260
7.3.1 Weak mixing 260
7.3.2 Walk off compensation 267
7.3.3 Shaped and tilted beams 268
7.3.4 Strong mixing 269
7.4 Mixing tightly focused beams ($z_R \sim L$) 273
7.4.1 Weak sum frequency mixing of focused beams 274
7.4.2 Weak difference frequency mixing of focused beams . 280
7.4.3 Beyond Boyd and Kleinman 281
7.4.4 Plane wave simulations of focused beam mixing . . . 287
7.4.5 Intermediate mixing of focused beams 288
7.4.6 Strong mixing of focused beams 290
7.5 Mixing highly structured beams 293
7.5.1 Mixing poor quality beams 293
7.5.2 Imaging 293
7.6 Vector field effects 298
7.7 Beam quality and M^2 299
7.7.1 Gaussian beams 299
7.7.2 Nongaussian beams 300
7.7.3 M^2 for pulsed beams 302
7.8 Exercises 303

8 Mixing spatially and temporally structured beams 311
8.1 Linear propagation 311
8.2 Second harmonic generation 312
8.3 Tilted beams & slanted envelopes 315
8.3.1 Apparent group velocity and GDD 316
8.3.2 Group velocity matched SHG of short, slanted pulses 321
8.3.3 Achromatic SHG of frequency chirped pulses 322
8.3.4 Mixing three short slanted pulses 324
8.3.5 CPOPA 325
8.3.6 Group velocity matched QPM mixing 329
8.3.7 Snell's law of slants 331
8.4 Other group velocity matching methods 333
8.4.1 Birefringent group velocity matching plus QPM . . . 333
8.4.2 Polarization mixed QPM 333
8.4.3 Chirped gratings and pulses 333
8.4.4 Spatial + temporal walk off compensation 333
8.5 Other applications of space/time structure 334
8.5.1 Grenouille 334
8.5.2 Crystal oscilloscope 335
8.6 Exercises 336

9 Optical parametric generation (OPG) 343

9.1 OPG pump threshold estimate . . . 345
9.2 OPG gain bandwidths . . . 347
9.3 OPG numerical modeling . . . 348
9.3.1 Quantum noise simulation . . . 349
9.4 Plane wave, broadband OPG modeling . . . 350
9.4.1 Subthreshold gain vs. temporal walk off . . . 351
9.4.2 Plane wave OPG performance versus $\{\mathcal{R}, \Theta\}$ . . . 354
9.4.3 Time structured pumps . . . 361
9.4.4 Ultra broadband OPG . . . 363
9.5 Diffractive, broadband OPG model . . . 364
9.5.1 Theory of tilt & tune . . . 364
9.5.2 Baseline OPG . . . 367
9.5.3 Long pulse, unseeded OPG, $z_R \approx L$ . . . 368
9.5.4 Long pulse, seeded OPG, $z_R \approx L$ . . . 374
9.5.5 Short pulse, seeded & unseeded OPG, $z_R \approx L$ . . . 379
9.5.6 OPG with birefringent walk off . . . 381
9.6 Back conversion reduction . . . 386
9.6.1 Red wave absorption . . . 386
9.6.2 Multiple crystals with red wave blocking . . . 387
9.7 Practical implementation of OPG . . . 387
9.7.1 Avoiding oscillation . . . 387
9.7.2 Optimum focusing . . . 388
9.7.3 Optimum crystal length . . . 388
9.7.4 Minimizing back conversion . . . 388
9.7.5 Seeding . . . 389
9.7.6 Cascade mixing . . . 389
9.8 Exercises . . . 389

10 Mixing CW monochromatic beams in optical cavities 399
10.1 Cavity design and mixing analysis . . . 401
10.1.1 Stable cavity design . . . 401
10.1.2 Impedance matching . . . 405
10.1.3 Internally generated waves . . . 409
10.1.4 Cavity loss . . . 409
10.1.5 Constant field approximation . . . 409
10.1.6 Gaussian beams . . . 410
10.2 Cavity sum frequency mixing . . . 411
10.2.1 Sum: Wave one resonated . . . 411
10.2.2 Sum: Waves one and two resonated . . . 416
10.2.3 Sum: Wave three resonated . . . 421
10.2.4 Sum: Waves one and three resonated . . . 423
10.2.5 Sum: Waves one, two, and three resonated . . . 425
10.3 Optical parametric oscillators . . . 428

10.3.1 Threshold power 428
10.3.2 Constancy of the mean pump field 431
10.3.3 OPO: Wave one resonated 432
10.3.4 OPO: Waves one and two resonated 440
10.3.5 OPO: Waves one and three resonated 449
10.3.6 OPO: Waves one, two, and three resonated 455
10.4 Difference frequency generation 459
10.4.1 Difference: Wave one resonated 460
10.4.2 Difference: Wave two resonated 463
10.4.3 Difference: Waves one and three resonated 464
10.4.4 Difference: Waves two and three resonated 468
10.4.5 Difference: Waves one and two resonant 469
10.4.6 Difference: Waves one, two, and three resonated . . 470
10.4.7 Difference: Wave three resonated 473
10.5 Exercises 475

11 Short pulse cavity devices **501**
11.1 Synch-pumped OPOs (SP-OPOs) 502
11.1.1 Rate multiplied SP-OPOs 503
11.1.2 Cavity dumped SP-OPOs 503
11.2 Singly-resonant SP-OPOs 503
11.2.1 Equal group velocities 504
11.2.2 Unequal group velocities 506
11.2.3 Nonzero group delay dispersion 511
11.2.4 Nonzero intensity dependent refractive index, n_2 . . 516
11.2.5 SP-OPO stability 520
11.3 Doubly-resonant SP-OPOs 521
11.4 Frequency combs 522
11.4.1 Singly resonant SP-OPO combs 523
11.4.2 Doubly resonant SP-OPO combs 523
11.5 CW-pumped, mode-locked OPOs 524
11.6 Exercises 525

12 Nanosecond optical parametric oscillators **531**
12.1 Survey of nanosecond OPO types 533
12.1.1 Singly resonant (SRO) 533
12.1.2 Doubly resonant (DRO) 533
12.1.3 Cross resonant (CRO) 534
12.1.4 Pump resonant 535
12.1.5 Backward wave 535
12.2 Efficiency of nanosecond OPOs 535
12.2.1 All waves monochromatic 536
12.2.2 Broadband operation 542
12.3 Spectral properties of nanosecond OPOs 548

12.3.1 Fine spectral control of SROs 550
12.3.2 Fine spectral control of DROs 554
12.3.3 Fine spectral control of CROs 556
12.3.4 Fine spectral control of BWOs 556
12.4 Beam quality of nanosecond OPOs 557
12.4.1 Confocal unstable cavity 560
12.4.2 Image rotating cavity 561
12.4.3 Influence of optical imperfection 562
12.5 Anomalies and pathologies 563
12.6 Exercises 564

13 Exotica **577**
13.1 Single pass mixing 577
13.1.1 Applications of cascade n_2 mixing 577
13.1.2 Angle multiplexed OPA pumping 578
13.1.3 Wavelength multiplexed collinear OPA pumping . . 579
13.1.4 Nonuniform QPM gratings 579
13.1.5 Dark intermediate state cascade mixing 581
13.1.6 Recirculating frequency doubler 582
13.2 Cavity nonlinear devices 583
13.2.1 Cavity frequency multipliers 584
13.2.2 Cavity wavelength multipliers 585
13.2.3 Enhanced OPOs 589
13.2.4 Nanosecond OPOs with reduced back conversion . . 592
13.3 Nonlinear devices inside a laser cavity 593
13.3.1 Intracavity SFG & DFG 593
13.3.2 Intracavity OPOs 594
13.3.3 Bifunctional (laser + nonlinear) crystals 597

14 Tensor properties of crystals **599**
14.1 Thermal expansion 600
14.1.1 Thermal strain tensor 604
14.1.2 Shorter derivation of $\alpha(\theta)$ 604
14.1.3 Generalization to three dimensions 605
14.1.4 Thermal expansion in arbitrary plane 605
14.2 Thermal conductivity & resistivity 606
14.3 Refractive index 608
14.4 Higher order tensors 609
14.4.1 Strain-optic effect 609
14.4.2 Stress and strain 610
14.4.3 Linear electro-optic effect 610
14.5 Transformation properties of tensors 610

15 Thermal Effects **613**

15.1 Nonuniform heating: simplified analysis 614
15.1.1 Disruption of phase matching 616
15.1.2 Thermal lensing 617
15.1.3 Thermal tilt 618
15.1.4 Pulsed heating 618
15.2 Nonuniform heating: detailed analysis 619
15.2.1 Computing the temperature profile 620
15.2.2 Thermo-optic effect 623
15.2.3 Strain-optic effect 624
15.2.4 Electro-optic effect 626

16 Crystal nonlinearity **629**
16.1 The $\boldsymbol{d}$ tensor 629
16.1.1 Definition of $\boldsymbol{d}$ 629
16.1.2 Absolute signs of $\boldsymbol{d}$ 632
16.2 Effective nonlinearity d_{eff} 632
16.3 Example d_{eff} calculations 634
16.3.1 Isotropic example 634
16.3.2 Uniaxial example 635
16.3.3 Biaxial example 635
16.4 General d_{eff} calculations 637
16.4.1 Signs of d_{eff} 639
16.4.2 d_{eff} surface 640
16.5 Crystal symmetry and $\boldsymbol{d}$ 641
16.5.1 Enantiomorphism 645
16.5.2 Gyrotropy 646
16.5.3 Ferroelectricity and poling 646
16.5.4 Pyroelectricity 647
16.5.5 Piezoelectricity 647
16.5.6 Walk off compensation 648
16.5.7 Triclinic: 1, $\bar{1}$ 648
16.5.8 Monoclinic: $2, m, 2/m$ 651
16.5.9 Orthorhombic: $222, mm2, mmm$ 656
16.5.10 Tetragonal: $4, \bar{4}, 4/m, 422, 4mm, \bar{4}2m, 4/mmm$ 660
16.5.11 Trigonal: $3, \bar{3}, 32, 3m, \bar{3}m$ 666
16.5.12 Hexagonal: $6, \bar{6}, 6/m, 622, 6mm, \bar{6}m2, 6/mmm$ 671
16.5.13 Cubic: $23, \bar{4}3m, m3, 432, m3m$ 676

17 Measuring $\boldsymbol{d}$ **681**
17.1 Phase matched methods 681
17.1.1 Spherical crystal method 682
17.1.2 Parallelepiped crystal method 684
17.2 Non-phase matched methods 687
17.2.1 Separated beams method 692

17.2.2 Maker fringe methods 701
17.2.3 Powder methods 704
17.3 Wavelength or Miller scaling of $\boldsymbol{d}$ 704
17.4 Quantum calculation of $\boldsymbol{d}$ 708
17.5 Exercises 709

References **713**

Index **757**

1
Introduction

In this introduction we list important definitions and relations that will be used throughout the book. We will use SI units exclusively. In a departure from custom, for degenerate mixing where the two red waves have identical frequencies, we keep the same three mixing equations as in nondegenerate mixing by splitting the power or energy of the degenerate waves into two equal parts. No degeneracy factor is needed.

Comments specific to SNLO and the exercises are contained in text boxes like this one. SNLO is freeware available from AS-Photonics. It is useful in selecting nonlinear crystals and modeling their performance. It contains a number of preloaded examples that will be used in the exercises listed at the end of each chapter.

1.1 Maxwell's equations in linear medium

For reference we present Maxwell's equations. Vector and tensor quantities will be in bold face throughout the book.

$$\boldsymbol{\nabla} \cdot \mathbf{B} = 0, \tag{1.1}$$

$$\boldsymbol{\nabla} \cdot \mathbf{D} = \rho, \tag{1.2}$$

$$\boldsymbol{\nabla} \times \mathbf{E} = -\frac{\partial \mathbf{B}}{\partial t}, \tag{1.3}$$

$$\boldsymbol{\nabla} \times \mathbf{H} = \frac{\partial \mathbf{D}}{\partial t} + \mathbf{J}, \tag{1.4}$$

where

$$\mathbf{D} = \boldsymbol{\epsilon} \cdot \mathbf{E} = \epsilon_\circ (\boldsymbol{I} + \boldsymbol{\chi}) \cdot \mathbf{E} = \epsilon_\circ \mathbf{E} + \mathbf{P}, \tag{1.5}$$

and $\boldsymbol{\epsilon}$, $\boldsymbol{I}$, and $\boldsymbol{\chi}$ are (3×3) matrices. $\boldsymbol{I}$ is the unit matrix, $\boldsymbol{\epsilon}$ is the dielectric tensor, and $\boldsymbol{\chi}$ is the linear susceptibility tensor.

$$\mathbf{B} = \mu_\circ (\mathbf{H} + \mathbf{M}), \tag{1.6}$$

$$\mu_\circ \epsilon_\circ c^2 = 1. \tag{1.7}$$

In the case of an isotropic dielectric refractive index is given by

$$n = \sqrt{\epsilon / \epsilon_\circ}. \tag{1.8}$$

We consider crystals that are nonconductive ($\mathbf{J} = 0$), uncharged ($\rho = 0$), and nonmagnetic ($\mathbf{M} = 0$), so Maxwell's equations reduce to

$$\boldsymbol{\nabla} \cdot \mathbf{B} = 0, \tag{1.9}$$

$$\boldsymbol{\nabla} \cdot \mathbf{D} = 0, \tag{1.10}$$

$$\boldsymbol{\nabla} \times \mathbf{E} = -\mu_\circ \frac{\partial \mathbf{H}}{\partial t}, \tag{1.11}$$

$$\boldsymbol{\nabla} \times \mathbf{H} = \frac{\partial \mathbf{D}}{\partial t}. \tag{1.12}$$

Combining the last two equations gives the wave equation

$$\boldsymbol{\nabla} \times \boldsymbol{\nabla} \times \mathbf{E} = -\mu_\circ \frac{\partial^2}{\partial t^2} \mathbf{D}. \tag{1.13}$$

Using the identity

$$\boldsymbol{\nabla} \times \boldsymbol{\nabla} \times \mathbf{V} = -\boldsymbol{\nabla}^2 \mathbf{V} + \boldsymbol{\nabla}(\boldsymbol{\nabla} \cdot \mathbf{V}), \tag{1.14}$$

the wave equation is often written as

$$\boldsymbol{\nabla}^2 \mathbf{E} - \boldsymbol{\nabla}(\boldsymbol{\nabla} \cdot \mathbf{E}) = \mu_\circ \frac{\partial^2}{\partial t^2} \mathbf{D}. \tag{1.15}$$

The Poynting vector which describes energy flow is defined by

$$\mathbf{S} = \mathbf{E} \times \mathbf{H}. \tag{1.16}$$

Throughout the book we use S as the symbol for irradiance.

1.2 Variable names and units

$\mathbf{B}$	magnetic induction	$\mathrm{Wb/m^2}$
$\mathbf{D}$	optical displacement field	$\mathrm{C/m^2}$
$\mathbf{E}$	optical electric field	V/m
$\mathbf{H}$	magnetic field	A-m
$\mathbf{P}$	optical polarization	$\mathrm{C/m^2}$
$\mathbf{S}$	Poynting vector	$\mathrm{W/m^2}$
$\boldsymbol{k}$	wave vector	$\mathrm{m^{-1}}$
$\Delta\boldsymbol{k}$	phase mismatch	$\mathrm{m^{-1}}$
$\mathcal{F}$	pulse fluence	$\mathrm{J/m^2}$
$\mathcal{P}$	power	W
$\mathcal{U}$	pulse energy	J
$\epsilon_\circ$	8.85×10^{-12}	F/m
$\mu_\circ$	1.26×10^{-6}	H/m
c	3.00×10^{8}	m/s
ϵ_{ij}	dielectric tensor element	F/m
$\chi^{(1)}_{ij}$	linear susceptibility element	dimensionless
$\chi^{(2)}_{ijk}$	second order susceptibility element	m/V
$\chi^{(3)}_{ijkl}$	third order susceptibility element	$\mathrm{m^2/V^2}$
d_{ij}	$\chi^{(2)}_{ij}/2$	m/V
d_{eff}	effective nonlinearity	m/V
$S_\circ$	characteristic irradiance	$\mathrm{W/m^2}$
n	refractive index	dimensionless
n_2^I	nonlinear refractive index	$\mathrm{m^2/W}$
n_g	group velocity index	dimensionless
v_g	group velocity	m/s
D	group delay dispersion	$\mathrm{s^2/m}$
α	linear power absorption coefficient	$\mathrm{m^{-1}}$
β	nonlinear power absorption coefficient	m/W
λ	wavelength in vacuum	m
ν	frequency	Hz
ρ	birefringent walk off angle	rad
ω	angular frequency	rad/s

1.3 Conversion factors & definitions

$$d(\mathrm{SI}) = d(\mathrm{cgs}) \times 4\pi/(3\times10^4) \tag{1.17}$$

$$d = \chi^{(2)}/2 \tag{1.18}$$

$$\chi^{(3)}(\mathrm{SI}) = \chi^{(3)}(\mathrm{cgs}) \times 4\pi/(3\times10^4) \tag{1.19}$$

$$
\begin{aligned}
n_g &= c/v_g && (1.20)\\
D(\mathrm{fs}^2/\mathrm{mm}) &= -GVD \times n_g^2/2\pi c^3 && (1.21)\\
\Delta k &= k_3 - k_1 - k_2 && (1.22)\\
\Delta k_{\mathrm{acceptance}} &= 2\pi/L && (1.23)\\
L_{\mathrm{coherence}} &= \pi/\Delta k && (1.24)
\end{aligned}
$$

1.4 Definition of mixing strength $S_\circ$

This book is mostly about second order nonlinear mixing of three waves. We label them waves one, two, and three, with the convention shown in Fig. 1.1. The frequencies satisfy ($\omega_3 = \omega_1 + \omega_2$) so the bluest wave is always called wave three. We will see that the form of the mixing equations are symmetric in the fields of the two red waves with frequencies ω_1 and ω_2, so we will not apply any general rule to distinguish between waves one and two. We will also try to avoid terms such as pump, signal, and idler because they are not uniquely defined in the literature. Similarly we will try to avoid the labels type I, type II, type III that are applied to mixing processes with certain polarization relationships. Instead we will simply state the polarization and wavelength for each wave.

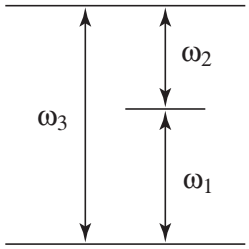

FIGURE 1.1. Naming convention for the three waves interacting in a second order nonlinear mixing process. The names of waves one and two are interchangeable.

In discussions of nonlinear mixing it is useful to use a characteristic irradiance $S_\circ$, defined for a particular crystal and set of wavelengths by

$$S_\circ = \frac{\epsilon_\circ c^3 \tilde{n}_1 \tilde{n}_2 \tilde{n}_3}{2 d_{\mathrm{eff}}^2 \omega_1 \omega_2 L^2} = \frac{\epsilon_\circ c\, \tilde{n}_1 \tilde{n}_2 \tilde{n}_3 \lambda_1 \lambda_2}{8\pi^2 d_{\mathrm{eff}}^2 L^2}, \qquad (1.25)$$

where d_{eff} is the effective nonlinear coefficient, L is the crystal length, and ω_1 and ω_2 are the angular frequencies of the two redder waves. The $\tilde{n}$'s are the refractive indices of the three waves in the crystal, corrected for beam tilts, as we will discuss in Chapter 3. If at least one of the input waves has

an irradiance comparable to $S_\circ$, efficient energy transfer among the three waves is possible.

1.5 Gaussian profiles

1.5.1 S_M/e^2 definitions

It is customary to describe Gaussian pulse and beam profiles in terms of the (S_M/e^2) points, where S_M is the peak irradiance. For example, the irradiance of a pulse with Gaussian time and space profiles is

$$S(x,y,t) = S_M e^{-2t^2/\tau^2} e^{-2x^2/w_x^2} e^{-2y^2/w_y^2}. \tag{1.26}$$

Integrating over any of the three Gaussian dimensions replaces the exponential with $(\sqrt{\pi/2}\, d_i)$, where d_i is the width in the dimension being integrated. For instance, integrating over time gives the fluence

$$\begin{aligned} \mathcal{F}(x,y) &= \int_{-\infty}^{\infty} S_M\, e^{-2t^2/\tau^2}\, e^{-2x^2/w_x^2}\, e^{-2y^2/w_y^2}\, dt & (1.27)\\ &= \left[\sqrt{\frac{\pi}{2}}\tau\right] S_M\, e^{-2x^2/w_x^2}\, e^{-2y^2/w_y^2}. & (1.28) \end{aligned}$$

Integrating over x and over y gives the power

$$\begin{aligned} \mathcal{P}(t) &= \int_{-\infty}^{\infty}\int_{-\infty}^{\infty} S_M\, e^{-2t^2/\tau^2}\, e^{-2x^2/w_x^2}\, e^{-2y^2/w_y^2}\, dxdy & (1.29)\\ &= \left[\frac{\pi}{2} w_x w_y\right] S_M\, e^{-2t^2/\tau^2}. & (1.30) \end{aligned}$$

Integrating over x, y, and t gives the pulse energy

$$\mathcal{U} = \left[\left(\frac{\pi}{2}\right)^{3/2} \tau w_x w_y\right] S_M. \tag{1.31}$$

The energy and the on-axis fluence are related by

$$\mathcal{U} = \mathcal{F}_M \frac{\pi w_x w_y}{2}, \tag{1.32}$$

where $\mathcal{F}_M$ is the peak fluence. For flat phase profiles, the Fourier transform widths measured at (S_M/e^2) satisfy

$$\tau\Delta\omega = w_x\Delta k_x = w_y\Delta k_y = 2. \tag{1.33}$$

We can define an effective area for a beam as

$$A_{\text{eff}} = \frac{\left(\int |E(x,y)|^2 dxdy\right)^2}{\int |E(x,y)|^4 dxdy}. \tag{1.34}$$

For a Gaussian beam the effective area is

$$A_{\text{eff}} = \pi w_x w_y. \tag{1.35}$$

1.5.2 FWHM definitions

Alternatively we can define the same Gaussian profiles in terms of full widths at the half maximum irradiance points. We call the FWHM values T, X, and Y. They are related to τ, $w_{\circ x}$, and $w_{\circ y}$ by

$$T = \tau\sqrt{2\ln(2)} = 1.177\,\tau, \tag{1.36}$$

$$X = w_x\sqrt{2\ln(2)}, \tag{1.37}$$

and

$$Y = w_y\sqrt{2\ln(2)}. \tag{1.38}$$

The lowest order Gaussian spatial and temporal irradiance profile can be expressed

$$S(x,y,t) = S_M\, e^{-4\ln(2)x^2/X^2} e^{-4\ln(2)y^2/Y^2} e^{-4\ln(2)t^2/T^2}. \tag{1.39}$$

Integrating over any of the three Gaussian dimensions replaces the exponential with $(\sqrt{\pi/[4\ln 2]}\; d_i)$, where d_i is the width in the dimension being integrated. For instance, integrating over time gives the fluence

$$\mathcal{F}(x,y) = \left[\sqrt{\frac{\pi}{4\ln 2}}\, T\right] S_M\, e^{-4\ln(2)x^2/X^2} e^{-4\ln(2)y^2/Y^2}. \tag{1.40}$$

Integrating over x and over y gives the power

$$\mathcal{P}(t) = \left[\frac{\pi}{4\ln 2}\, XY\right] S_M\, e^{-4\ln(2)t^2/T^2}. \tag{1.41}$$

Integrating over x, y, and t gives the pulse energy

$$\mathcal{U} = \left[\left(\frac{\pi}{4\ln 2}\right)^{3/2} TXY\right] S_M. \tag{1.42}$$

The energy and the on-axis fluence are related by

$$\mathcal{U} = \mathcal{F}_M \frac{\pi XY}{4\ln 2}. \tag{1.43}$$

The numerical value of $(\sqrt{\pi/[4\ln 2]})$ is 1.0645. For flat phase fronts, the Fourier transform full widths at $(S_M/2)$ obey

$$T\Delta\omega = X\Delta k_x = Y\Delta k_y = 4\ln 2 = 2.77. \tag{1.44}$$

1.5.3 Supergaussians

Often a profile that is more flat-topped than a lowest order Gaussian is needed. We define a super Gaussian profile of order m by

$$S(x,y) = S_M \exp\left\{ -\ln(2)\left[\left(\frac{2x}{X}\right)^2 + \left(\frac{2y}{Y}\right)^2\right]^m \right\}, \tag{1.45}$$

where m is an integer. The full widths at half maximum irradiance are X and Y. The lowest order Gaussian corresponds to $(m = 1)$. Larger values of m make the profile progressively more like a top-hat.

1.5.4 Sech squared pulses

The time profile of ultra short pulses is sometimes best fit by a hyperbolic secant profile of width (FWHM) T,

$$\mathcal{P}(t) = \mathcal{P}_M \operatorname{sech}^2\left(\alpha \frac{t}{T}\right), \tag{1.46}$$

where

$$\alpha = 2\ln\left(\sqrt{2}+1\right) = 1.76275, \tag{1.47}$$

and

$$\mathcal{U} = \int_{-\infty}^{\infty} \mathcal{P}(t)\, dt = \frac{2\mathcal{P}_M T}{\alpha}. \tag{1.48}$$

1.5.5 Rayleigh and dispersion lengths

For a lowest order Gaussian spatial profile with a round waist of size $w_\circ$ (radius at S_M/e^2) the Rayleigh range is defined as

$$z_R = \frac{k w_\circ^2}{2} = \frac{A_{\text{eff},\circ}}{\lambda}, \tag{1.49}$$

where $A_{\text{eff},\circ}$ is the effective area at the beam waist and λ is the wavelength in the medium. At distance z from the waist the beam size is

$$w(z) = w_\circ \sqrt{1 + \frac{z^2}{z_R^2}}\,, \tag{1.50}$$

and the phase front radius of curvature is

$$R(z) = z\left[1 + \frac{z_R^2}{z^2}\right]. \tag{1.51}$$

Similarly, for a lowest order Gaussian temporal profile with shortest duration $\tau_\circ$ the dispersion length is

$$z_D = \frac{\tau_\circ^2}{2D}, \tag{1.52}$$

where D is the group delay dispersion, given by

$$D = \frac{\partial^2 k}{\partial \omega^2}. \tag{1.53}$$

At a distance z from the point of minimum duration the duration is

$$\tau = \tau_\circ \sqrt{1 + \frac{z^2}{z_D^2}}\,, \tag{1.54}$$

and the frequency chirp is

$$\dot{\omega} = \frac{2}{\tau_\circ^2}\,\frac{z/z_D}{1 + z^2/z_D^2}. \tag{1.55}$$

1.6 Field expansions

As a mathematical convenience it is customary in optics to express an optical field or polarization in terms of a carrier wave and a complex envelope function. For example, an optical field $\mathbf{E}(x, y, z, t)$, which is always a real quantity, can be written

$$\mathbf{E}(x, y, z, t) = \frac{1}{2}\left[\boldsymbol{E}(x, y, z, t)e^{-i\omega_c t + i\mathbf{k}_c\cdot\mathbf{r}} + \boldsymbol{E}^*(x, y, z, t)e^{i\omega_c t - i\mathbf{k}_c\cdot\mathbf{r}}\right], \tag{1.56}$$

where the field is factored into a carrier wave of frequency ω_c and wave vector $\boldsymbol{k}_c$, and a complex envelope function $\boldsymbol{E}(x, y, z, t)$ that defines the modulation of the carrier wave in time and space. The carrier wave is an arbitrarily chosen monochromatic plane wave that lies near the central temporal and spatial frequencies of the real field.

Throughout this book real vector quantities such as an electric field or a polarization are represented by bold upright letters, while the complex field components are represented by the bold italic letters.

1.6.1 Fourier transform definitions

The envelope functions may be Fourier transformed between t and ω using

$$\boldsymbol{E}(x, y, z, \omega) = \frac{1}{\sqrt{2\pi}}\int_{-\infty}^{\infty} \boldsymbol{E}(x, y, z, t)e^{i\omega t}dt, \tag{1.57}$$

$$\boldsymbol{E}(x,y,z,t) = \frac{1}{\sqrt{2\pi}} \int_{-\infty}^{\infty} \boldsymbol{E}(x,y,z,\omega) e^{-i\omega t} d\omega, \tag{1.58}$$

where ω represents detuning from the carrier frequency. Similarly, the envelope functions can be transformed from x to k_x or from y to k_y using

$$\boldsymbol{E}(k_x,y,z,t) = \frac{1}{\sqrt{2\pi}} \int_{-\infty}^{\infty} \boldsymbol{E}(x,y,z,t) e^{-ik_x x} dx, \tag{1.59}$$

$$\boldsymbol{E}(x,k_y,z,t) = \frac{1}{\sqrt{2\pi}} \int_{-\infty}^{\infty} \boldsymbol{E}(x,y,z,t) e^{-ik_y y} dy, \tag{1.60}$$

where k_x and k_y represent tilts relative to the carrier k-vector which is usually assumed to point in the z direction.

We use $\Leftrightarrow$ to indicate Fourier transform pairs, for example

$$\boldsymbol{E}(x,y,z,t) \Leftrightarrow \boldsymbol{E}(x,y,z,\omega). \tag{1.61}$$

1.6.2 Fourier transform properties

Here we list some convenient relations for transforms. The relation

$$\frac{1}{\sqrt{2\pi}} \int E_1(\omega) E_2(\omega_\circ - \omega) d\omega \Longleftrightarrow E_1(t) E_2(t) \tag{1.62}$$

indicates that the transform of the product of two fields is a convolution of the individual transforms of the two fields.

The transform pair

$$E_\circ e^{-(x/x_\circ)^2} \Longleftrightarrow \frac{1}{\sqrt{2}} E_\circ x_\circ e^{-(k_x x_\circ/2)^2} \tag{1.63}$$

indicates that a Gaussian in x space with a constant phase is the transform of a Gaussian in k_x space with a constant phase. Note that the two widths, $x_\circ$ and $2/x_\circ$, satisfy Eq. (1.33).

The relation

$$\frac{dE(t)}{dt} \Longleftrightarrow -i\omega E(\omega) \tag{1.64}$$

relates the transform of the time derivative of a field to the field's $(t \to \omega)$ transform.

Similarly the relation

$$\frac{dE(x)}{dx} \Longleftrightarrow ik_x E(k_x) \tag{1.65}$$

relates the transform of the space derivative of a field to the field's $(x \to k_x)$ transform.

1.7 Abbreviations

BB	broad bandwidth
B&K	Boyd and Kleinman
BW	bandwidth
BWO	backward wave oscillator
CW	continuous wave
CPM	compensated phase match
CPOPA	chirped pulse optical parametric amplification
CRO	cross resonant oscillator
DFG	difference frequency generation
DRO	doubly resonant oscillator
FDTD	finite difference time domain
FFT	fast Fourier transform
FWHM	full width half maximum
GDD	group delay dispersion
GVD	group velocity dispersion
GVM	group velocity mismatch
LP	long pulse
NCPM	noncritical phase match
OPA	optical parametric amplifier
OPG	optical parametric generator
OPF	optical parametric fluorescence
OPO	optical parametric oscillator
ppX	periodically poled crystal X
PW	plane wave
QPM	quasi phase match
ROC	radius of curvature
SBS	stimulated Brillouin scattering
SFG	sum frequency generation
SHG	second harmonic generation
SP	short pulse or synchronously pumped
SPM	self phase modulation
SRO	singly resonant oscillator
SRS	stimulated Raman scattering
SVEA	slowly varying envelope approximation
THG	third harmonic generation
TPA	two photon absorption
TRO	triply resonant oscillator
WOC	walk off compensated

2

Linear crystal optics for monochromatic plane waves

The physics of three-wave mixing in anisotropic crystals can be conveniently separated into three topics: how a light wave is changed when it enters or exits the crystal, how a light wave propagates in the crystal, and how three-wave mixing occurs in the crystal. Each of these topics can be considered at different levels of complexity, but each begins with a treatment of monochromatic plane waves. This chapter is devoted to the first two topics, linear propagation of monochromatic plane waves in a crystal, and their behavior on entering or exiting the crystal. Chapters 3 & 4 will explain nonlinear mixing of the monochromatic plane waves. Once the behavior of monochromatic plane waves is thoroughly explored, we will show in subsequent chapters how linear combinations of monochromatic plane waves are used to construct realistic beams and pulses, and how the equations that describe those realistic cases are derived and applied.

As a starting point we rewrite Maxwell's equations specifically for monochromatic plane waves. Following the customary procedure, we write the vectors for the polarization, the electric field, and the displacement in complex notation,

$$\mathbf{P} = \frac{1}{2}\left[\boldsymbol{P}e^{-i(\omega t-\mathbf{k}\cdot\mathbf{r})} + \boldsymbol{P}^{*}e^{i(\omega t-\mathbf{k}\cdot\mathbf{r})}\right], \tag{2.1}$$

$$\mathbf{E} = \frac{1}{2}\left[\boldsymbol{E}e^{-i(\omega t-\mathbf{k}\cdot\mathbf{r})} + \boldsymbol{E}^{*}e^{i(\omega t-\mathbf{k}\cdot\mathbf{r})}\right], \tag{2.2}$$

$$\mathbf{D} = \frac{1}{2}\Big[\boldsymbol{D}e^{-i(\omega t-\mathbf{k}\cdot\mathbf{r})} + \boldsymbol{D}^* e^{i(\omega t-\mathbf{k}\cdot\mathbf{r})}\Big]. \tag{2.3}$$

The actual fields are represented by the real quantities $\mathbf{P}$, $\mathbf{E}$, and $\mathbf{D}$, but for many calculations it is more convenient to use the complex envelope functions $\boldsymbol{D}$, $\boldsymbol{E}$, and $\boldsymbol{P}$. These complex vectors are in general functions of (x, y, z, t). However, for monochromatic plane waves, they are independent of space and time so we omit these arguments in this chapter, and treat the envelope functions as simple complex vectors.

We substitute the expansions of Eqs. (2.1)-(2.3) in the wave equation, Eq. (1.13)

$$\boldsymbol{\nabla}\times\boldsymbol{\nabla}\times\mathbf{E} = -\mu_\circ\frac{\partial^2}{\partial t^2}\mathbf{D} = -\mu_\circ\frac{\partial^2}{\partial t^2}\Big[\epsilon_\circ\mathbf{E}+\mathbf{P}\Big]. \tag{2.4}$$

The operator $\boldsymbol{\nabla}$ becomes $(\pm i\boldsymbol{k})$ when it operates on the exponent $(\pm i\boldsymbol{k}\cdot\boldsymbol{r})$. Similarly the operator $(\partial/\partial t)$ becomes $(\pm i\omega)$ when it operates on the exponent $(\pm i\omega t)$. Making these substitutions in Eq. (2.4) and equating the positive (or negative) frequency components on each side of the equation yields

$$\boldsymbol{k}\times\boldsymbol{k}\times\boldsymbol{E} = -\mu_\circ\omega^2\boldsymbol{D}. \tag{2.5}$$

In deriving this equation we assumed that $\boldsymbol{E}$ and $\boldsymbol{D}$ do not change on propagation, so this is a wave equation for eigenpolarized light. This expression implies that $\boldsymbol{D}$ must be normal to $\boldsymbol{k}$, but $\boldsymbol{D}$ is not necessarily parallel to $\boldsymbol{E}$. However, $\boldsymbol{k}$, $\boldsymbol{D}$, and $\boldsymbol{E}$ must lie in a single plane.

We use a similar procedure to rewrite the Poynting vector equation to find the energy flow for monochromatic plane waves. We start with Eq. (1.16), the general Poynting vector equation,

$$\mathbf{S} = \frac{1}{\mu_\circ}\mathbf{E}\times\mathbf{B} = \mathbf{E}\times\mathbf{H}. \tag{2.6}$$

For monochromatic plane waves the third Maxwell equation, Eq. (1.3), relates $\boldsymbol{H}$ to $\boldsymbol{E}$ for eigenpolarized light in a nonmagnetic material by

$$\boldsymbol{H} = \frac{\boldsymbol{k}\times\boldsymbol{E}}{\mu_\circ\omega}. \tag{2.7}$$

Substituting the expansions for $\mathbf{E}$ and $\mathbf{H}$ in Eq. (2.6), equating equal frequency components, and using Eq. (2.7) plus

$$\epsilon_\circ\mu_\circ c^2 = 1, \tag{2.8}$$

we arrive at

$$\langle\mathbf{S}\rangle = \frac{n\epsilon_\circ c}{2}|\boldsymbol{E}|^2\ \hat{\boldsymbol{e}}\times\hat{\boldsymbol{k}}\times\hat{\boldsymbol{e}}, \tag{2.9}$$

where the angle brackets around **S** indicate a time average over the optical cycle. We only care about the time averaged values, so we will leave the brackets off in the remainder of the book, and **S** will be understood to be the time averaged Poynting vector. The unit vector $\hat{\boldsymbol{e}}$ is parallel to the electric field, and the unit vector $\hat{\boldsymbol{k}}$ is parallel to the propagation vector (normal to the wave fronts). From Eq. (2.9) we see that the flow of optical energy, represented by **S**, is perpendicular to $\boldsymbol{E}$, but not necessarily parallel to $\boldsymbol{k}$. However, **S**, $\boldsymbol{E}$, and $\hat{\boldsymbol{k}}$ must lie in a single plane.

It is a good idea to memorize the two pairings of orthogonal vectors we have just derived, ($\boldsymbol{E}\perp\mathbf{S}$) and ($\boldsymbol{D}\perp\boldsymbol{k}$).

The remainder of this chapter consists of finding solutions to Eq. (2.5) in anisotropic crystals. The solutions will allow us to explore linear propagation in biaxial crystals, and to show how uniaxial and isotropic crystals are special cases of biaxial crystals. I choose this approach because it is not difficult to understand propagation in biaxial crystals, and also because the popular nonlinear crystals of the KTP family (KTP, RTP, KTA, RTA, CTA), plus several borate crystals (LBO, CBO, BiBO, YCOB, GdCOB), and $KNbO_3$ are all biaxial.

Our discussion of light propagation in biaxial crystals will progress from a word-and-diagram geometrical sketch to a more mathematical description based on that geometrical picture, and finally to more abstract mathematical derivations based directly on Maxwell's equations and crystal dielectric tensors.

2.1 A geometrical description

The word picture presented in this section is adapted from Born and Wolf's classic text *Principles of Optics* [1]. We consider only crystals that are nonmagnetic (**M**=0) and nonconductive (**J**=0).

The solution to the wave equation for eigenpolarized light,

$$\boldsymbol{k}\times\boldsymbol{k}\times\boldsymbol{E}=-\mu_\circ\omega^2\boldsymbol{D}, \tag{2.10}$$

can be broken into two steps. The first step is to relate $\boldsymbol{D}$ to $\boldsymbol{E}$ in a general way. The second step is to find the specific paired values of $\boldsymbol{D}$ and $\boldsymbol{E}$ that solve the wave equation.

2.1.1 Relating $\boldsymbol{D}$ to $\boldsymbol{E}$

Any two vector quantities in a nonisotropic crystal are generally related by a (3×3) tensor. In our case of $\boldsymbol{D}$ and $\boldsymbol{E}$, the relation is

$$\boldsymbol{D}=\boldsymbol{\epsilon}\cdot\boldsymbol{E}, \tag{2.11}$$

where $\boldsymbol{\epsilon}$ is the symmetric (3×3) dielectric tensor. It will be more convenient to use this equation in the form

$$\boldsymbol{E} = \boldsymbol{\epsilon}^{-1}\cdot\boldsymbol{D}. \tag{2.12}$$

As we discuss in Chapter 14, Eq. (2.12) can be associated with a three dimensional ellipsoid with principal axes n_x, n_y, and n_z defined by

$$n_x = \sqrt{\epsilon_{xx}/\epsilon_\circ}\,, \tag{2.13}$$

$$n_y = \sqrt{\epsilon_{yy}/\epsilon_\circ}\,, \tag{2.14}$$

$$n_z = \sqrt{\epsilon_{zz}/\epsilon_\circ}\,. \tag{2.15}$$

This ellipsoid has various names in the literature. We will call it the D-ellipsoid because, as we will see, it relates a given $\boldsymbol{D}$ to its paired $\boldsymbol{E}$. The D-ellipsoid is diagrammed in Fig. 2.1 where, for the purpose of illustration, the ellipticity is greatly exaggerated. In practice the lengths of the principal axes usually differ by 5% or less.

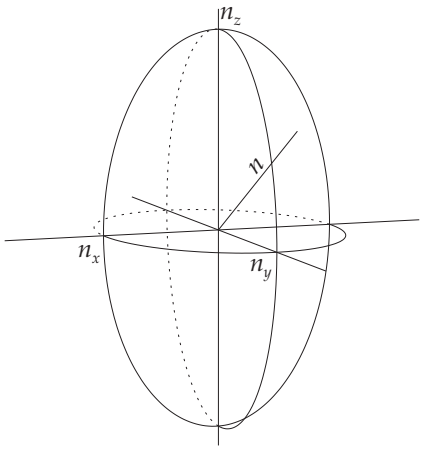

FIGURE 2.1. D-ellipsoid shown with the principal optical frame $\{x, y, z\}$ which is aligned to the primary axes of the ellipsoid with the convention $(n_x < n_y < n_z)$.

For biaxial crystals the three principal axes have different lengths, and we adopt the standard labeling with $(n_x < n_y < n_z)$. For uniaxial crystals two of the axes have equal length, while for isotropic crystals all three axes have equal length. These are limiting cases of the biaxial crystal, so an understanding of biaxial crystals will be easy to apply to them. We will

relate the orientation of the D-ellipsoid to the underlying crystal structure in Chapter 16. For now it is sufficient to know the D-ellipsoid exists for any crystal.

The D-ellipsoid represents the dielectric response for all orientations of $\boldsymbol{D}$. If $\boldsymbol{D}$-extended is drawn as a vector from the origin through the ellipsoid surface, the electric field $\boldsymbol{E}$ associated with $\boldsymbol{D}$ is parallel to the surface normal of the ellipsoid at the point where $\boldsymbol{D}$ intersects the surface. In general $\boldsymbol{E}$ is not quite parallel to $\boldsymbol{D}$. The two are exactly parallel only when they are aligned with one of the principal axes of the D-ellipsoid.

2.1.2 Finding the eigenpolarizations

As we showed earlier, the relation ($\boldsymbol{D} \perp \boldsymbol{k}$) must hold in order to satisfy the wave equation. If we consider a wave propagating along direction $\hat{\boldsymbol{k}}$, as shown in Fig. 2.2, $\boldsymbol{D}$ must lie in the plane normal to $\hat{\boldsymbol{k}}$. This plane passes through the center of the D-ellipsoid and intersects the ellipsoid in an ellipse that we can call the n-ellipse. The $\boldsymbol{E}$ field associated with $\boldsymbol{D}$ must be aligned normal the D-ellipsoid and thus normal to the n-ellipse. However, $\boldsymbol{E}$ does not generally lie in the plane of the n-ellipse.

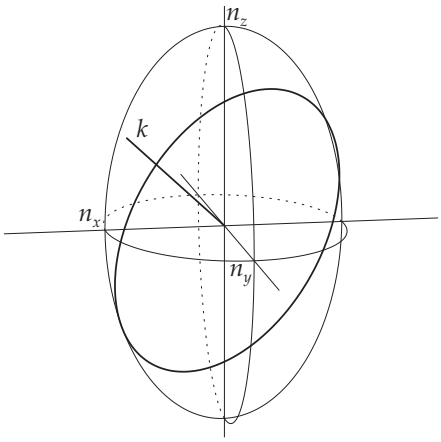

FIGURE 2.2. D-ellipsoid and propagation vector, $\boldsymbol{k}$. The plane normal to $\boldsymbol{k}$ that passes through the origin intersects the D-ellipsoid in the n-ellipse indicated by the heavy line. The eigenpolarization planes coincide with the major and minor axes of this n-ellipse, and the associated refractive indices are equal to the semi major and semi minor axes of the ellipse.

In order to satisfy the wave equation, $\boldsymbol{E}$ must lie in the same plane as $\boldsymbol{k}$ and $\boldsymbol{D}$. Otherwise the vector quantities on the two sides of Eq. (2.10)

would not be parallel. This condition can be met only if $\boldsymbol{D}$ lies along one of the principal axes of the n-ellipse. There are two possible solutions to the wave equation corresponding to $\boldsymbol{D}$ lying along either of the principal axes of the n-ellipse. The $\boldsymbol{D}$ vectors of the two solutions are thus orthogonal to one another, and in combination with $\boldsymbol{k}$ define two eigenpolarization planes that contain $\boldsymbol{k}$ and the paired solutions for $\boldsymbol{D}$ and $\boldsymbol{E}$. Only waves with $\boldsymbol{D}$ aligned along the major or minor axis of the n-ellipse propagate without changes to the direction of $\boldsymbol{D}$ or $\boldsymbol{E}$, that is as eigenpolarizations. The corresponding two refractive index values correspond to the lengths of the two principal axes of the n-ellipse. We use hi or lo to label the eigenpolarization associated with the higher or lower refractive index.

To summarize, the problem of finding the eigenpolarizations and their refractive indices is reduced to the problem of constructing the D-ellipsoid based on the crystal's dielectric tensor, followed by defining a propagation vector $\boldsymbol{k}$. The n-ellipse is then defined in the plane normal to $\boldsymbol{k}$, and the two eigenpolarization planes are those defined by $\boldsymbol{k}$ and the major and minor axes of the n-ellipse. The two corresponding refractive indices are given by the lengths of the semi major and semi minor axes of the n-ellipse.

2.1.3 Optical axes of biaxial crystals

Suppose we start with the propagation vector parallel to the z axis of the D-ellipsoid and continuously rotate it in the xz plane until it is parallel to x. Initially, when the propagation is along z, the n-ellipse lies in the xy plane, and n_{hi}, the higher index, must be equal to n_y, and n_{lo} must be equal to n_x. As the propagation direction rotates away from z toward the x, the n-ellipse pivots about the y-axis. Thus the y direction remains an eigenpolarization with the refractive index n_y, but the second refractive index increases as the angle increases, going from n_x for propagation along z to n_z for propagation along x. The second index starts out smaller than n_y and finishes larger than n_y, so at some intermediate angle it must be equal to n_y. At that angle the n-ellipse must be a circle with both refractive indices equal to n_y. This propagation direction is known as the optic axis, and its angle relative to z is traditionally labeled Ω. By symmetry there must be a second equivalent optic axis on the opposite side of the z-axis at $(-\Omega)$. As the propagation angle sweeps through Ω the major and minor axes of the n-ellipse swap places. For angles smaller than Ω the major axis is parallel to y, while for angles larger than Ω the minor axis is parallel to y.

2.1.4 Propagation outside the principal planes

When the k-vector lies outside the three principal planes, xy, xz, or yz, the n-ellipse and its eigenpolarization directions are generally rotated so the eigenpolarizations do not align with the axes of the D-ellipsoid. Figure 2.3 illustrates the two eigenpolarization directions for various propagation direction lying in one octant for the biaxial crystal $KNbO_3$. The eigenpolarizations twist as the propagation direction changes, but they are always orthogonal to one another. The other octants are images of this one reflected in the three principal planes, xy, yz, and xz. The angle of the optical axis, Ω, uniquely determines the entire eigenpolarization map for a crystal. All crystals with identical optical axis directions share the same eigenpolarization map.

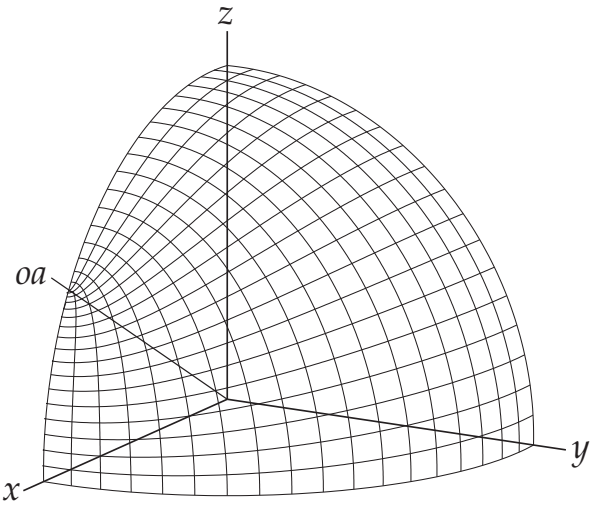

FIGURE 2.3. Eigenpolarization pairs plotted against the propagation direction in one octant of the biaxial crystal $KNbO_3$. The polarization directions for the *lo* refractive index follow lines originating on the yz arc, while the polarization directions for the *hi* refractive index follow lines originating on the xy arc. The optic axis is labeled *oa*. The other octants are reflections of this one in the three principal planes, xy, yz, or xz.

2.1.5 Poynting vector walk off

As described earlier, the electric field $\boldsymbol{E}$ paired with $\boldsymbol{D}$ is normal to the surface of the D-ellipsoid at the point where $\boldsymbol{D}$ intersects it, so $\boldsymbol{E}$ is not in general parallel to $\boldsymbol{D}$. For an eigenpolarization the point of intersection coincides with either the major or the minor axis of the n-ellipse, so the tilt of $\boldsymbol{E}$ must lie in the plane containing both $\boldsymbol{D}$ and $\boldsymbol{k}$. The small angle between $\boldsymbol{D}$ and $\boldsymbol{E}$ is conventionally labeled ρ. $\boldsymbol{E}$ is tilted relative to $\boldsymbol{D}$ in the direction of diminishing refractive index.

Recall that $\boldsymbol{E}$ and $\mathbf{S}$ are orthogonal. This implies that the angle between $\boldsymbol{k}$ and $\mathbf{S}$ is also ρ. Each of the eigenpolarizations has an associated Poynting vector walk off angle that we label ρ_{hi} or ρ_{lo}. These tilts are illustrated in Fig. 2.4.

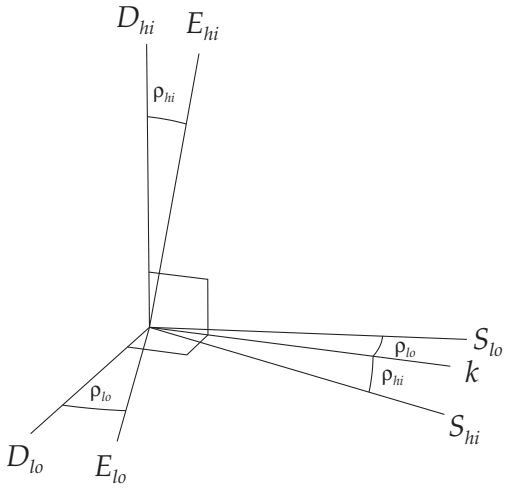

FIGURE 2.4. Vectors $\boldsymbol{D}_{hi}$, $\boldsymbol{E}_{hi}$, $\mathbf{S}_{hi}$, and $\boldsymbol{k}$ lie in a single plane while vectors $\boldsymbol{D}_{lo}$, $\boldsymbol{E}_{lo}$, $\mathbf{S}_{lo}$, and $\boldsymbol{k}$ lie in an orthogonal plane. Walk off angle ρ_{hi} is the angle between $\boldsymbol{D}_{hi}$ and $\boldsymbol{E}_{hi}$ and also the angle between $\boldsymbol{k}$ and $\mathbf{S}_{hi}$. Walk off angle ρ_{lo} is the angle between $\boldsymbol{D}_{lo}$ and $\boldsymbol{E}_{lo}$ and also the angle between $\boldsymbol{k}$ and $\mathbf{S}_{lo}$.

Because walk off occurs in the eigenpolarization planes, the lines in Fig. 2.3 that show the eigenpolarization directions also indicate the directions of the two Poynting vector walk off angles. For the *hi* eigenpolarization (curves originating on the xy arc), the energy flow is tilted along the *hi* eigenpolarization direction in the direction away from the xy plane, while for the *lo*-index polarization (curves originating on the yz plane) the

energy flow is tilted along the *lo* eigenpolarization direction toward the yz plane.

Walk off always tilts **S** toward the direction of lower refractive index, so if $\boldsymbol{k}$ is pivoted slightly in the plane of the *lo* eigenpolarization in the direction of walk off, n_{lo} decreases but n_{hi} is unaltered. This means that the lines in Fig. 2.3 that indicate the directions of the *lo* eigenpolarization (curves originating on the yz plane) are also curves of constant n_{hi}. Similarly, the *hi* eigenpolarization directions (curves originating on the xy plane) are curves of constant n_{lo}. For example, for propagation directions lying in the yz plane, the *hi* eigenpolarization lies in the yz plane and n_{hi} varies with angle, but the *lo* eigenpolarization is normal to the yz plane and $n_{lo} = n_x$, independent of angle. Similarly, along each of the lines originating on the xy arc, n_{lo} is constant, with a different value for each line, varying from n_x for the line lying in the yz plane to n_y for the line lying in the xz plane and terminating at the optic axis.

For propagation in a principal plane one of the walk off angles becomes zero. For example, propagation in the yz plane makes ($\rho_{lo} = 0$), while propagation in the xy plane makes ($\rho_{hi} = 0$). Propagation in the xz plane makes ($\rho_{lo} = 0$) for directions between *oa* and x, and ($\rho_{hi} = 0$) for directions between *oa* and z.

2.1.6 Hi and lo index surfaces

We have explained that there are two refractive indices associated with each propagation direction. They can be represented by double surfaces as shown in Fig. 2.5. The distance from the origin to the outer surface along any propagation direction is n_{hi}. The distance to the inner surface is n_{lo}. The two surfaces touch only at their point of intersection with the optic axes. The Poynting vector for a beam with *lo* polarization is normal to the inner surface, the Poynting vector for the beam with *hi* polarization is normal to the outer surface. The corresponding $\boldsymbol{E}$ fields are tangent to the surfaces.

2.1.7 Uniaxial crystals

The symmetry of the crystal structure for certain classes of crystals requires that two of the principal refractive indices be exactly equal (see Chapter 16). In the transition from biaxial to uniaxial there are two possibilities: the intermediate index n_y can approach the high index ($n_y \rightarrow n_z$) or the low index ($n_y \rightarrow n_x$). If ($n_y \rightarrow n_z$), the two optic axes tilt toward the x axis, while if ($n_y \rightarrow n_x$), the optic axes tilt toward the z axis. The left diagram in Fig. 2.6 shows the eigenpolarization directions for the crystal DLAP which has principal indices at 1064 nm of ($n_x = 1.496$), ($n_y = 1.558$),

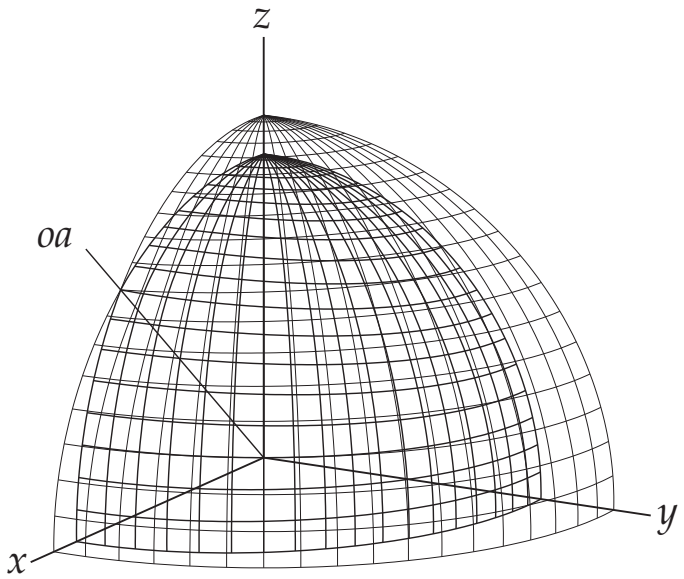

FIGURE 2.5. The two n surfaces. The distance from the origin to the outer surface at each value of (θ, ϕ) is $n_{hi}(\theta, \phi)$, while the distance to the inner surface is $n_{lo}(\theta, \phi)$. The **E** field for an eigenpolarization is tangent to the corresponding surface, and its Poynting vector **S** is normal to the corresponding surface. The optic axis *oa* is the only point where the two surfaces touch.

and $(n_z = 1.565)$. Its optic axis lies near the x axis. The right diagram in Fig. 2.6 shows the eigenpolarization directions for the crystal KTA which has principal indices at 1064 nm of $(n_x = 1.782)$, $(n_y = 1.787)$, and $(n_z = 1.868)$. Its optic axis lies near the z axis.

If n_y becomes exactly equal to n_x the two optic axes merge into a single optic axis oriented along z. The eigenpolarization directions then lie along the latitude and longitude lines as shown in Fig. 2.7. The *hi*-index wave, polarized along a line of constant longitude, is called the extraordinary, or *e*-wave, while the *lo*-index wave, polarized along a line of constant latitude, is called the ordinary, or *o*-wave. The n_o surface is spherical with radius $n_x (= n_y)$, while the n_e surface is an oblate ellipsoid of revolution with polar radius of $n_x (= n_y)$ and equatorial radius n_z. The left hand diagram

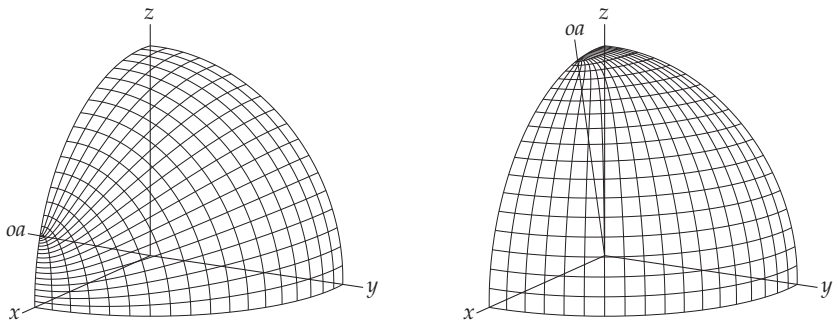

FIGURE 2.6. Eigenpolarization and walk off directions for DLAP (left) and KTA (right). The line labeled *oa* is the optic axis. The other octants are reflections of this one in the three principal planes.

of Fig. 2.8 shows a slice through the double n-surface for such a positive uniaxial crystal. The o-wave has no Poynting vector walk off, while the walk off of the e-wave is toward the z axis.

On the other hand, if n_y becomes exactly equal to n_z, the crystal is negative uniaxial and the two optic axes converge to a single axis lying along x. The eigenpolarization contours converge on the x axis rather than the z axis. However, for such crystals it is customary to abandon the convention ($n_x < n_y < n_z$) and relabel the unique axis from x to z. The eigenpolarization directions then are identical to those shown in Fig. 2.7. The ordinary or n_o surface is again spherical while the extraordinary or n_e surface is a prolate ellipsoid of revolution. A cross section through the double index surfaces for a negative uniaxial crystal shown on the right in Fig. 2.8. Poynting vector walk off of the e-wave is away from the z axis for a negative uniaxial crystal.

2.1.8 Isotropic crystals

If ($n_x = n_y = n_z$), all three refractive indices are equal so the D-ellipsoid is a sphere. The crystal is isotropic, meaning all propagation directions and polarizations are equivalent. There are no unique eigenpolarization directions determined by the crystal's dielectric response, so all polarizations are eigenpolarizations.

Exercise 1 illustrates computation of the *hi* and *lo* refractive indices plus the walk off angles, for any propagation direction in a biaxial or uniaxial crystal using the SNLO function RefInd.

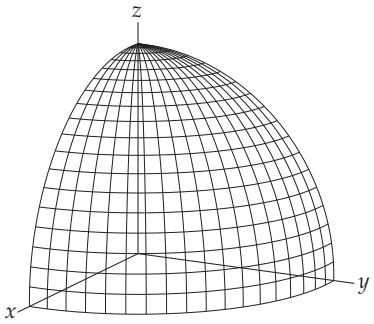

FIGURE 2.7. Eigenpolarization and walk off directions for a uniaxial crystal. The polarization and walk off direction for an extraordinary, or e-wave, lies along a line of constant longitude while the polarization direction for an ordinary, or o-wave, lies along a line of constant latitude.

2.2 Mathematics of the geometrical description

In Sec. 2.1 we presented a qualitative, graphical description of linear propagation of monochromatic plane waves in a biaxial crystal. In this section we develop the quantitative mathematical counterpart. We will make minimal reference to Maxwell's equations here, saving that for the next section. The derivations of this section are not particularly elegant, but they are tied directly to the geometrical picture using the D-ellipsoid and the n-ellipse. We will retrace the path of the previous discussion, starting with a derivation of the D-ellipsoid and following with analysis of the n-ellipse. If you are satisfied with the qualitative version already presented you can skip ahead to Sec. 2.4.

2.2.1 Finding the D-ellipsoid

The displacement $\boldsymbol{D}(\omega)$ produced by a monochromatic optical field $\boldsymbol{E}(\omega)$ can be written

$$\boldsymbol{D}(\omega) = \epsilon_\circ \boldsymbol{E}(\omega) + \boldsymbol{P}(\omega) = \epsilon_\circ \boldsymbol{E}(\omega) + \epsilon_\circ \boldsymbol{\chi}^{(1)}(\omega) \cdot \boldsymbol{E}(\omega). \tag{2.16}$$

The linear susceptibility $\boldsymbol{\chi}^{(1)}(\omega)$ in its most general form is a symmetric (3×3) tensor. Hiding the ω arguments, the displacement $\boldsymbol{D}$ can be written

$$\boldsymbol{D} = \boldsymbol{\epsilon} \cdot \boldsymbol{E}, \tag{2.17}$$

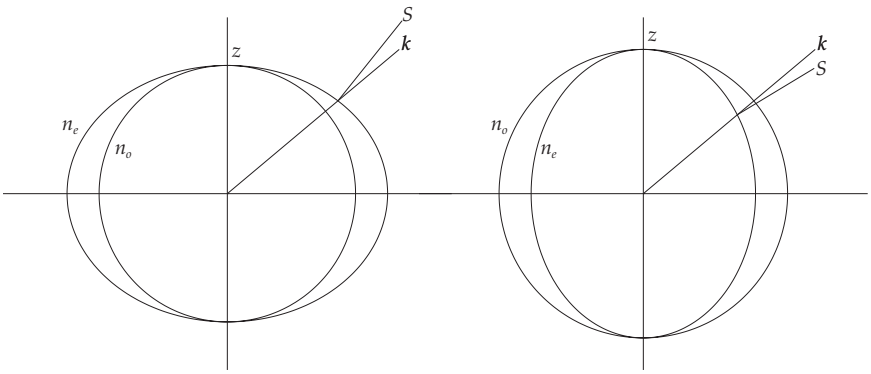

FIGURE 2.8. Poynting vector walk off directions for a positive uniaxial crystal (left) and negative uniaxial crystal (right).

where

$$\boldsymbol{\epsilon} = \epsilon_o[\boldsymbol{I} + \boldsymbol{\chi}^{(1)}], \tag{2.18}$$

and $\boldsymbol{I}$ is the (3×3) identity matrix. In expanded form Eq. (2.17) is

$$\begin{pmatrix} D_x \\ D_y \\ D_z \end{pmatrix} = \begin{pmatrix} \epsilon_{xx} & \epsilon_{xy} & \epsilon_{xz} \\ \epsilon_{yx} & \epsilon_{yy} & \epsilon_{yz} \\ \epsilon_{zx} & \epsilon_{zy} & \epsilon_{zz} \end{pmatrix} \begin{pmatrix} E_x \\ E_y \\ E_z \end{pmatrix}. \tag{2.19}$$

where the dielectric tensor ϵ is symmetric. By rotating the reference frame so it aligns with the dielectric principal frame $\boldsymbol{\epsilon}$ is diagonalized. Associating the diagonal elements of $\boldsymbol{\epsilon}$ with the principal refractive indices, $(\epsilon_{xx} = \epsilon_\circ n_x^2)$, $(\epsilon_{yy} = \epsilon_\circ n_y^2)$, and $(\epsilon_{zz} = \epsilon_\circ n_z^2)$ we write Eq. (2.17) in the principal reference frame

$$\begin{pmatrix} D_x \\ D_y \\ D_z \end{pmatrix} = \epsilon_\circ \begin{pmatrix} n_x^2 & 0 & 0 \\ 0 & n_y^2 & 0 \\ 0 & 0 & n_z^2 \end{pmatrix} \begin{pmatrix} E_x \\ E_y \\ E_z \end{pmatrix}. \tag{2.20}$$

The same equation in inverted form

$$\boldsymbol{E} = \boldsymbol{\epsilon}^{-1} \cdot \boldsymbol{D}, \tag{2.21}$$

yields, in the principal frame,

$$\begin{pmatrix} E_x \\ E_y \\ E_z \end{pmatrix} = \frac{1}{\epsilon_\circ} \begin{pmatrix} 1/n_x^2 & 0 & 0 \\ 0 & 1/n_y^2 & 0 \\ 0 & 0 & 1/n_z^2 \end{pmatrix} \begin{pmatrix} D_x \\ D_y \\ D_z \end{pmatrix}. \tag{2.22}$$

Next we define a refractive index n as the proportionality constant between $\boldsymbol{D}$ and the component of $\boldsymbol{E}$ parallel to $\boldsymbol{D}$ according to

$$E_{||} = \frac{1}{\epsilon_\circ n^2} D. \tag{2.23}$$

8

Mixing spatially and temporally structured beams

In this chapter we combine the ideas of Chapters 6 & 7 and apply them to mixing of beams with both spatial and temporal structure. We will emphasize the ability of spatial structure to modify the apparent group velocity and apparent group velocity dispersion of spectrally broad pulses. This ability is of practical use in achieving group velocity matched mixing, for example. We first consider a rather general case of second harmonic generation to illustrate the coupling between spatial and temporal structure. We then specialize to large diameter beams that allow us to ignore certain aspects of spatial walk off.

8.1 Linear propagation

We copy from Chapter 5 the general envelope propagation equation

$$\begin{aligned}\frac{\partial E}{\partial z} &= -\tan(\alpha+\rho)\frac{\partial E}{\partial x} - \frac{\cos\rho}{v_g\cos(\alpha+\rho)}\frac{\partial E}{\partial t} \\ &\quad +i\left(\frac{A}{2}\frac{\cos^3\rho}{\cos^3(\alpha+\rho)}\right)\frac{\partial^2 E}{\partial x^2} + i\left(\frac{B}{2}\frac{\cos\rho}{\cos(\alpha+\rho)}\right)\frac{\partial^2 E}{\partial y^2} \\ &\quad +i\left(-\frac{D}{2}\frac{\cos\rho}{\cos(\alpha+\rho)} + \frac{A}{2}\frac{\sin^2\alpha\cos^3\rho}{v_g^2\cos^3(\alpha+\rho)} + F\frac{\sin\alpha\cos^2\rho}{v_g\cos^2(\alpha+\rho)}\right)\frac{\partial^2 E}{\partial t^2} \\ &\quad +i\left(A\frac{\sin\alpha\cos^3\rho}{v_g\cos^3(\alpha+\rho)} + F\frac{\cos\alpha\cos\rho}{\cos(\alpha+\rho)}\right)\frac{\partial^2 E}{\partial x\partial t}. \qquad (8.1)\end{aligned}$$

This equation describes a beam propagating with its carrier k-vector tilted at angle α relative to the integration axis z. The coefficients of the various partial derivatives can be considered to be the effective walk off, the effective group velocity, *etc.*, each defined as the coefficient measured along a z axis that is common to the three coupled beams involved in a mixing process. Following the notation of Chapter 5, we indicate these effective coefficients by tildes. For example, the effective walk off angle is

$$\tilde{\rho} = \rho + \alpha \; . \tag{8.2}$$

The angle $\tilde{\rho}$ is the angle between the z-axis and the Poynting trajectory of a point at the center of the light envelope. The true, or intrinsic, walk off angle ρ is the walk off angle measured in the usual way, as the angle between $\boldsymbol{S}$ and $\boldsymbol{k}$. Similarly, the effective group velocity is

$$\tilde{v}_g = v_g \frac{\cos(\alpha + \rho)}{\cos \rho}, \tag{8.3}$$

and the effective group delay dispersion coefficient is

$$\widetilde{D} = D \frac{\cos \rho}{\cos(\alpha + \rho)} - A \frac{\sin^2 \alpha}{v_g^2} \frac{\cos^3 \rho}{\cos^3(\alpha + \rho)} - 2F \frac{\sin \alpha}{v_g} \frac{\cos^2 \rho}{\cos^2(\alpha + \rho)}, \tag{8.4}$$

where D is the intrinsic group delay dispersion coefficient, A is the intrinsic diffraction coefficient (approximately $1/k$), and F is the intrinsic frequency dependent walk off, which can usually be neglected. The effective coefficients can be used to propagate a pulse by numerically integrating the propagation equation along the z direction. They are generic in the sense that they are independent of the shape of the pulse envelope.

The mixing terms that couple the three equations were defined in Chapter 5 as

$$\frac{\partial E_1}{\partial z} = i \frac{d_{\text{eff}} \omega_1}{\tilde{n}_1 c} E_3 E_2^* e^{i \Delta k z}, \tag{8.5}$$

where d_{eff} and $\tilde{n}$ were defined in Eqs. (3.31) and (3.33). In this chapter we assume the pulses are long enough to neglect the additional mixing term that is proportional to $(\partial [E_3 E_2^*]/\partial t)$.

8.2 Second harmonic generation

We begin with a simple illustration of second harmonic generation by a small diameter, short fundamental pulse. This example shows how spatial and temporal structure can become entangled via nonlinear mixing. We will assume the diameter of the fundamental beam is large enough that diffraction is unimportant, yet small enough that birefringent walk off is

larger than the beam size. We also assume the pulse duration is long enough that dispersion is unimportant, yet short enough that temporal walk off between the fundamental and second harmonic is larger than the pulse duration. We also assume mixing is weak enough that the fundamental is not significantly depleted.

This SHG process is diagrammed in Fig. 8.1. The combination of spatial

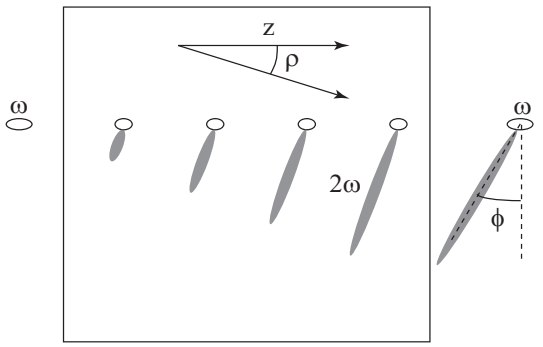

FIGURE 8.1. Second harmonic generation of a short, small diameter, fundamental pulse in a crystal with temporal and spatial walk off of the second harmonic relative to the fundamental. The output second harmonic is a slanted pulse whose slant angle is determined by the magnitudes of the spatial and temporal walk offs.

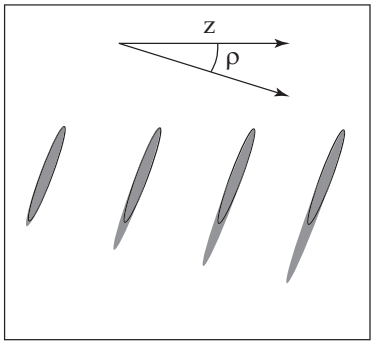

FIGURE 8.2. Second harmonic generation of a fundamental pulse with a slanted pulse envelope in the same crystal as in Fig. 8.1. The ellipse outlined by the solid line is the fundamental envelope; the shaded region is the second harmonic envelope.

and temporal walk off creates a slanted second harmonic envelope. As the pulses propagate through the crystal, the second harmonic pulse moves laterally relative to the fundamental pulse and also lags behind. This leads

to the slanted second harmonic pulse. The slant angle is easily calculated in terms of the spatial (ρ) and temporal ($n_{g2} - n_{g1}$) walk offs. After exiting the crystal the slant angle is ($\phi = \arctan[(n_{g2} - n_{g1})/\rho]$). Inside the crystal the slant of the second harmonic envelope is ($\phi_{int} = \arctan[(1 - n_{g1}/n_{g2})/\rho]$).

It is obvious that if the fundamental pulse is reshaped before entering the crystal so that inside the crystal it has an elongated envelope slanted at the same angle as the second harmonic just described, the fundamental envelope will better overlap the second harmonic envelope through the crystal. This is illustrated in Fig. 8.2. The group velocities of the fundamental and second harmonic are unchanged and are still unequal. However, the *apparent group velocities, defined as the velocities of the points of intersection between the envelopes and the z axis*, are now equal.

Apparent group velocities are further explained in Fig. 8.3. In this diagram, the fundamental is o polarized and ($S_1 \parallel k_1 \parallel z$). The second harmonic is e polarized so S_3 is tilted by the second harmonic walk off angle ρ relative to z. The true group velocity of second harmonic is less than that of the fundamental, so the center of its envelope, indicated in the figure by the lower dot, travels more slowly along the z direction than the center of the fundamental envelope, indicated by the upper dot. However, the apparent group velocities are equal. This equality requires the proper slant angle of the fundamental envelope.

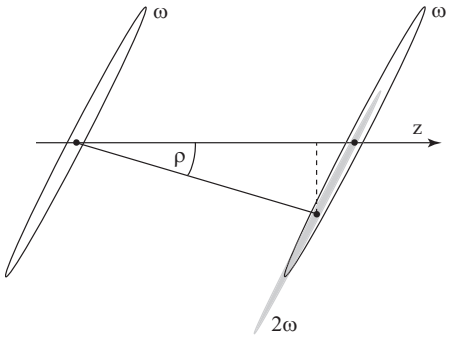

FIGURE 8.3. SHG using a slanted pulse. The k vectors are parallel to z, and the fundamental is o polarized so its Poynting vector is along z. The second harmonic is e polarized so its Poynting vector makes an angle of ρ with the z axis. The envelope on the left is the fundamental envelope at ($t = 0$). The envelopes on the right are the fundamental and second harmonic envelopes at ($t > 0$). The true group velocity of the second harmonic is less than that of the fundamental so the center of its envelope, indicated by the lower dot, lags behind the center of the fundamental envelope, indicated by the upper dot. However, the *apparent* group velocities, as measured at the point of intersection of the envelopes and the z axis, are equal.

Exercise 1 uses 2D-mix-SP to illustrate SHG of a 100 fs pulse in a 5 mm long BBO crystal. The second harmonic envelope is slanted as shown in Fig. 8.1

8.3 Tilted beams & slanted envelopes

For some cases the general propagation and mixing equations for tilted beams listed in Eqs. (8.1)-(8.5) are more general than necessary. If we assume the pulse profiles look like large diameter pancakes we can incorporate the x and y derivatives in the t derivative terms to obtain equations similar to the plane-wave mixing equations of Chapter 6. That is the topic of this section. The group velocities and GDD coefficients in the modified equations are the apparent group velocities and apparent GDD coefficients. Such a treatment is permissible if certain conditions are met. We must assume the beam diameters are large enough that spatial walk off is much smaller than the beam diameters; we must assume the three pulses have equal slant angles; we must assume the entrance and exit faces of the crystals are parallel to the pulse envelopes. This situation is diagrammed in Fig. 8.4. The three pulse envelopes are parallel and the pancakes have diameters much larger than the spatial walk off associated with the noncollinear Poynting vectors. These restrictions mean that along any axis parallel to the z axis each pancake has a well defined apparent v_g and apparent D coefficient. The further

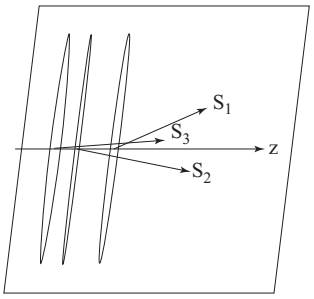

FIGURE 8.4. Generalized short pulse envelope diagram. The pulses have parallel, slanted envelopes, but different propagation directions. The crystal faces are parallel to the envelopes.

simplifying assumptions that the $\tilde{n}$ values in Eq. (8.5) can be replaced by n values, and the crystal faces can be normal to z rather than parallel to the envelopes, are usually used, although they are not truly justified.

8.3.1 Apparent group velocity and GDD

We use the notation $\hat{v}_g$ and $\widehat{D}$ to indicate apparent group velocities and GDD coefficients. We must show how $\hat{v}_g$ and $\widehat{D}$ can be computed from their true values plus the propagation tilts and envelope slants. To help with this we note that a slanted pulse can be created by reflecting a short, unslanted pulse from a grating as shown in Fig. 8.5. We exploit this equivalence in computing $\hat{v}_g$ and $\widehat{D}$. In the near field the reflected pulse is an undispersed pulse with a slanted envelope. In the far field it is angularly dispersed by the grating, with the red components tilted in the direction of the leading edge of the near field pulse and the blue components tilted in the direction of the trailing edge.

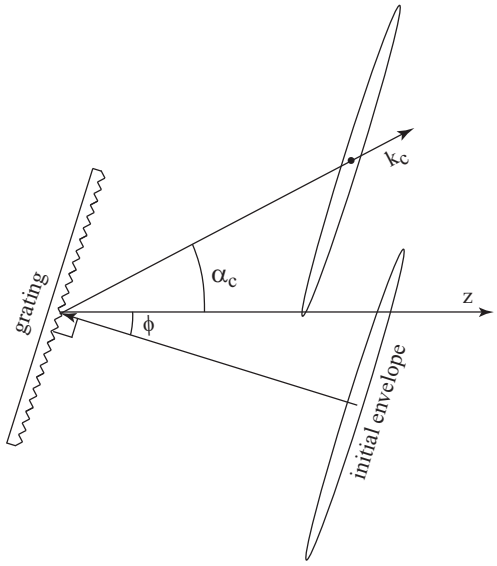

FIGURE 8.5. Slanted pulse generated by reflecting a normally incident, unslanted pulse from a diffraction grating. The slant angle is ϕ and the propagation angle is α_c, both measured relative to the z axis.

Figure 8.6 shows our notational conventions for a large diameter, short light pulse propagating in a birefringent crystal. We assume both the propagation vector $\boldsymbol{k}$, and the normal to the pulse envelope lie in the same plane as the birefringent walk off ρ. The apparent group velocity $\hat{v}_g$ is the velocity of the intersection of the envelope with the z-axis. It is not a true group velocity because it does not refer to a fixed point within the envelope. The apparent group delay dispersion $\widehat{D}$ is the dispersion of the apparent group

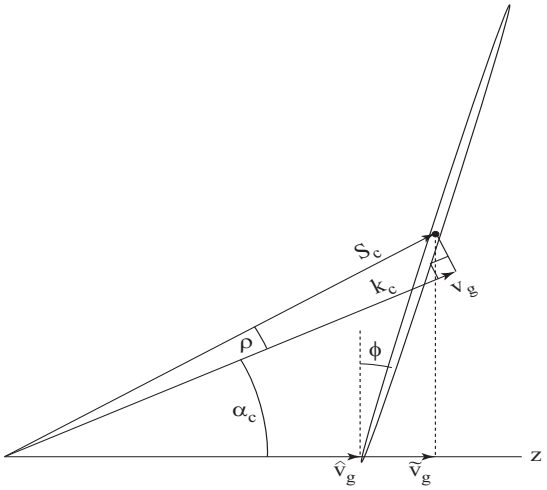

FIGURE 8.6. The apparent group velocity $\hat{v}_g$ is the velocity of the point of intersection between a short, slanted pulse and the z axis. Velocity v_g is the group velocity as it is usually defined. Subscript c refers to the carrier wave.

delay. It accounts for the dispersive reshaping of the envelope as measured along the z axis.

The apparent velocity and dispersion are the full derivatives of k_z with respect to ω,

$$\frac{1}{\hat{v}_g} = \frac{dk_z}{d\omega} \tag{8.6}$$

and

$$\widehat{D} = \frac{d^2k_z}{d\omega^2}. \tag{8.7}$$

These definitions take account of the fact that k_z is a function of both ω and α, and, for slanted pulses, α is a function of ω and ϕ. Figure 8.5 shows how a light pancake propagating at carrier angle α_c with slant angle ϕ can be mathematically constructed. An unchirped light pancake with no slant relative to its k vector (initial envelope) is normally incident on a diffraction grating embedded in the crystal, from which the carrier wave diffracts at angle $(\alpha_c + \phi)$. Figure 8.7 shows the corresponding k-vector diagram for this process. In evaluating Eqs. (8.6) and (8.7) we use the expansion

$$\frac{dk_z}{d\omega} = \frac{d(k\cos\alpha)}{d\omega} = \left[\frac{\partial k}{\partial\omega} + \frac{\partial k}{\partial\alpha}\frac{\partial\alpha}{\partial\omega}\right]\cos\alpha - k\sin\alpha\frac{\partial\alpha}{\partial\omega}. \tag{8.8}$$

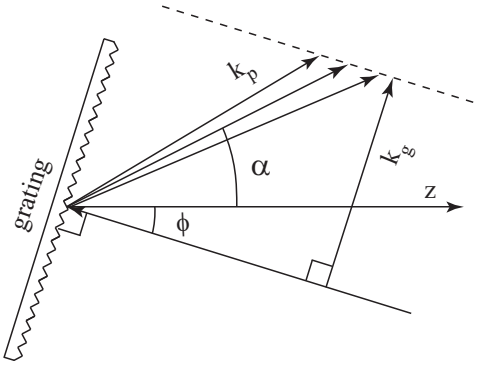

FIGURE 8.7. Slanted pulse generation k vectors. Each k_p vector of the reflected pulse has a transverse component equal to the grating vector, k_g, in the direction parallel to the grating.

Using the standard definitions of walk off and group velocity

$$\tan\rho = -\frac{1}{k}\frac{\partial k}{\partial \alpha} \tag{8.9}$$

$$\frac{1}{v_g} = \frac{\partial k}{\partial \omega} \tag{8.10}$$

in Eq. (8.8) we find

$$\frac{1}{\hat{v}_g} = \frac{dk_z}{d\omega} = \left[\frac{1}{v_g} - k\tan\rho\frac{\partial\alpha}{\partial\omega}\right]\cos\alpha - k\sin\alpha\frac{\partial\alpha}{\partial\omega}. \tag{8.11}$$

We still need to find $(\partial\alpha/\partial\omega)$, the relation between angle and frequency. This is derived by differentiating the grating equation

$$k\sin(\alpha+\phi) = k_g \tag{8.12}$$

with respect to ω to find

$$\left[\frac{\partial k}{\partial\omega} + \frac{\partial k}{\partial\alpha}\frac{\partial\alpha}{\partial\omega}\right]\sin(\alpha+\phi) + k\cos(\alpha+\phi)\frac{\partial\alpha}{\partial\omega} = 0. \tag{8.13}$$

Solving for $(\partial\alpha/\partial\omega)$ for the central, or carrier wave, gives

$$\left.\frac{\partial\alpha}{\partial\omega}\right|_c = \frac{1}{kv_g}\left[\frac{\tan(\alpha_c+\phi)}{\tan\rho\tan(\alpha_c+\phi)-1}\right] = \frac{-1}{kv_g}\left[\frac{\cos\rho\sin(\alpha_c+\phi)}{\cos(\alpha_c+\phi+\rho)}\right]. \tag{8.14}$$

For brevity we will write α_c as α below. Substituting this in Eq. (8.11) gives a convenient expression for $\hat{v}_g$

$$\hat{v}_g = v_g\frac{\cos(\alpha+\rho)}{\cos\rho}\left[1-\tan(\alpha+\rho)\tan\phi\right] = v_g\frac{\cos(\alpha+\phi+\rho)}{\cos\phi\cos\rho}. \tag{8.15}$$

Happily, this expression for the apparent group velocity can also be deduced directly from the geometry of the diagram in Fig. 8.6. It also agrees with Eq. (8.1) when ($\phi = 0$), in which case the x derivatives are zero for large pancakes.

The apparent group delay dispersion,

$$\widehat{D} = \frac{d^2 k_z}{d\omega^2} \tag{8.16}$$

can be evaluated in a similar manner. After considerable tedious algebra, the result is

$$\begin{aligned} \widehat{D} &= D\frac{\cos\phi\cos\rho}{\cos(\alpha+\phi+\rho)} \\ &\quad -A\frac{1}{v_g^2}\frac{\cos\phi\sin^2(\alpha+\phi)\cos^3\rho}{\cos^3(\alpha+\phi+\rho)} \\ &\quad -F\frac{2}{v_g}\frac{\cos\phi\sin(\alpha+\phi)\cos^2\rho}{\cos^2(\alpha+\phi+\rho)}. \end{aligned} \tag{8.17}$$

The coefficients A, D, and F are respectively the diffraction, group delay dispersion, and frequency dependent walk off coefficients we derived in Chapter 5. Comparing with Eq. (8.4) we see that when ($\phi = 0$), ($\tilde{D} = \widehat{D}$).

In case this derivation seems too abstract, we offer the following simplified, intuitive derivation of $\widehat{D}$. The appearance of A (the x diffraction coefficient) in the expression for $\widehat{D}$ might seem odd at first glance. However, the role of diffraction becomes apparent if we look at the simplified case of a slanted pulse propagating in vacuum with $\boldsymbol{k}$ parallel to the z-axis, as shown in Fig. 8.8. The blue and red envelopes separate because of grating angular dispersion, which is a manifestation of diffraction. Thus diffraction accounts for the separation of the dots shown in Fig. 8.8 at the center of the envelopes. In vacuum there is no true group delay dispersion which would lead to a longitudinal separation of the dots, so D cannot contribute to $\widehat{D}$. However, the apparent group delay dispersion $\widehat{D}$ refers to the separation of the $\times$'s in Fig. 8.8, so it has a nonzero value due to diffraction, that is proportional to the diffraction coefficient A. We can compute it from

$$k_z = k\cos(\phi - \phi_c), \tag{8.18}$$

where ϕ_c is the diffraction angle of the carrier frequency. The expression for $\widehat{D}$ is

$$\widehat{D} = \left.\frac{d^2 k_z}{d\omega^2}\right|_{\phi=\phi_c} = -k\left(\frac{d\phi}{d\omega}\right)^2. \tag{8.19}$$

Using the grating relation

$$\phi = \arcsin(k_g/k), \tag{8.20}$$

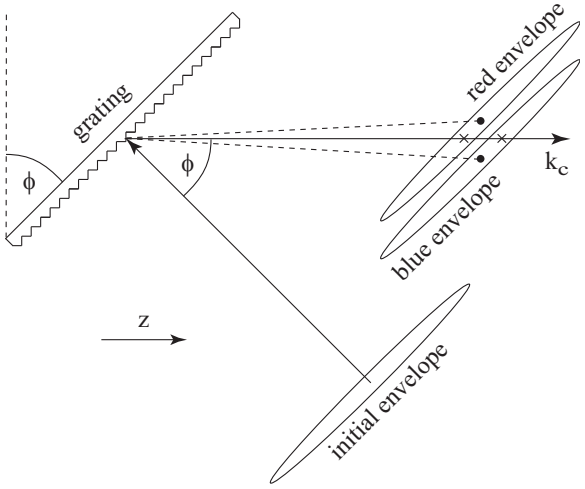

FIGURE 8.8. Diffraction of a short light pancake from a grating. The red and blue portions of the spectrum separate with the red portion diffracted at a larger angle than the blue portion.

we find

$$\frac{d\phi}{d\omega} = -\frac{1}{kc}\tan\phi, \tag{8.21}$$

which, combined with Eq. (8.19) and the vacuum values $(D = 0)$, $(F = 0)$, $(A = 1/k)$, $(\rho = 0)$, gives

$$\widehat{D} = -A\frac{1}{c^2}\tan^2\phi, \tag{8.22}$$

in agreement with Eq. (8.17) when $(\alpha = 0)$, $(\rho = 0)$. Note that because the red light trails the blue light the apparent dispersion is always anomalous in vacuum, so the sign of $\widehat{D}$ is negative. This apparent group delay dispersion is commonly used in femtosecond technology to stretch or compress pulses using grating pairs[112].

Repeating this exercise for a grating embedded a dispersive, nonbirefringent material rather than in vacuum adds a contribution proportional to D, the true group delay dispersion coefficient, yielding

$$\widehat{D} = D - A\frac{1}{v_g^2}\tan^2\phi, \tag{8.23}$$

again in agreement with Eq. (8.17) for $(\alpha = 0)$, $(\rho = 0)$. Note that because the signs of the D and A terms are opposite in normally dispersive media, it may be possible to tune $\widehat{D}$ to zero by adjusting ϕ. If $(\widehat{D} = 0)$ the wave

will propagate without any change in shape caused by GDD. This can be achieved if the slant angle is set to

$$\tan\phi = \sqrt{\frac{Dv_g^2}{A}}, \tag{8.24}$$

or, using the approximation ($A = 1/k$),

$$\tan\phi = \sqrt{Dv_g^2 k}\ . \tag{8.25}$$

Now that we have derived propagation equations for slanted pulses that include no transverse derivatives, we can forget the pulses are slanted and tilted, and if the conditions listed earlier are met, we can use the apparent group velocities defined by Eq. (8.15) and the apparent GDD coefficients defined by Eq. (8.17) in the plane-wave mixing equations in place of v_g and D. We can integrate these mixing equations as though the pulses were true plane waves with envelopes normal to z and k vectors parallel to z.

8.3.2 Group velocity matched SHG of short, slanted pulses

We return to our earlier example of group velocity matched SHG in a birefringent crystal for a more quantitative treatment. We will demonstrate the close relation between group velocity matched SHG of slanted pulses and achromatic SHG using angular dispersion of the fundamental light. Both of these maximize the phase matching bandwidth.

As we showed earlier, the shortest second harmonic pulses and the broadest second harmonic bandwidth, as well as the highest conversion efficiency, are achieved when the group velocities of the fundamental and second harmonic pulses are equal. The apparent group velocity for a pulse with a slanted envelope is given by Eq. (8.15) which we reproduce here

$$\hat{v}_g = v_g \frac{\cos(\alpha + \phi + \rho)}{\cos\phi\cos\rho}. \tag{8.26}$$

Assuming the two fundamental pulses have the same polarization, with both carrier waves propagating along z, the second harmonic carrier must also propagate along z, so ($\alpha_3 = 0$), giving

$$\hat{v}_{g3} = v_{g3} \frac{\cos(\phi_3 + \rho_3)}{\cos\phi_3\cos\rho_3}. \tag{8.27}$$

Usually the true group velocity of the second harmonic is slower than that of the fundamental. In a negative uniaxial crystal such as BBO, the second harmonic is e polarized while the fundamental is o polarized. For the o-polarized fundamental, ($\rho = 0$) and ($\hat{v}_{g1} = v_{g1}$), so its apparent group

velocity is simply the true group velocity, regardless of the slant angle ϕ. However, the apparent group velocity of the e-polarized second harmonic can be adjusted by changing the slant angle ϕ. To increase $\hat{v}_{g3}$ the slant must be in the negative direction, meaning the normal to the envelope is tilted in the same direction as the walk off ρ, so ϕ_3 and ρ_3 have opposite signs. The pulse envelopes must all have the same slant ($\phi_1 = \phi_3 = \phi$), so matching the apparent group velocities of the fundamental and second harmonic is achieved when ϕ is adjusted to satisfy

$$v_{g1} = v_{g3}\frac{\cos(\phi + \rho_3)}{\cos\phi\cos\rho_3}. \tag{8.28}$$

Exercise 2 illustrates a calculation of the slant angles ϕ required for group velocity matching (or achromatic phase matching) in second harmonic generation.

8.3.3 Achromatic SHG of frequency chirped pulses

There are a variety of other ways to increase the acceptance bandwidth, and we will discuss some of them later, but the method that is most obvious in the case of a swept-frequency fundamental pulse is achromatic phase matching[195] in which the angle of the fundamental wave is varied with wavelength so the beam always propagates along a phase matched direction in a birefringent crystal. We again illustrate using the example of an o-polarized fundamental and an e-polarized second harmonic wave, appropriate for a negative uniaxial crystal such as BBO. The waves propagate nearly parallel to the fixed z axis, and the propagation angle of the fundamental, measured relative to z, is ϑ_1. If ϑ_1 is properly varied as $\Delta\omega_1$ is tuned, phase matching can be maintained. Because phase matching is maintained the fundamental and second harmonic waves have parallel propagation vectors as $\Delta\omega$ is tuned so we drop the subscripts on ϑ. To first order in ϑ the expression for Δk_z due to tilt alone is

$$\Delta k_z = \left.\frac{\partial k_{3z}}{\partial\vartheta}\right|_{\vartheta=0}\vartheta - 2\left.\frac{\partial k_{1z}}{\partial\vartheta}\right|_{\vartheta=0}\vartheta. \tag{8.29}$$

The second term is zero because the fundamental is o polarized, leaving

$$\Delta k_z = \left.\frac{\partial k_{3z}}{\partial\vartheta}\right|_{\vartheta=0}\vartheta. \tag{8.30}$$

Equating the Δk induced by tilt (ϑ) to the negative of Δk induced by tuning ($\Delta\omega_1$) gives the relation between tilt angle and detuning required to maintain phase matching

$$\left.\frac{\partial k_{3z}}{\partial\vartheta}\right|_{\vartheta=0}\vartheta = -2\left(\frac{1}{v_{g3}} - \frac{1}{v_{g1}}\right)\Delta\omega_1. \tag{8.31}$$

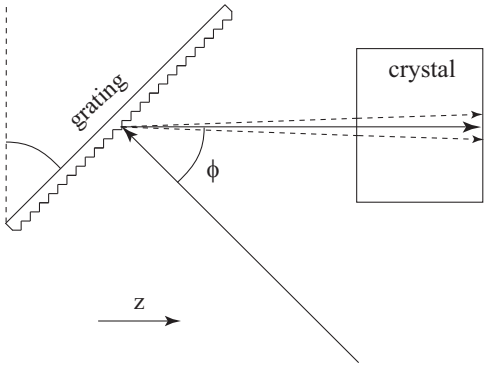

FIGURE 8.9. Angular dispersion of fundamental for first order achromatic phase matching of second harmonic generation.

We use the birefringent walk off equation

$$\frac{\partial k}{\partial \vartheta} = -k \tan \rho \tag{8.32}$$

to rewrite this as

$$\left(k_{3z} \tan \rho_3\right) \vartheta = \left(\frac{1}{v_{g3}} - \frac{1}{v_{g1}}\right) \Delta\omega_3, \tag{8.33}$$

or in differential form as

$$\frac{\partial \vartheta}{\partial \omega_3} = \frac{\left(1/v_{g3} - 1/v_{g1}\right)}{k_{3z} \tan \rho_3}. \tag{8.34}$$

This equation has the same form as the grating dispersion equation Eq. (8.14) which, for $(\alpha = 0)$, becomes

$$\frac{\partial \vartheta}{\partial \omega_3} = \frac{-1}{k_3 v_{3g}} \frac{\cos \rho \cos \phi}{\cos(\rho + \phi)}. \tag{8.35}$$

This equation describes a dispersion that can be provided by a grating. The implication is that we can achieve achromatic phase matching to first order in $\Delta\omega$ by dispersing the fundamental using a grating as shown in Fig. 8.9. If we equate the right hand sides of Eqs. (8.35) and (8.34) we find that it reduces to

$$v_{g1} = v_{g3} \frac{\cos(\phi + \rho_3)}{\cos \phi \cos \rho_3}, \tag{8.36}$$

in agreement with the group velocity matching requirement of Eq. (8.28).

This shows that achromatic SHG and group velocity matched SHG are based on the same far field angular dispersion of the fundamental pulse. Although the reasoning used in deriving this result for short pulses and for swept frequencies differed, it is clear that achromatic phase matching and matched apparent group velocities are in some sense equivalent.

If an extremely broad phase matching bandwidth is desired it is possible to fine tune the propagation angle versus frequency with a correction term proportional to $(\Delta\omega^2)$. This cannot be achieved with a single grating but combinations of gratings and prisms or prisms alone can be used[195]. This would be equivalent to adjusting the $\widehat{D}$'s to fulfill the optimum broadband condition ($\widehat{D}_3 = \widehat{D}_1/2$) that was derived in Chapter 6.

8.3.4 Mixing three short slanted pulses

Ideal broadband phase matching for three short pulses requires matching all three apparent group velocities so

$$\hat{v}_{g1} = \hat{v}_{g2} = \hat{v}_{g3}. \tag{8.37}$$

In rare instances such a group velocity match can be found for collinear mixing. One example[43] is (4024 nm + 983 nm $\leftrightarrow$ 790 nm) mixing along propagation direction ($\theta = 70°, \phi = 22°$) in $KNbO_3$. Another lucky coincidence is quasi phase matched mixing ($1500 - 1800$ nm + $2250 - 1970$ nm $\leftrightarrow$ 940 nm) in poled $LiNbO_3$ with a period of 27.2 μm and a temperature of 52°C[196].

Group velocity matching can also sometimes be accomplished in birefringent crystals[197] by slanting the three pulse envelopes to a common angle ϕ and tilting the waves, as shown in Fig. 8.10. The carrier waves are phase matched for a particular value of α by adjusting the propagation angle in the crystal θ. The transverse carrier k-vectors must add to zero. The common slant angle ϕ can be adjusted to seek a match of the $\hat{v}_g$s. The ability to independently adjust α, ϕ, and θ in seeking to equalize three apparent group velocities means success with this method is often possible. However, matching the group velocities fixes both ϕ and α, leaving no independent adjustment of the $\widehat{D}$s. Dispersion can be adjusted only by selecting a different crystal, a different set of polarizations, or a different principal plane if the crystal is biaxial.

Exercise 3 shows how to use SNLO function GVM to match the group velocities of three pulses in noncollinearly phase matched mixing of slanted pulses.

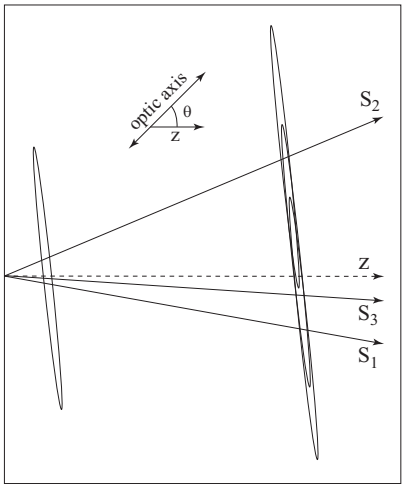

FIGURE 8.10. Scheme for matching the apparent group velocities of three pulses in a birefringent crystal. The pulses have a common slant angle but different directions of propagation. Varying the crystal angle, the beam angles, and the slant angle can sometimes achieve group velocity matching.

8.3.5 CPOPA

CPOPA is our acronym for chirped pulse optical parametric amplification. To create the highest achievable optical fields it is necessary to make a pulse as short as possible and the beam quality as high as possible. However, optical damage to nonlinear crystals and other optics places practical limits on the irradiance and power of short pulses. Amplifier damage can be avoided by starting with a low energy, short pulse, stretching the pulse in time to create a much longer chirped pulse, amplifying the chirped pulse to a high energy, and then recompressing the pulse using large area diffraction gratings. Optical parametric amplification in a nonlinear crystal is an attractive amplification method because it can provide high gain over a broad bandwidth with little added background from fluorescence.

One requirement for amplifying 10 fs pulses is that the gain be nearly uniform over 1500 cm^{-1}. Such a broad bandwidth requires that we match the apparent group velocities ($\hat{v}_{g1} = \hat{v}_{g2}$) and also closely approximate ($\widehat{D}_1 = -\widehat{D}_2$). This is seldom possible using collinear phase matching, but achromatic phase matching can sometimes achieve this. For simplicity it would be best if the output light of interest, which we will label ω_1, is not angle dispersed so it does not have a slanted pulse envelope. The slant or dispersion of the other red wave at ω_2 is of less concern and can be exploited to achieve the required conditions on $\hat{v}_g$ and $\widehat{D}$. We can tilt the pump to

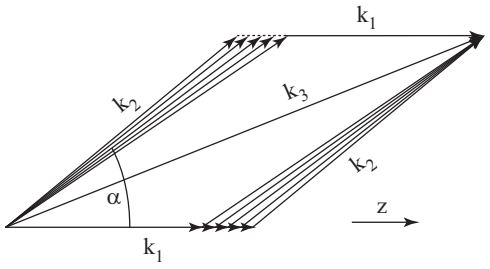

FIGURE 8.11. Phase matching diagram for chirped pulse optical parametric amplifier. The pump is tilted and nearly monochromatic, while the red waves are broadband, as indicate by the ranges of k-vectors. The input pulse is decomposed into parallel waves indicated by the set of vectors labeled k_1, while the internally generated pulse two consists of angle dispersed waves indicated by the set of vectors labeled k_2.

adjust the tilt and slant of pulse two. Fortunately, this allows nearly ideal adjustments to $\hat{v}_g$ and $\widehat{D}$ in many cases.

Figure 8.11 shows a k-vector diagram for CPOPA with a tilted pump beam (k_3) and nondispersed ω_1 beam. The ω_2 beam is angle dispersed as well as tilted so its carrier wave propagates at angle α. We show a fixed length k-vector for the pump because it has a much narrower bandwidth than the two red waves which are diagrammed with ranges of k-vectors necessitated by their broad bandwidths. Each frequency component of pulse one must phase match with its conjugate frequency component in pulse two. In other words, each conjugate pair (k_1, k_2) in the diagram must form a closed triangle with the pump k-vector (k_3), or, as we have redundantly diagrammed it, they must form a parallelogram with the pump k-vector forming the diagonal. Including all of the frequency components of the pulses leads to a set of parallelograms as shown in the figure.

Because we are assuming that all beams have infinite extent in the directions normal to $\hat{z}$, there is no range of k_x or k_y in either the k_3 or the k_1 vectors. This means the transverse component of each of the k_2 vectors must be equal to the transverse component of the pump vector. This is exactly the situation created when a large diameter ω_2 pulse with no angular dispersion is diffracted by a grating. Each wave in the first order diffracted pulse has a transverse k-vector component equal to the grating vector k_g, defined as $(2\pi/d_g)$ where d_g is the separation of grating grooves. This is shown in the left hand diagram of Fig. 8.12.

The corresponding time domain diagram is shown on the right in Fig. 8.12. The ω_2 pulse propagates with a tilt angle α and a pulse envelope slant of zero. The values of $\hat{v}_{g2}$ and $\widehat{D}_2$ are given by Eqs. (8.15) and (8.17) with

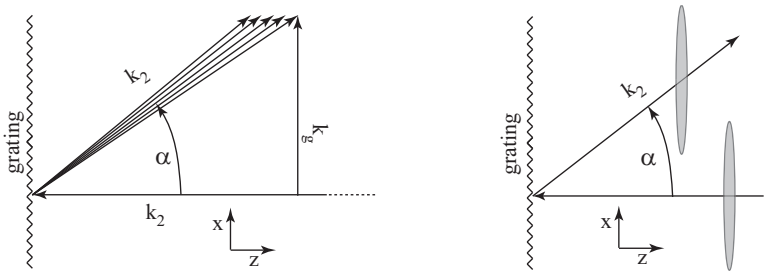

FIGURE 8.12. Model for the formation of the pulse at ω_2 as a pulse diffracted by a grating with vector k_g. Left diagram is in (k, ω) space; right diagram is in (r, t) space. The incident pulse in this artificial construction is composed of a set of monochromatic waves with parallel k-vectors indicate by the set of k_2 vectors incident on the grating. The reflected pulse consists of a set of angle dispersed waves, each with its transverse component equal to k_g which represents the transverse component of k_3. The tilt angle is (α=arcsin$[k_g/k_2]$)

$(\phi = 0)$,

$$\hat{v}_{g2} = v_{g2} \frac{\cos(\alpha + \rho_2)}{\cos \rho_2}, \tag{8.38}$$

$$\widehat{D}_2 = D_2 \frac{\cos \rho_2}{\cos(\alpha + \rho_2)} - A_2 \frac{1}{v_{g2}^2} \frac{\sin^2 \alpha \cos^3 \rho_2}{\cos^3(\alpha + \rho_2)}, \tag{8.39}$$

where ρ_2 is the birefringent walk off angle of beam two. The value of α is adjusted by changing the tilt angle of the pump beam. It is set to achieve, as nearly as possible, the ideal group velocity and GDD conditions, $(\hat{v}_{g1} = \hat{v}_{g2})$, $(\widehat{D}_1 = -\widehat{D}_2)$. The internal structure for chirped ω_1 and ω_2 pulses is shown in Fig. 8.13.

In CPOPA there is a reasonable likelihood of achieving simultaneous matching of apparent group velocities and apparent GDD coefficients for the two red pulses. Recall that the D_2 and A_2 coefficients in Eq. (8.39) are both positive in a normally dispersive crystal, so $\widehat{D}_2$ will be tuned toward negative values by increasing the pump angle, which increases α. $\widehat{D}_1$ is equal to D_1 which is usually positive. The value of $\hat{v}_{g2}$ also depends on ρ_2 and α_2. In general the problem of achieving ideal group velocity and GDD coefficients in any particular crystal by varying only α is over constrained. However, by choosing the right crystal from among a large selection of candidates, it is often possible to meet the requirements for broadband CPOPA.

Exercise 4 illustrates how to use Opoangles to search for broad phase matching of noncollinear parametric amplification.

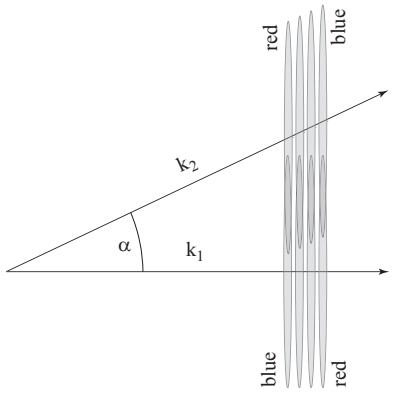

FIGURE 8.13. Structure of pulses in chirped pulse amplification with tilted pump beam. Ideally the apparent group velocities of waves one and two match and the apparent GDD's are equal and opposite so the red-to-blue and blue-to-red structures within the two pulses are exactly complementary.

Exercise 5 illustrates how use GVM to find the values of $\hat{v}_g$ and $\widehat{D}$ for noncollinear parametric amplification

In CPOPA the initial short ω_1 pulse is usually generated by a mode locked laser, often a Ti:sapphire laser, with a wavelength near 800 nm, and a duration of 10-100 fs. It is stretched by factors as high as 10^5 using diffraction gratings or prisms, producing linearly chirped pulses with durations of picoseconds or even nanoseconds. The pump pulse is often provided by a Q-switched laser such as a frequency doubled Nd:glass or Nd:YAG laser, operating on a single longitudinal mode to generate a pulse of 530 nm light with a duration of 100 ps to 10 ns. The wavelength of the second red wave in this scheme is 1580 nm. The energy in the original 800 nm pulse is typically a few nJ while the desired final pulse energy might be joules or kilo joules, so the required amplification can be 10^9 or more. Some of this gain might be provided by laser amplifier stages such as Yb^{3+}-doped silica fiber, or by Ti:sapphire rods or slabs, but the final several factors of ten are usually provided by a parametric amplifier. The bandwidth of a 10 fs pulse is approximately 1500 cm^{-1}, so phase matching must be good over the range 800±50 nm if we are to maintain the bandwidth of the amplified pulse and recompressibility to 10 fs.

Exercise 6 uses PW-mix-SP to illustrate numerical modeling of high gain CPOPA in the plane-wave limit.

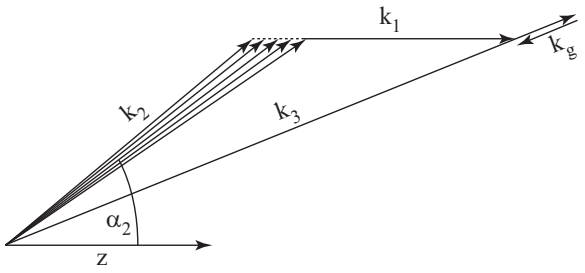

FIGURE 8.14. Noncollinear quasi phase matched CPOPA for pulse envelopes one and two normal to z and k_1. The tilt angle α_2 is set to match apparent group velocities $\hat{v}_{g1}$ and $\hat{v}_{g2}$. The vector $(\boldsymbol{k}_3+\boldsymbol{k}_g)$ closes the triangle.

8.3.6 Group velocity matched QPM mixing

CPOPA

Quasi phase matching introduces added flexibility in group velocity matching. Fig. 8.14 shows how CPOPA can be achieved in QPM assuming ($v_{g2} > v_{g1}$). The envelopes of pulses one and two are parallel to one another and perpendicular to k_1. The tilt angle of pulse two (α_2) is adjusted to make ($\hat{v}_{g1} = \hat{v}_{g2}$). The pump and QPM grating vectors (k_3 and k_g) close the phase matching diagram. The envelope structure of wave two corresponds to that in Fig. 8.12.

There is no birefringent walk off in most quasi phase matched crystals so the values of ρ are each zero in the equations for $\hat{v}_g$ and $\widehat{D}$. They become

$$\hat{v}_g = v_g \frac{\cos(\alpha+\phi)}{\cos\phi}, \tag{8.40}$$

$$\widehat{D} = D\frac{\cos\phi}{\cos(\alpha+\phi)} - \frac{1}{kv_g^2}\frac{\cos\phi\sin^2(\alpha+\phi)}{\cos^3(\alpha+\phi)}, \tag{8.41}$$

where we have discarded the F term in $\widehat{D}$ and used ($A = 1/k$). Matching apparent group velocities for pulses one and two requires

$$\alpha_2 = \arccos\left(\frac{v_{g1}}{v_{g2}}\right). \tag{8.42}$$

Matching $\hat{v}_{g1}$ and $\hat{v}_{g2}$ gives broad amplification bandwidth, but still broader bandwidth is possible if ($\widehat{D}_2 = -\widehat{D}_1$). Adjustment of α_2 alone is unlikely to meet this requirement while maintaining group velocity matching. However, adjusting both α_2 and $\phi_2(=\phi_1)$ may achieve the desired $\widehat{D}$ condition, but this means wave one is slanted, which may be unacceptable.

In principle the pump k-vector can point in any direction as long as the grating vector closes the phase matching diagram. In practice the grating

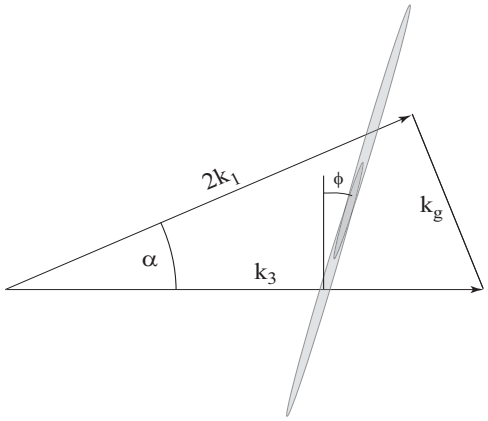

FIGURE 8.15. Noncollinear quasi phase matched and group velocity matched second harmonic generation. Angles α and ϕ are chosen to match apparent group velocities $\hat{v}_{g1}$ and $\hat{v}_{g2}$. The grating vector k_g closes the triangle.

vector should be as small as possible so the poling period is within practical limits. This requires the k_3 vector to be nearly parallel to the third side of the triangle formed by k_1 and k_2, as diagrammed in Fig. 8.14. The magnitude of k_g is always larger, and the poling period smaller, than for a collinear QPM process.

Exercise 7 illustrates noncollinear, group velocity matched, quasi phase matched CPOPA in ppLT.

SHG

Group velocity matched and quasi phase matched second harmonic generation is also possible[198, 199]. If the fundamental and second harmonic have the same polarization, the group velocity of the second harmonic is generally less than that of the fundamental, so group velocity matching requires slowing the fundamental pulse. This can be achieved by tilting the fundamental and using nonzero slant angle ϕ as shown in Fig. 8.15. The quasi phase matching grating is chosen to make ($\Delta k = 0$), and will be tilted. Group velocity matching requires α and ϕ angles that satisfy

$$\hat{v}_{g1} = v_{g1}\frac{\cos(\alpha+\phi)}{\cos\phi} = v_{g3}. \tag{8.43}$$

For broadest bandwidth we would also satisfy

$$\widehat{D}_1 = 2\widehat{D}_3, \tag{8.44}$$

but this is nearly impossible to achieve.

Once a group velocity matched geometry is found it is straightforward to compute the quasi phase matching grating needed to meet the phase match requirement ($\Delta k_z = [k_3 - 2k_1 \cos\alpha_1 - k_{gz}] = 0$) and ($\Delta k_x = [2k_1 \sin\alpha_1 - k_{gx}] = 0$). It is important to make sure the grating period is long enough to be practical. If a geometry with ($\phi = 0$) is chosen, the QPM grating vector must be large so it will accommodate the transverse phase mismatch. Longer grating periods are possible if ($\phi > 0$) because this reduces α. The transverse mismatch can be avoided by splitting the fundamental into two parts, one propagating with angle α, the other with angle $(-\alpha)$. This requires ($\phi = 0$), of course.

Exercise 8 illustrates noncollinear, quasi phase matched and group velocity matched SHG of 1550 nm light in ppLN.

Three pulse mixing

For the more general case where we wish to match the group velocities of three different pulses we can slow the two faster pulses to match the slowest group velocity by tilting them. Assuming wave three is the slowest, we can adjust α_1 and α_2 with ($\phi = 0$) to match all three group velocities. The quasi phase matching grating is then chosen to null the transverse and longitudinal components of Δk. To obtain practical poling periods it may be necessary to use a nonzero ϕ as well. This makes it possible to use smaller tilts to achieve the desired group velocity reduction, and that generally leads to longer, more practical grating periods.

8.3.7 Snell's law of slants

To take advantage of pulse slants it is necessary to know how they transform when the pulse enters or exits a crystal. We define angle γ as the slant relative to the normal to the k vector. We can derive a relation between incident and transmitted γ similar to Snell's law that relates incident and transmitted directions of the k vector. We begin by using the diagram in Fig. 8.16 to express the apparent group velocity along the input face of the crystal $\hat{v}_x$ as

$$\hat{v}_x = \frac{\hat{v}_g}{\tan\phi}. \tag{8.45}$$

Using Eq. (8.15) this can be written

$$\hat{v}_x = v_g \frac{\cos(\alpha + \phi + \rho)}{\sin\phi \cos\rho}, \tag{8.46}$$

and using ($\gamma = \phi + \alpha$) this becomes

$$\hat{v}_x = v_g \frac{\cos(\gamma + \rho)}{\sin(\gamma - \alpha)\cos\rho}. \tag{8.47}$$

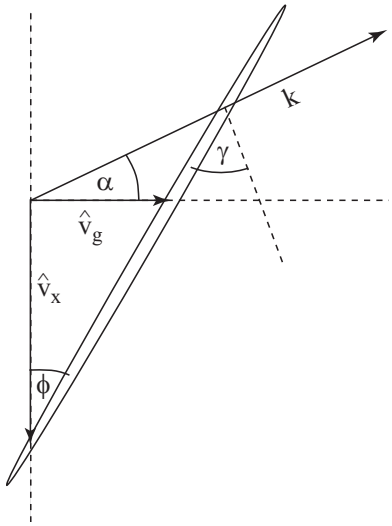

FIGURE 8.16. Angles for deriving $\hat{v}_x$ for a slanted pulse.

Let the pulse travel from crystal 1 with refractive index n and group velocity index n_g to crystal 2 with refractive index n' and group velocity index n'_g. The continuity condition on the pulse envelope across the boundary is $(\hat{v}_x = \hat{v}'_x)$ so

$$v_g \frac{\cos(\gamma + \rho)}{\sin(\gamma - \alpha)\cos\rho} = v'_g \frac{\cos(\gamma' + \rho')}{\sin(\gamma' - \alpha')\cos\rho'}. \tag{8.48}$$

subject to Snell's law

$$n \sin\alpha = n' \sin\alpha'. \tag{8.49}$$

The last two equations can be solved for γ' which can then be used to calculate $\hat{v}'_g$.

For example, suppose a pulse with zero slant ($\gamma = 0$) in air is obliquely incident on an optically isotropic window or prism ($\rho' = 0$). Equation (8.48) becomes

$$v_g \frac{1}{\sin(-\alpha)} = v'_g \frac{\cos(\gamma')}{\sin(\gamma' - \alpha')}, \tag{8.50}$$

with

$$\sin\alpha = n' \sin\alpha'. \tag{8.51}$$

Combining the last two equations gives

$$\tan\gamma' = \frac{\sin\alpha}{[1 - (1/n')^2 \sin^2\alpha]^{1/2}} \left(\frac{1}{n'} - \frac{1}{n'_g} \right). \tag{8.52}$$

9
Optical parametric generation (OPG)

Here optical parametric generation (OPG) means the single-pass parametric amplification of quantum noise to the point of noticeable pump depletion and beyond. It is attractive as a relatively simple means of frequency down-conversion because it dispenses with the optical cavity used in an OPO. The longitudinal cavity modes of an OPO are absent, yielding a less structured output spectrum. However, we will see that relative to an OPO, OPG is likely to sacrifice conversion efficiency, spectral control, beam quality, and pulse-to-pulse stability.

Optical parametric generation relies on parametric amplification of the quantum background which fills all possible spatial and temporal modes. The amplified output light may be spectrally broad and have poor beam quality. It is possible to improve the OPG spectrum, beam quality, and efficiency by adding a narrow bandwidth seed beam that overpowers the quantum background. A few microwatts or milliwatts is usually sufficient. With or without seeding, OPG efficiency can be quite high, with reported efficiencies up to 70%[205], but it is usually considerably lower than that.

Optical parametric generation requires a much higher single pass gain than an OPO, making optical damage more likely. OPG has been demonstrated in a variety of nonlinear crystals using short pump pulses (ps or fs) where the irradiance damage limit is high, but for nanosecond and longer pump pulses, OPG is limited to long crystals with high nonlinearity, usually quasi phase matched $LiNbO_3$ (ppLN), $LiTaO_3$ (ppLT), KTP (ppKTP), or GaAs (opGAAS). There are only a few reports of OPG in birefringently

phase matched crystals when the birefringent walk off is greater than a small fraction of the pump diameter[206, 207, 208, 209].

In most OPG demonstrations a Gaussian pump beam is focused so its Rayleigh range is approximately equal to the crystal length L. For this focusing condition, when spatial and temporal walk offs are insignificant the threshold pump power is approximately proportional to $(1/L)$, so the peak irradiance at the focal waist at threshold is proportional to $(1/L^2)$. Using longer crystals to take advantage of this scaling is important if optical damage lurks or if the available pump power is limited. Longer crystals also help avoid problems caused by higher order nonlinearities such as the intensity-dependent refractive index (n_2) and two-photon absorption (β). However, if generation of the shortest possible pulses is desired, the crystal must be short enough that the temporal walk off is not much greater than the pump duration.

Optical parametric fluorescence (OPF) is closely related to OPG. It also involves parametric amplification of quantum noise, but the gain is much lower, leading to countable numbers of generated photons and negligible pump depletion. It is often used as the source of correlated and entangled photons. It can also be used to measure second order nonlinear optical coefficients, as discussed in Sec. 17.1.2

The amplitude of the initiating quantum noise is half a photon per mode on average, or approximately (10^{-19} J) per mode. Many modes are sometimes amplified, raising the initial noise level to perhaps 10^{-16} J. Pump levels usually lie in the nanojoule to millijoule range, so the threshold gain is typically in the vicinity of 100 dB. In most other applications of nonlinear crystals the input irradiances need be only a few times the characteristic irradiance $S_\circ$ to achieve high mixing efficiency. In contrast, achieving a threshold gain near 100 dB requires pump irradiances near $(100\times S_\circ)$.

The high gain of OPG implies that the red waves are strongly modified by gain over a mere 5% of the crystal length. In contrast, when the pump is focused so the Rayleigh length is equal to the crystal length, the diffractive length for the red beams is roughly the full crystal length. The dispersive counterpart of the Rayleigh range is the dispersion length defined by $(z_D = \tau^2/2D)$. The value of D for ppLN near 1000 nm is roughly 250 fs^2/mm. For this value a 100 fs pulse would have a dispersion length of 20 mm, again much longer than the gain length even in a 50 mm long crystal. Temporal walk off lengths are also usually long compared with the gain length. The implication is that parametric gain tends to overpower diffraction and dispersion to a much greater extent than in most non-OPG mixing applications.

The high gain of OPG also means there is only a small window of pump power between threshold and the onset of back conversion. Back conversion is present in most OPGs pumped at more than 1.25 times threshold and is

the primary cause of the beam quality degradation and spectral broadening observed whenever an OPG is pumped much above threshold.

The rate of energy transfer from the pump to the red pulses as they propagate is proportional to the local product of the three optical fields. This tends to lock the pulses together. The high gain of OPG can reshape the red pulses, preventing them from separating at the rate predicted by their group velocities. Similarly, the red beams tend to be entrained by the pump beam. At pump levels well above threshold, past the point in the crystal where the pump becomes depleted and the gain is reduced, this pulse/beam locking is defeated, and walk off, dispersion, and diffraction may dominate near the output end of the crystal, strongly influencing the output beam/pulse profile, spectra, and efficiency.

To optimize OPG sources in terms of spectral line width, beam quality, and efficiency it is common practice to use multiple stages of OPG in which the first stage supplies most of the gain but low conversion, while a second, low-gain stage provides the bulk of the energy conversion. Between these stages the light can be spectrally or spatially filtered to optimize overall performance.

We discuss all these topics in detail below. We begin by considering temporal/spectral effects in the absence of diffraction or birefringent walk off, using a plane wave, dispersive OPG model. This simplifies the initial discussion, emphasizing the roles of temporal walk off and gain. We will follow by adding spatial effects, including pump spatial profiles, diffraction, red wave tilts, and birefringent walk off. We will explore different focusing conditions, crystal lengths, temporal walk offs, tilted waves, seeding, back conversion, pump bandwidths, and more.

9.1 OPG pump threshold estimate

To estimate the threshold gain we first consider the simplest case where the pump pulse is long compared with any group velocity walk off pulses, and long compared with any GDD-induced stretching of the pulses. We also assume parallel Poynting vectors with small diffractive spreading of the beams, permitting the use of plane wave propagation and mixing equations. Threshold is reached when the pump pulse is slightly depleted at its peak.

According to Eq. (3.88) the parametric gain of the red1 irradiance, in the monochromatic, plane wave limit, assuming an undepleted pump, no red2 input, and ($\Delta k = 0$), is

$$\Gamma_1 = \sinh^2(\gamma L), \tag{9.1}$$

where L is the crystal length, and

$$\gamma L = \sqrt{\frac{S_3}{S_\circ}}. \tag{9.2}$$

Here S_3 is the irradiance of the blue (pump) pulse and $S_\circ$ is the usual reference irradiance for this process, defined by

$$S_\circ = \frac{\epsilon_\circ c^3 n_1 n_2 n_3}{2 d_{\text{eff}}^2 \omega_1 \omega_2 L^2}. \tag{9.3}$$

For large gains the sinh function in Eq. (9.1) can be approximated as

$$\sinh(\gamma L) = \frac{1}{2} e^{\gamma L}, \tag{9.4}$$

leading to

$$\Gamma_1 = \frac{1}{4} e^{2\gamma L} = \frac{1}{4} \exp\left(2\sqrt{\frac{S_3}{S_\circ}} \right). \tag{9.5}$$

For a Gaussian pump pulse of duration τ, Gaussian waist w (both at I_M/e^2), and pulse energy $\mathcal{U}_3$, the peak pump irradiance at the pulse and beam center is

$$S_{3M} = \frac{\mathcal{U}_3}{(\pi/2)^{3/2}\ \tau w^2}. \tag{9.6}$$

The average noise irradiance of the red1 beam at its pulse and beam center, in a beam with the same shape as the blue beam, is at least

$$S_{1M} = \frac{h\nu_1}{(\pi/2)^{3/2}\ \tau w^2}. \tag{9.7}$$

It is many times larger than this if many frequency modes can be amplified. In order to deplete the pump irradiance by 10% at pulse/beam center, the red1 irradiance must be amplified from this initial value of S_{1M} to

$$S_1 = 0.1\ \frac{\nu_1}{\nu_3}\ S_{3M}. \tag{9.8}$$

Using Eq. (9.5) we write this threshold condition as

$$0.1\ \frac{\nu_1}{\nu_3}\ S_{3M} = 0.25\ S_{1M}\ \exp\left(2\sqrt{\frac{S_{3M}}{S_\circ}} \right), \tag{9.9}$$

or, in terms of the pulse energy for a spatial and temporal Gaussian pump,

$$0.4 \frac{\mathcal{U}_{\text{th}}}{h\nu_3} = \exp\left(2\sqrt{\frac{\mathcal{U}_{\text{th}}}{(\pi/2)^{3/2}\ \tau w^2\ S_\circ}} \right) \approx \exp\left(\sqrt{\frac{2\ \mathcal{U}_{\text{th}}}{\tau w^2\ S_\circ}} \right). \tag{9.10}$$

Taking the logarithm of both sides and squaring gives the pump threshold energy condition

$$\ln^2 \left[0.4 \frac{\mathcal{U}_{\text{th}}}{h\nu_3} \right] = \frac{2\ \mathcal{U}_{\text{th}}}{\tau w^2\ S_\circ}. \tag{9.11}$$

An important point is that $\mathcal{U}_{\rm th}$ estimated this way depends on the crystal properties and the wavelengths through parameter $S_\circ$, and on the pump beam waist w and pulse duration τ. The threshold deduced from Eq. (9.11) would be increased by temporal walk off of the red waves from the pump, by diffractive spreading of the pump beam, or by any loss of the red beams. It would be slightly decreased if many red frequency modes can be amplified.

Using Eq. (9.11) we find that typical threshold gains are in the range of 100-150 dB and the ratio $(S_3/S_\circ)$ at threshold is in the range 150-300. To increase the conversion efficiency from 0.1 to nearly 1.0, another 10 dB of gain is necessary, requiring at least a 20% increase in pump energy. The efficiency computed over the full pulse and beam profiles rather than at the pulse/beam center is still quite low at this pump level, so stronger pumps are frequently used to improve efficiency, but this causes back conversion near the pump pulse/beam center.

9.2 OPG gain bandwidths

The high parametric gain required for OPG substantially alters the spectral acceptance bandwidth of the red waves. At low gain the bandwidth is defined by the condition $(\Delta kL = 2\pi)$ but at higher gain the bandwidth broadens. According to Sec. 3.4, the plane wave parametric gain expression, now including Δk, is

$$\Gamma_1 = \frac{S_3}{S_\circ}\left|\frac{\sinh(\gamma L)}{\gamma L}\right|^2, \tag{9.12}$$

where

$$\gamma L = \sqrt{\frac{S_3}{S_\circ} - \left(\frac{\Delta kL}{2}\right)^2}. \tag{9.13}$$

In Fig. 9.1 we plot the plane wave gain profiles versus the phase mismatch ΔkL for three values of $S_3/S_\circ$: [1, 150 (100 dB gain), 323 (150 dB gain)]. The broadened profiles at typical OPG gains imply red OPG spectra that are broader than the low gain bandwidth

$$\Delta\nu_{12} = \frac{1}{|\tau_{12}|} = \frac{c}{L|n_{g1} - n_{g2}|}. \tag{9.14}$$

For typical OPG gains the linewidth is approximately 2.5 times broader than the low gain limit and, because it grows slowly with increasing gain, we somewhat arbitrarily define the OPG acceptance bandwidth as $(\Delta kL = 16)$. This width applies near the OPG threshold. For higher pump levels back conversion may further broaden the linewidth.

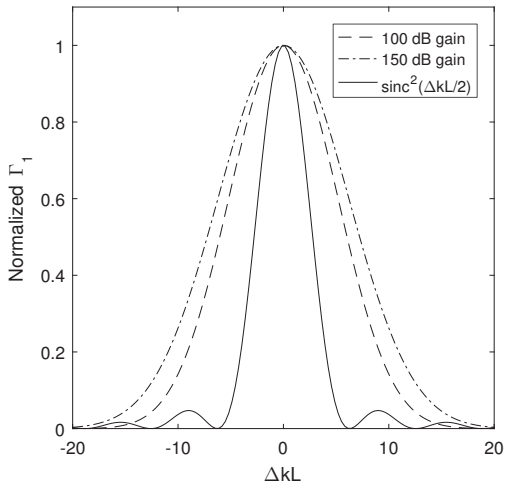

FIGURE 9.1. Plane wave parametric gain Γ_1 defined in Eq. (9.12) versus phase mismatch ΔkL for three values of $S_3/S_\circ$. The narrow curve is the familiar $\text{sinc}^2(\Delta kL/2)$ function. The dashed and chained curves are the gain profiles for 100 dB ($S_3/S_\circ = 150$) and 150 dB ($S_3/S_\circ = 323$) gains. The widths (FWHM) of the high gain curves are 2.2 and 2.7 times that of the sinc^2 function.

9.3 OPG numerical modeling

Most of the discussion in this chapter is based on numerical modeling, so it is important to understand what is included in our models. Numerical methods for OPG are much the same as for other frequency mixing processes. Beam propagation methods which incorporate accurate treatments of diffraction, dispersion, phase matching, and nonlinear mixing, including pump depletion, are used to compute output fields $E_i(x, y, t)$, from which we calculate mixing efficiency, beam quality, pulse quality, beam tilts, and so on. One difference from other mixing is the extreme gain of OPG which requires the size of the propagation steps be much smaller. Typically $(300 - 500)$ z-steps are used. High transverse spatial resolution is also necessary if the pump significantly exceeds threshold. The beams often develop fine spatial structure, in particular strong irradiance spikes near the beam center. At locations downstream from the first back conversion the red waves can also develop large tilts, so keeping the beams fully contained within the spatial grid may require large grids. This combination of large beams and fine spatial structure demands high spatial resolution. The red spectra also broaden with increasing pump strength so high time resolution is necessary. The resulting small step sizes in $\{x, y, z, t\}$ makes for a slow model demanding a large memory. Educated adjustments of the grid sizes

and resolutions to ensure convergence of the model without wasting computer resources is an important aspect of OPG modeling. Model runs for full dispersive/diffractive models typically require a few minutes to an hour. Systematic studies varying parameters take much longer. For this reason, we attempt to explain here the broad outlines of OPG behavior, based on extensive modeling studies. We hope you will be able use this knowledge to more efficiently explore the details of your OPG.

The SNLO function OPG uses beam propagation methods to model OPG. It incorporates diffraction, dispersion, nonlinear mixing, starting quantum noise, and phase matching to produce physically realistic results.

9.3.1 Quantum noise simulation

Because OPG is initiated by quantum noise, adequate simulations of that noise are essential. In general we include both spatial and temporal noise for both red waves. In Sec. 5.5 we explained how we treat all optical fields as classical fields, so we do not use a true quantum treatment of the noise. Instead, we use a stochastic electrodynamics treatment[143]. Each optical mode which might possibly be amplified is populated with a classical field with stochastic properties suitably chosen to approximate quantum noise. Specifically, the average energy per mode is $(h\nu/2)$, and the energy distribution among the modes is Gaussian with a random phase distribution[143, 144]. Model results when populating one red wave at $(h\nu)$ or both red waves at $(h\nu/2)$ are usually indistinguishable, but we always populate both waves.

To construct the noise we must define the modes and determine which modes to include in a simulation. Our approach is to include noise in as many modes as possible under the numerical constraints. We assign noise with a mean value of $(h\nu/2)$ to each volume element of the $\{x, y, t\}$ grid. That is

$$< U_{\text{noise}} >= \Delta x \Delta y \Delta t \frac{\epsilon_\circ c}{2} < |E|^2 >= \frac{h\nu}{2}. \tag{9.15}$$

Defining volume V by

$$V = \Delta x \Delta y \Delta t, \tag{9.16}$$

the mean square of the field is written

$$< |E|^2 >= \left[\frac{h\nu}{\epsilon_\circ c V}\right]. \tag{9.17}$$

The noise field is a set of fields $\{E\}$, one for each grid volume element, given by

$$\{E\} = \left[\frac{h\nu}{\epsilon_\circ c V}\right]^{1/2} \big[-\ln\{R\}\big]^{1/2} \big[\cos\{\phi\} + i\sin\{\phi\}\big], \tag{9.18}$$

propagating in the opposite direction, right to left, the response is two upward fields create a polarization directed to the left, which means d_{eff} is negative. Thus for the same crystal sample, d_{eff} can change sign depending its orientation. One way to analyze this is to keep the propagation direction fixed in space while we change the orientation of the crystal, keeping all field directions fixed to the crystal with the assurance that the directions are then physically related to the nonlinearity of the crystal. In the laboratory frame these rotations change the directions of the optical fields. We can rotate about three axes as shown in Fig. 16.2, demonstrating that for a single crystal there are four orientations that phase match and have the same magnitude of d_{eff}. However, the sign of d_{eff} changes depending on the orientation of the crystal. If the sign of d_{eff} is positive for the orientation shown in Fig. 16.2(a) it is also positive for the orientation in (b) but negative for the orientations in (c) and (d). This example uses the *e*- and *o*-polarized waves of a uniaxial crystal, but the same arguments obviously apply to the orthogonal polarizations of a biaxial crystal if the crystal is rotated 180° about one of the eigenpolarization directions or about the propagation direction.

16.4.2 d_{eff} surface

We can pick one set of eigenpolarizations and calculate d_{eff} for all propagation directions to form a $|d_{\text{eff}}|$ surface such as that shown in Fig. 16.3. This example is for $KNbO_3$ with two waves polarized along the *hi* index direction and one polarized along the *lo* index direction. Reversing the propagation direction does not change $|d_{\text{eff}}|$ so we need to calculate d_{eff} for only 4 of the eight octants. We chose $(x > 0)$ for this example, but we could have chosen the four with $(y > 0)$ or the four with $(z > 0)$ just as well. The $|d_{\text{eff}}|$ surface reflects the underlying crystal symmetry. Our example crystal, $KNbO_3$, is unchanged by rotation of 180° about $\hat{x}$ or by reflection in the $(y = 0)$ or $(z = 0)$ planes.

The phase matching loci in biaxial crystals form loops around one of the principal axes or, rarely, around the optic axes[37]. It is convenient to specify phase matching angles using polar angle θ and azimuthal angle ϕ measured relative to the encircled axis. Plots of θ and $|d_{\text{eff}}|$ as functions of ϕ are then single valued and easy to interpret. The phase matching loops traverse four octants. In crystals with lowest possible symmetry, the four octants are different so a complete specification of $|d_{\text{eff}}|$ requires a plot over 360° in ϕ. I know of no reports of applications of nonlinear crystals with such low symmetry. More symmetric crystals require a plot of $|d_{\text{eff}}|$ over only one or two octants. For example, the phase matching loci for second harmonic generation of 1064 nm light in $KNbO_3$ loop around the x-axis. Only a single octant is necessary for this crystal.

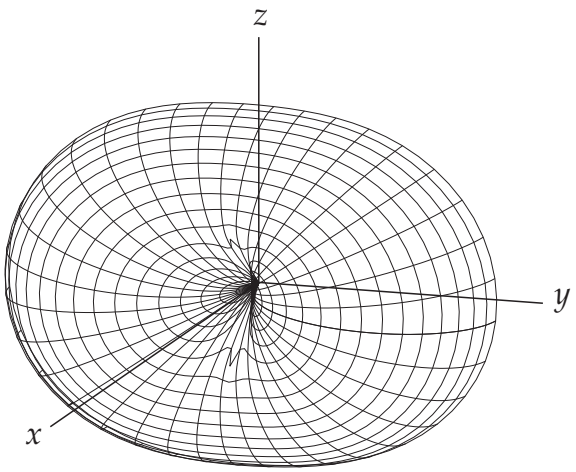

FIGURE 16.3. The values of d_{eff} for $KNbO_3$ versus propagation angle. The polarizations are: one *lo* and two *hi*. The rear half of the surface ($x < 0$) is a mirror image of the front ($x > 0$) half.

The SNLO function BMIX allows the user to specify the reference axis for plots of θ, d_{eff} and other properties.

The phase matching loci in uniaxial crystals always form circles about the z-axis at constant θ. Simple expressions give d_{eff} as a function of ϕ and it is customary to specify a crystal as either type I or type II depending on whether ϕ is chosen to maximize d_{eff} for mixing with one e-wave or two.

16.5 Crystal symmetry and $\boldsymbol{d}$

The forms of both the d and ϵ tensors depend on how the reference frame in which they are specified is oriented relative to the lattice structure of the crystal, and also on the symmetry properties of the crystal's unit cell. To account for this we consider two reference systems, a crystallographic system that is tied to the crystal lattice, and an optical system that we superimpose on it. The crystallographic system axes are labeled (a, b, c) and the optical system axes are labeled $(\hat{x}, \hat{y}, \hat{z})$. Figure 16.4 shows the labeling convention. The optical system is orthogonal but the crystallographic system is not

necessarily orthogonal. Both systems are right handed meaning ($\hat{x} \times \hat{y} = \hat{z}$) and ($(a \times b) \cdot c > 0$). Various other reference frames abound in the literature but these two are sufficient and by using only two reference frames I hope to minimize confusion. In specifying the crystallographic frame relative to

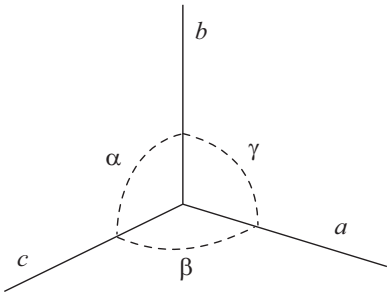

FIGURE 16.4. Crystallographic axis convention.

the crystal lattice we will try to use the established conventions, but often ambiguity remains and we will discuss this when it occurs.

There is always an orientation of the optical frame in which ϵ is diagonal with ($\epsilon_{xx} \leq \epsilon_{yy} \leq \epsilon_{zz}$). We will use this frame to specify both ϵ and $\boldsymbol{d}$. There is ambiguity here as well because rotation of the optical frame by 180° about any of its axes will also be a frame meeting this criterion, so we will be alert to the implications of this ambiguity as well. For biaxial crystals the orientation of $(\hat{x}, \hat{y}, \hat{z})$ is fixed relative to (a, b, c) by these standards. For uniaxial crystals we will label the optical axis $\hat{z}$ and it will lie along a crystal symmetry axis that is conventionally labeled c. Orienting $\hat{z}$ along this direction is sufficient to diagonalize ϵ but it leaves the orientation of the $\hat{x}$ and $\hat{y}$ axes undefined. We must specify their orientations relative to (a, b, c) if $\boldsymbol{d}$ is to be uniquely specified. For isotropic crystals ϵ is diagonal for all orientations of $(\hat{x}, \hat{y}, \hat{z})$ so we pick a convenient orientation relative to (a, b, c), for example ($\hat{x} = \hat{a}$, $\hat{y} = \hat{b}$, $\hat{z} = \hat{c}$). Some crystals exist in two distinct mirror image, or enantiomorphic, forms. The right handed form is assumed unless stated otherwise.

Before we proceed further, a little knowledge of crystallography is essential. Our discussion is based largely on the treatments presented in books by Cady[466], Kittel[467], Butcher[468], and Boyd[14]. Perfect crystals consist of identical unit cells stacked in space, each situated identically with respect to its neighboring cells to form a crystal lattice. The unit cell is the smallest parallelepiped out of which the crystal could be constructed. There are seven types of unit cells that can be used to fill space. They are listed in Table 16.5 along with a description of their shape specified by the lengths of three adjacent sides (a, b, c) and the included angles (α, β, γ)

using the labeling conventions shown in Fig. 16.4. The set of axes (a, b, c) is the crystallographic reference frame.

TABLE 16.5. Crystal System Properties

System	Unit cell	Unit cell angles	Type
Triclinic	$a \neq b \neq c$	$\alpha \neq \beta \neq \gamma$	biaxial
Monoclinic	$a \neq b \neq c$	$\alpha = \gamma = 90^\circ \neq \beta$	biaxial
Orthorhombic	$a \neq b \neq c$	$\alpha = \beta = \gamma = 90^\circ$	biaxial
Tetragonal	$a = b \neq c$	$\alpha = \beta = \gamma = 90^\circ$	uniaxial
Trigonal	$a = b = c$	$90^\circ \neq \alpha = \beta = \gamma \leq 120^\circ$	uniaxial
Hexagonal	$a = b \neq c$	$\alpha = \beta = 90^\circ\ \gamma = 120^\circ$	uniaxial
Cubic	$a = b = c$	$\alpha = \beta = \gamma = 90^\circ$	isotropic

Each unit cell contains an identical array of atoms located at fixed positions relative to the cell. The symmetry of this array of atoms is in general lower than that of the unit cell. At most its symmetry equals that of the unit cell. It is known from group theory that there are 32 point symmetries possible for the atomic structure. Point symmetries are defined by covering operations such as rotation, reflection, and inversion about a point that leave the appearance of the crystal unchanged. Table 16.6 lists the point symmetry classes along with some familiar examples. If T is a covering operation, the transformed $\boldsymbol{d}$ must be the same as the original because the appearance of the crystal has not changed. Thus

$$\epsilon_{ij} = \epsilon'_{ij} = T_{ir} T_{js} \epsilon_{rs} \ , \tag{16.30}$$

and

$$d_{ijk} = d'_{ijk} = T_{ir} T_{js} T_{kt} d_{rst} \ . \tag{16.31}$$

The name of each crystal class reflects its symmetries or covering operations. Numbers indicate rotation symmetry. For example the number 2 indicates that the crystal appears unchanged by rotation through 180°, 3 means it is unchanged by rotation through 120°, etc. A bar over the number indicates that rotation plus inversion is a covering operation. For example $\bar{3}$ means rotation by 120° plus inversion is a covering operation. Symmetry on reflection in a plane is indicated by m. We will briefly discuss each class and the corresponding properties of ϵ and $\boldsymbol{d}$ beginning with the least symmetric class and progressing to the most symmetric.

As is well known, a second order nonlinear response requires an asymmetric medium. We will see that only 20 (18 when Kleinman symmetry is assumed) of the 32 crystal classes have asymmetry that can support a second order response. These are indicated in the Table 16.6.

TABLE 16.6. Crystal symmetry classes

Crystal system	Crystal class	Schoenflies	$\boldsymbol{d} \neq 0$	common name
Triclinic	1	C_1	yes	
	$\bar{1}$	C_i or S_2	no	
Monoclinic	2	C_2	yes	
	m	C_s or C_{1h}	yes	
	$2/m$	C_{2h}	no	
Orthorhombic	222	D_2 or V	yes	
	$mm2$	C_{2v}	yes	
	mmm	D_{2h} or V_h	no	
Tetragonal	4	C_4	yes	
	$\bar{4}$	S_4	yes	
	$4/m$	C_{4h}	no	
	422	D_4	no	
	$4mm$	C_{4v}	yes	
	$\bar{4}2m$	D_{2d} or V_d	yes	chalcopyrite
	$4/mmm$	D_{4h}	no	
Trigonal	3	C_3	yes	
	$\bar{3}$	C_{3i} or S_6	no	
	32	D_3	yes	
	$3m$	C_{3v}	yes	
	$\bar{3}m$	D_{3d}	no	
Hexagonal	6	C_6	yes	
	$\bar{6}$	C_{3h}	yes	
	$6/m$	C_{6h}	no	
	622	D_6	no	
	$6mm$	C_{6v}	yes	wurtzite
	$\bar{6}m2$	D_{3h}	yes	
	$6/mmm$	D_{6h}	no	
Cubic	23	T	yes	
	$m3$	T_h	no	
	432	O	no	
	$\bar{4}3m$	T_d	yes	zinc blende
	$m3m$	O_h	no	

Values for $\boldsymbol{d}$ are not tabulated in this book. The SNLO values are kept up to date, and used by SNLO in its calculations. To view the SNLO $\boldsymbol{d}$, run Qmix and select the crystal. The corresponding $\boldsymbol{d}$ tensor is displayed in the text window of the Qmix form, along with its crystal class.

16.5.1 Enantiomorphism

It is possible for crystals without mirror or inversion symmetries to exist in two distinct mirror image forms, or enantiomorphs. Crystal classes in which enantiomorphism is allowed include classes (1, 2, 222, 4, 422, 3, 32, 6, 622, 23, 432) of which all but (422, 622, 432) have nonzero $\boldsymbol{d}$. The two mirror image crystal forms are traditionally called left-handed and right-handed because all enantiomorphic classes also all exhibit optical activity. The right-handed form of the crystal rotates linearly polarized light clockwise as viewed looking into the beam, while the left-handed form rotates it counter clockwise.

The mirror symmetry of enantiomorphs is perfect, so all physical attributes are the same for the two forms if they are described in mirror image reference systems. It is customary to quote $\boldsymbol{d}$ for the right-handed crystal form as expressed in a right-handed reference system, which is the same as that for the left-handed form described in a corresponding left-handed reference system. We illustrate this in Fig. 16.5. The left half of the figure shows the right handed form of a crystal unit cell along with a standard, right-handed (x, y, z) reference frame. The orientation of (x, y, z) must be specified relative to the unit cell structure if we are to have a unique determination of $\boldsymbol{d}$. For the triclinic class unit cell shown in the figure, the standard orientation of (a, b, c) is $(c < a < b)$ and $(\alpha, \beta > 90°)$. The origin of this uniquely defined crystallographic frame is marked by the dot.

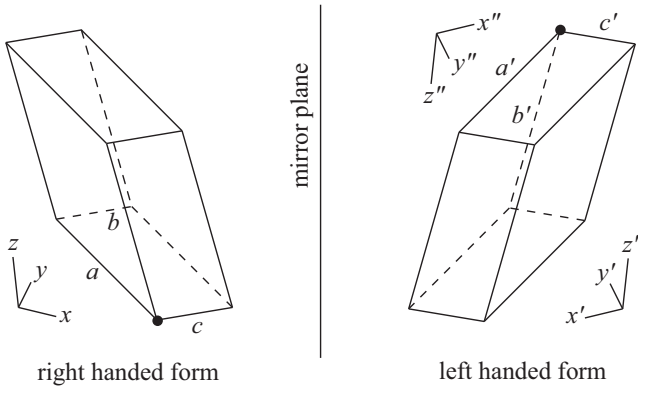

FIGURE 16.5. Mirror image crystal structures and associated crystallographic and optical reference systems.

The right half of Fig. 16.5 shows the mirror image, or left-handed, unit cell, along with the mirror image reference frame (x', y', z'). If (x, y, z) is used for the right-handed enantiomorph and (x', y', z') is used for the left-handed enantiomorph, all the properties of the two forms are identi-

cal, including the $\boldsymbol{d}$ tensor. Notice that (x', y', z') is a left-handed frame. If we invert all of its axes we have the right-handed frame (x'', y'', z''). However, inverting all the axes inverts the sign of $\boldsymbol{d}$ so, expressed in the (x'', y'', z'') frame, all of the d_{ijk} terms of the left-handed crystal are the negative of those for the standard right-handed crystal. Finally, notice that if we apply our standard rule for orienting the crystallographic frame to the left-handed crystal, we arrive at the right-handed frame (a', b', c') with its origin indicated by the dot. This frame has the same orientation relative to (x'', y'', z'') that frame (a, b, c) has relative to (x, y, z). We conclude that if we use right-handed crystallographic and reference frames for both crystal forms, and follow the standard rule for orienting the crystallographic axes, the sign of $\boldsymbol{d}$ is opposite for right- and left-handed enantiomorphs.

16.5.2 Gyrotropy

Gyrotropy is optical activity or the rotation of linearly polarized light on propagation through material[4]. It was discussed in Chapter 2 in connection with the linear optical properties of crystals. All enantiomorphic crystals can exhibit gyrotropy with the two enantiomorphs giving opposite directions of polarization rotation so a measurement of the rotation direction provides a convenient way to distinguish between enantiomorphs. Some nonenantiomorphic crystals (classes m, $mm2$, $\bar{4}$, and $\bar{4}2m$) can also exhibit gyrotropy. In birefringent crystals the birefringence normally overwhelms the gyrotropy so no rotation is evident unless the propagation direction lies along an optical axis where birefringence disappears. Among the nonbirefringent crystal classes only classes 432 and 23 are gyrotropic. Both of these are enantiomorphic and the sign of the rotation depends on whether the crystal is a right or left enantiomorph. In these two classes gyrotropy is equal valued for all propagation directions.

16.5.3 Ferroelectricity and poling

Distinguishing characteristics of ferroelectric crystals are that they belong to one of the 10 ferroelectric classes with a polar axis, classes (1, 2, m, $mm2$, 4, $4mm$, 3, $3m$, 6, $6mm$), that they have a spontaneous polarization along a polar axis which can be reversed by a sufficiently strong applied electric field, that they show dielectric hysteresis, and that they have a domain structure. Above the Curie temperature these ferroelectric properties are absent. All ferroelectric crystal classes also have second-order nonlinearity, but not all nonlinear crystal classes are ferroelectric. Just because a crystal species is a member of a ferroelectric crystal class does not mean it must be ferroelectric. It only means ferroelectricity is not forbidden by symmetry. Among commonly used nonlinear crystals, $KNbO_3$, crystals of the KTP

References

[1] M. Born and E. Wolf. *Principles of Optics*. Pergamon Press, 1991.

[2] B. Wyncke and F. Brehat. Calculation of the effective second-order non-linear coefficients along the phase matching directions in acentric orthorhombic biaxial crystals. *J. Phys. B: At. Mol. Opt. Phys.*, 22:363–376, 1989.

[3] F. Brehat and B. Wyncke. Calculation of double-refraction walk-off angle along the phase-matching directions in non-linear biaxial crystals. *J. Phys. B: At. Mol. Opt. Phys.*, 22:1891–1898, 1989.

[4] J.F. Nye. *Physical Properties of Crystals*. Oxford Univ. Press, 1964.

[5] Z. Huang, D. French, H.-Y. Pao, and I. Jovanovic. Assessment of image resolution improvement by phase-sensitive optical parametric amplification. *Appl. Phys. B*, 10.1007/s00340-10-4101-z:1–7, 2010.

[6] R.L. Sutherland. *Handbook of Nonlinear Optics*. Marcel Dekker, Inc., 1996.

[7] Y.R. Shen. *The Principles of Nonlinear Optics*. John Wiley & Sons, 1984.

[8] J.A. Armstrong, N. Bloembergen, J. Ducuing, and P. S. Pershan. Interactions between light waves in a nonlinear dielectric. *Phys. Rev.*, 127:1918–1939, 1962.

[9] G.I. Stegeman, M. Sheik-Bahae, E. Van Stryland, and G. Assanto. Large nonlinear phase shifts in second-order nonlinear-optical processes. *Opt. Lett.*, 18(1):13–15, 1993.

[10] A.E. Kaplan. Eigenmodes of $\chi^{(2)}$ wave mixings: cross-induced second-order nonlinear refraction. *Opt. Lett.*, 18(15):1223–1225, 1993.

[11] K. Gallo, G. Assanto, K.R. Parameswaran, and M.M. Fejer. All-optical diode in a periodically poled lithium niobate waveguide. *Appl. Phys. Lett.*, 79(3):314–316, 2001.

[12] A.V. Buryak, P. Di Trapani, D.V. Skryabin, and S. Trillo. Optical solitons due to quadratic nonlinearitites: from basic physics to futuristic applications. *Phys. Reports*, 370:63–235, 2002.

[13] G. Porat and A. Arie. Efficient, broadband, and robust frequency conversion by fully nonlinear adiabatic three-wave mixing. *J. Opt. Soc. Am. B*, 30(5):1342–1351, 2013.

[14] R.W. Boyd. *Nonlinear Optics*. Academic Press, Inc., 1992.

[15] N. Bloembergen. *Nonlinear Optics*. W.A. Benjamin, Inc., 1965.

[16] S. Ashihara, J. Nishina, T. Shimura, K. Kuroda, T. Sugita, K. Mizuuchi, and K. Yamamoto. Nonlinear refraction of femtosecond pulses due to quadratic and cubic nonlinearities in periodically poled lithium tantalate. *Opt. Comm.*, 222:421–427, 2003.

[17] M. Sheik-Bahae, D.C. Hutchings, D.J. Hagan, and E.W. Van Stryland. Dispersion of bound electronic nonlinear refraction in solids. *IEEE J. Quant. Elect.*, 27(6):1296–1309, 1991.

[18] R. DeSalvo, A.A. Said, D.J. Hagan, E.W. Van Stryland, and M. Sheik-Bahae. Infrared to ultraviolet measurements of two-photon absorption and n_2 in wide bandgap solids. *IEEE J. Quant. Elect.*, 32(8):1324–1333, 1996.

[19] P. Gorski, M. Kin, and W. Kucharczyk. On the application of a generalized form of Miller's δ coefficient to nonlinear refractive indices in partially ionic crystals. *J. Phys. D: Appl. Phys.*, 30:1111–1114, 1997.

[20] A.A. Kaminskii, P. Becker, L. Bohaty, K. Ueda, K. Takaichi, J. Hanuza, M. Maczka, H.J. Eichler, and G.M.A. Gad. Monoclinic bismuth triborate BiB_3O_6 - a new efficient $\chi^{(2)} + \chi^{(3)}$ - nonlinear crystal: multiple stimulated Raman scattering and self-sum-frequency lasing effects. *Opt. Comm.*, 206:179–191, 2002.

[21] V. Pasiskevicius, A. Fragemann, F. Laurell, R. Butkus, V. Smilgevicius, and A. Piskarskas. Enhanced stimulated Raman scattering in optical parametric oscillators from periodically poled $KTiOPO_4$. *Appl. Phys. Lett.*, 82(3):325–327, 2003.

[22] T-H. My, O. Robin, O. Mhibik, C. Drag, and F. Bretenaker. Stimulated Raman scattering in an optical parametric oscillator based on periodically poled MgO-doped stoichiometric $LiTaO_3$. *Opt. Express*, 17(7):5912–5918, 2009.

[23] A.V. Okishev and J.D. Zuegel. Intracavity-pumped Raman laser action in a mid-IR, continuous-wave (cw) MgO:PPLN optical parametric oscillator. *Opt. Express*, 14(25):12169–12173, 2006.

[24] G. McConnell and A.I. Ferguson. Simultaneous stimulated Raman scattering and second harmonic generation in periodically poled lithium niobate. *Opt. Express*, 13(6):2099–2104, 2005.

[25] Z. Liu, Q. Wang, X. Zhang, Z. Liu, J. Chang, H. Wang, S. Zhang, S. Fan, W. Sun, G. Jin, X. Tao, S. Zhang, and H. Zhang. A $KTiOAsO_4$ Raman laser. *Appl. Phys. B*, 94:585–588, 2009.

[26] V. Pasiskevicius, C. Canalias, and F. Laurell. Highly efficient stimulated Raman scattering of picosecond pulses in $KTiOPO_4$. *Appl. Phys. Lett.*, 88:041110, 2006.

[27] H. Jang, G. Stromqvist, V. Pasiskevicius, and C. Canalias. Control of forward stimulated polariton scattering in periodically-poled KTP crystals. *Opt. Express*, 21(22):27277–27283, 2013.

[28] R. DeSalvo, D.J. Hagan, M. Sheik-Bahae, G. Stegeman, E.W. Van Stryland, and H. Vanherzeele. Self-focusing and self-defocusing by cascaded second-order effects in KTP. *Opt. Lett.*, 17(1):28–30, 1992.

[29] Ch. Bosshard, R. Spreiter, M. Zgonik, and P. Gunter. Kerr nonlinearity via cascaded optical rectification and the linear electro-optic effect. *Phys. Rev. Lett.*, 74(14):2816–2819, 1995.

[30] J.P. Torres, L. Torner, I. Biaggia, and M. Segev. Tunable self-action of light in optical rectification. *Opt. Comm.*, 213:351–356, 2002.

[31] M. Bass, P.A. Franken, J.F. Ward, and G. Weinreich. Optical rectification. *Phys. Rev. Lett.*, 9(11):446–448, 1962.

[32] T.K. Gustafson, J.-P.E. Taran, P.L. Kelley, and R.Y. Chiao. Self-modulation of picosecond pulses in electro-optic crystals. *Opt. Comm.*, 2(1):17–21, 1970.

[33] T. Suhara and M. Fujimura. *Waveguide Nonlinear-Optic Devices*. Springer-Verlag, 2003.

[34] A. Yariv and P. Yeh. *Optical waves in crystals*. John Wiley & Sons, 1984.

[35] A. Fiore, S. Janz, L. Delobel, P. van der Meer, P. Bravetti, V. Berger, E. Rosencher, and J. Nagle. Second-harmonic generation at $\lambda = 1.6\mu$m in AlGaAs/Al_2O_3 waveguides using birefringence phase matching. *Appl. Phys. Lett.*, 72(23):2942–2944, 1998.

[36] A. Fiore, V. Berger, E. Rosencher, P. Bravetti, and J. Nagle. Phase matching using an isotropic optical material. *Nature*, 391:463–466, 1998.

[37] M.V. Hobden. Phase-matched second-harmonic generation in biaxial crystals. *J. Appl. Phys.*, 38(11):4365–4372, 1967.

[38] K. Kato. Tunable UV generation to 0.185 μm in CsB_3O_5. *IEEE J. Quant. Elect.*, 31(1):169–171, 1995.

[39] V. Petrov, V. Badikov, G. Shevyrdyaeva, V. Panyutin, and V. Chizhikov. Phase-matching properties and optical parametric amplification in single crystals of $AgGaGeS_4$. *Opt. Mater.*, 26:217–222, 2004.

[40] R.T. Bailey, F.R. Cruickshank, D. Pugh, and J.N. Sherwood. Assessment of optically nonlinear organic crystals. *J. Phys. D: Appl. Phys.*, 26:B208–B216, 1993.

[41] C.E. Barker, D. Eimerl, and S.P. Velsko. Temperature-insensitive phase matching for second-harmonic generation in deuterated *l*-arginine phosphate. *J. Opt. Soc. Am. B*, 8(12):2481–2492, 1991.

[42] S.G. Grechin, V.G. Dmitriev, V.A. D'yakov, and V.I. Pryalkin. Temperature-noncritical third harmonic generation in an LBO crystal. *Quantum Electronics*, 34(6):565–568, 2004.

[43] V. Petrov, V. Vedenyapin, F. Noack, and F. Rotermund. Group-velocity matching through off-plane propagation in a biaxial nonlinear crystal. *Conf. on Lasers and Electro-optics*, pages 259–260, 2002.

[44] S. Takeuchi. Beamlike twin-photon generation by use of type II parametric downconversion. *Opt. Lett.*, 26(11):843–845, 2000.

[45] N. Boeuf, D. Branning, I. Chaperot, E. Dauler, S. Guerin, G. Jaeger, A. Muller, and A. Migdall. Calculating characteristics of noncollinear phase matching in uniaxial and biaxial crystals. *Opt. Eng.*, 39(4):1016–1024, 2000.

[46] G.T. Moore, C.A. Denman, and T.S. Ross. Using multiple mutually incoherent fiber lasers to pump a coherent signal beam in an optical parametric oscillator. *IEEE J. Quant. Elect.*, 36:828–834, 2000.

[47] R. Gadonas, A. Marcinkevicius, A. Piskarskas, V. Smilgevicius, and A. Stabinis. Travelling wave optical parametric generator pumped by a conical beam. *Opt. Comm.*, 146:253–256, 1998.

[48] N. Umemura, H. Nakao, H. Furuya, M. Yoshimura, Y. Mori, T. Sasaki, K. Yoshida, and K. Kato. 90° phase-matching properties of $YCa_4O(BO_3)_3$ and $Gd_xY_{1-x}Ca_4O(BO_3)_3$. *Jpn. J. Appl. Phys.*, 40:596–600, 2001.

[49] Z. Wang, X. Xu, K. Fu, R. Song, J. Wang, J. Wei, Y. Liu, and Z. Shao. Non-critical phase matching of $Gd_xY_{1-x}Ca_4O(BO_3)_3(Gd_xY_{1-x}COB)$ crystal. *Solid State Comm.*, 120:397–400, 2001.

[50] D. Artigas, E.U. Rafailov, P. Loza-Alvarez, and W. Sibbett. Periodically switched nonlinear structures for frequency conversion: theory and experimental demonstration. *IEEE J. Quant. Elect.*, 40(8):1122–1130, 2004.

[51] S.C. Chen and I.C. Khoo. Phase matching of second harmonic generations in rotational crystals. *Appl. Opt.*, 26(2):186–187, 1987.

[52] F. Jonsson and C. Flytzanis. Optical parametric generation and phase matching in magneto-optic media. *Opt. Lett.*, 24(21):1514–1516, 1999.

[53] X.G. Huang and M.R. Wang. A novel quasi-phase-matching frequency doubling technique. *Opt. Comm.*, 150:235–238, 1998.

[54] P. Dong and A.G. Kirk. Nonlinear frequency conversion in waveguide directional couplers. *Phys. Rev. Lett.*, 93(13):133901–1–4, 2004.

[55] I.P. Christov, H.C. Kapteyn, and M.M. Murnane. Quasi-phase matching of high-harmonics and attosecond pulses in modulated waveguides. *Opt. Express*, 7(11):362–367, 2000.

[56] X. Liu, L. Qian, and F. Wise. Effect of local phase-mismatch on frequency doubling of high-power femtosecond laser pulses under quasi-phase-matched conditions. *Opt. Comm.*, 164:69–75, 1999.

[57] K.C. Rustagi, S.C. Mehendale, and S. Meenakshi. Optical frequency conversion in quasi-phasematched stacks of nonlinear crystals. *IEEE J. Quant. Elect.*, 18(6):1029–1041, 1982.

[58] M.M. Fejer, G.A. Magel, D.H. Jundt, and R.L. Byer. Quasi-phase-matched second harmonic generation: tuning and tolerances. *IEEE J. Quant. Elect.*, 28(11):2631–2654, 1992.

[59] G. Imeshev, M.A. Arbore, M.M. Fejer, A. Galvanauskas, M. Fermann, and D. Harter. Ultrashort-pulse second-harmonic generation with longitudinally nonuniform quasi-phase-matching gratings: pulse compression and shaping. *J. Opt. Soc. Am. B*, 17(2):304–318, 2000.

[60] L. Gallmann, G. Steinmeyer, G. Imeshev, J.-P. Meyn, M.M. Fejer, and U. Keller. Sub-6-fs blue pulses generated by quasi-phase-matching second-harmonic generation pulse compression. *Appl. Phys. B*, 74(supplement 1):s237–s243, 2002.

[61] S.T. Yang and S.P. Velsko. Frequency-agile kilohertz repetition-rate optical parametric oscillator based on periodically poled lithium niobate. *Opt. Lett.*, 24(3):133–135, 1999.

[62] Y. Sasaki, A. Yuri, K. Kawase, and H. Ito. Terahertz-wave surface-emitted difference frequency generation in slant-stripe-type periodically poled $LiNbO_3$ crystal. *Appl. Phys. Lett.*, 81(18):3323–3325, 2002.

[63] P.E. Powers, T.J. Kulp, and S.E. Bisson. Continuous tuning of a continuous-wave periodically poled lithium niobate optical parametric oscillator by use of a fan-out grating design. *Opt. Lett.*, 23(3):159–161, 1998.

[64] N. O'Brien, M. Missey, P. Powers, V. Dominic, and K.L. Schepler. Electro-optic spectral tuning in a continuous-wave, asymmetric-duty-cycle, periodically poled $LiNbO_3$ optical parametric oscillator. *Opt. Lett.*, 24(23):1750–1752, 1999.

[65] N.E. Yu, S. Kurimura, and K. Kitamura. Broadband second harmonic generation with simultaneous group-velocity matching and quasi-phase matching. *Jpn. J. Appl. Phys.*, 42:L821–L823, 2003.

[66] S.M. Russell, P.E. Powers, M.J. Missey, and K.L. Schepler. Broadband mid-infrared generation with two-dimensional quasi-phase-matched structures. *IEEE J. Quant. Elect.*, 37(7):877–887, 2001.

[67] P. Xu, S.H. Ji, S.N. Zhu, X.Q. Yu, J. Sun, H.T. Wang, J.L. He, Y.Y. Zhu, and N.B. Ming. Conical second harmonic generation in a two-dimensional $\chi^{(2)}$ photonic crystal: a hexagonally poled $TiTaO_3$ crystal. *Phys. Rev. Lett.*, 93(133904):1–4, 2004.

[68] V. Berger. Nonlinear photonic crystal. *Phys. Rev. Lett.*, 81(19):4136–4139, 1998.

[69] J.R. Kurz, A.M. Schober, D.S. Hum, A.J. Saltzman, and M.M. Fejer. Nonlinear physical optics with transversely patterned quasi-phase-matching gratings. *IEEE J. Selected Topics Quant. Electron.*, 8(3):660–663, 2002.

[70] M.S. Piltch, C.D. Cantrell, and R.C. Sze. Infrared second harmonic generation in nonbirefringent cadmium telluride. *J. Appl. Phys.*, 47(8):3514–3517, 1976.

[71] L. Gordon, G.L. Woods, R.C. Eckardt, R.R. Route, R.S. Feigelson, M.M. Fejer, and R.L. Byer. Diffusion-bonded stacked GaAs for quasi-phase-matched second-harmonic generation of a carbon dioxide laser. *Electron. Lett.*, 29(22):1942–1944, 1993.

[72] L.A. Eyres, P.J. Tourreau, T.J. Pinguet, C.B. Ebert, J.S. Harris, M.M. Fejer, L. Becouarn, B. Gerard, and E. Lallier. All-epitaxial fabrication of thick, orientation-patterned GaAs films for nonlinear optical frequency conversion. *Appl. Phys. Lett.*, 79(7):904–906, 2001.

[73] P.S. Kuo, K.L. Vodopyanov, M.M. Fejer, X. Yu, J.S. Harris, D.F. Bliss, and D. Weyburne. GaAs optical parametric oscillator with circularly polarized and depolarized pump. *Opt. Lett.*, 32(18):2735–2737, 2007.

[74] S. Guha, J.O. Barnes, and P.G. Schunemann. Mid-wave infrared generation by difference frequency mixing of continuous wave lasers in orientation-patterned Gallium Phosphide. *Opt. Mater. Express*, 5(12):2911–2923, 2015.

[75] K.L. Vodopyanov, O. Levi, P.S. Kuo, T.J. Pinguet, J.S. Harris, M.M. Fejer, B. Gerard, L. Becouarn, and E. Lallier. Optical parametric oscillation in quasi-phase-matched GaAs. *Opt. Lett.*, 29(16):1912–1914, 2004.

[76] R. Haidar, N. Forget, P. Kupecek, and E. Rosencher. Fresnel phase matching for three-wave mixing in isotropic semiconductors. *J. Opt. Soc. Am. B*, 21(8):1522–1534, 2004.

[77] M. Raybaut, A. Godard, A. Toulouse, C. Lubin, and E. Rosencher. Nonlinear reflection effects on Fresnel phase matching. *Appl. Phys. Lett.*, 92:121112–1–3, 2008.

[78] H. Komine, W.H. Long, J.W. Tully Jr., and E.A. Stappaerts. Quasi-phase-matched second-harmonic generation by use of a total-internal-reflection phase shift in gallium arsenide and zinc selenide plates. *Opt. Lett.*, 23(9):661–663, 1998.

[79] A.V. Smith, D.J. Armstrong, and W.J. Alford. Increased acceptance bandwidths in optical frequency conversion by use of multiple walk-off-compensating nonlinear crystals. *J. Opt. Soc. Am. B*, 15(1):122–141, 1998.

[80] G.G. Luther, M.S. Alber, J.E. Marsden, and J.M. Robbins. Geometrical analysis of optical frequency conversion and its control in quadratically nonlinear media. *J. Opt. Soc. Am. B*, 17(6):932–941, 2000.

[81] J.D. Bierlein, D.B. Laubacher, J.B. Brown, and C.J. van der Poel. Balanced phase matching in segmented $KTiOPO_4$ waveguides. *Appl. Phys. Lett.*, 56(18):1725–1727, 1990.

[82] J.-J. Zondy, D. Kolker, C. Bonnin, and D. Lupinski. Second-harmonic generation with monolithic walk-off-compensating periodic structures. II. Experiments. *J. Opt. Soc. Am. B*, 20(8):1695–1707, 2003.

[83] X. Mu, H. Meissner, and H.-C. Lee. Optical parametric oscillations of 2 μm in multiple-layer bonded walk-off compensated KTP stacks. *Opt. Lett.*, 35(3):387–389, 2010.

[84] R.J. Gehr, M.W. Kimmel, and A.V. Smith. Simultaneous spatial and temporal walk-off compensation in frequency-doubling femtosecond pulses in $\beta - BaB_2O_4$. *Opt. Lett.*, 23(16):1298–1300, 1998.

[85] T. Sugita, K. Mizuuchi, K. Yamamoto, K. Fukuda, T. Kai, I. Nakayama, and K. Takahashi. Highly efficient second-harmonic generation in direct-bonded $MgO:LiNbO_3$ pure crystal waveguide. *Electron. Lett.*, 40(21):1359–1360, 2004.

[86] J.R. Kurz, X.P. Xie, and M.M. Fejer. Odd waveguide mode quasi-phase matching with angled and staggered gratings. *Opt. Lett.*, 27(16):1445–1447, 2002.

[87] S. Ducci, L. Lanco, V. Berger, A. De Rossi, V. Ortiz, and M. Calligaro. Continuous-wave second-harmonic generation in modal phase matched semiconductor waveguides. *Appl. Phys. Lett.*, 84(16):2974–2976, 2004.

[88] W. Wirges, S. Yilmaz, W. Brinker, S. Bauer-Gogonea, S. Bauer, M. Jager, G.I. Stegeman, M. Ahlheim, M. Stahelin, B. Zysset, F. Lehr, M. Diemeer, and M.C. Flipse. Polymer waveguides with optimized overlap integral for modal dispersion phase-matching. *Appl. Phys. Lett.*, 70(25):3347–3349, 1997.

[89] K. Chikuma, S. Okamoto, N. Uenishi, T. Uemiya, and S. Umegaki. Design, fabrication, and evaluation of crystal-cored fibers for efficient second-harmonic generation based on Cerenkov-radiation-type phase matching. *Appl. Opt.*, 43(24):4697–4704, 2004.

[90] G. Landry and T.A. Maldonado. Counterpropagating quasi-phase matching: a generalized analysis. *J. Opt. Soc. Am. B*, 21(8):1509–1521, 2004.

[91] M.J. Steel and C.M. de Sterke. Second-harmonic generation in second-harmonic gratings. *Appl. Opt.*, 35(18):3211–3222, 1996.

[92] C. DeAngelis, G. Nalesso, D. Modotto, M. Midrio, A. Locatelli, and J.S. Aitchison. Multiple-scale coupled-mode theory for second-harmonic generation in one-dimensional periodic structures. *J. Opt. Soc. Am. B*, 20(9):1853–1865, 2003.

[93] M. Scalora, M.J. Bloemer, A.S. Manka, J.P. Dowling, C.M. Bowden, R. Viswanathan, and J.W. Haus. Pulsed second-harmonic generation in nonlinear, one-dimensional, periodic structures. *Phys. Rev. A*, 56(4):3166–3174, 1997.

[94] N. Bloembergen and A.J. Sievers. Nonlinear optical properties of periodic laminar structures. *Appl. Phys. Lett.*, 17(11):483–486, 1970.

[95] C.L. Tang and P.P. Bey. Phase matching in second-harmonic generation using artificial periodic structured. *IEEE J. Quant. Elect.*, 9(1):9–17, 1973.

[96] A. Bosco, M. Centini, L. Sciscione, C. Sibilia, E. Fazio, M. Bertolotti, A. Fiore, A. Convertino, L. Cerri, and M. Scalora. Noncollinear type-II second-harmonic generation in a $Al_{0.3}Ga_{0.7}As/Al_2O_3$ one-dimensional photonic crystal. *Appl. Phys. Lett.*, 84(16):3010–3012, 2004.

[97] Y. Dumeige, I. Sagnes, P. Monnier, P. Vidakovic, I. Abram, C. Meriadec, and A. Levenson. Phase-matched frequency doubling at photonic band edges: efficiency scaling as the fifth power of the length. *Phys. Rev. Lett.*, 89(043901), 2002.

[98] J.P. van der Ziel and M. Ilegems. Optical second harmonic generation in periodic multilayer GaAs-$Al_{0.3}Ga_{0.7}As$ structures. *Appl. Phys. Lett.*, 28(8):437–439, 1976.

[99] J. Trull, R. Vilaseca, J. Martorell, and R. Corbalan. Second-harmonic generation in local modes of a truncated periodic structure. *Opt. Lett.*, 20(17):1746–1748, 1995.

[100] T. Pertsch, U. Peschel, and F. Lederer. All-optical switching in quadratically nonlinear waveguide arrays. *Opt. Lett.*, 28(2):102–104, 2003.

[101] D.W. Prather, S. Shi, D.M. Pustai, C. Chen, S. Venkataraman, A. Sharkawy, G.J. Schneider, and J. Murakowski. Dispersion-based optical routing in photonic crystals. *Opt. Lett.*, 29(1):50–52, 2004.

[102] M. Notomi. Negative refraction in photonic crystals. *Opt. Quant. Electron.*, 34:133–143, 2002.

[103] M. Trippenbach and Y.B. Band. Propagation of light pulses in non-isotropic media. *J. Opt. Soc. Am. B*, 13(7):1403–1411, 1996.

[104] D. Eimerl, J.M. Auerbach, and P.W. Milonni. Paraxial wave theory of second and third harmonic generation in uniaxial crystals, I. Narrowband pump fields. *J. Mod. Opt.*, 42(5):1037–1067, 1995.

[105] M.A. Dreger. Optical beam propagation in biaxial crystals. *J. Opt. A: Pure Appl. Opt.*, 1:601–616, 1999.

[106] M.A. Dreger and J.K. McIver. Second-harmonic generation in a nonlinear, anisotropic medium with diffraction and depletion. *J. Opt. Soc. Am. B*, 7(5):776–784, 1990.

[107] Jr. J.A. Fleck and M.D. Feit. Beam propagation in uniaxial anisotropic media. *J. Opt. Soc. Am.*, 73(7):920–926, 1983.

[108] M.A. Porras. Pulse correction to monochromatic light-beam propagation. *Opt. Lett.*, 26(1):44–46, 2001.

[109] P. Kinsler and G.H.C. New. Few-cycle pulse propagation. *Phys. Rev. A*, 67:023813–1–8, 2003.

[110] T. Brabec and F. Krausz. Nonlinear optical pulse propagation in the single-cycle regime. *Phys. Rev. Lett.*, 78(17):3282–3285, 1997.

[111] A. Bourgeade and E. Freysz. Computational modeling of second-harmonic generation by solution of full-wave vector Maxwell equations. *J. Opt. Soc. Am. B*, 17(2):226–234, 2000.

[112] J.C. Diels and W. Rudolph. *Ultrashort Laser Pulse Phenomena.* Academic Press, 1996.

[113] G.P. Agrawal. *Nonlinear Fiber Optics.* Academic Press, 1989.

[114] J.R. de Oliveira, M.A. de Moura, J.M. Hickmann, and A.S.L. Gomes. Self-steepening of optical pulses in dispersive media. *J. Opt. Soc. Am. B*, 9(11):2025–2027, 1992.

[115] D. Hovhannisyan, K. Stepanyan, and R. Avagyan. Sum and difference frequency generation by femtosecond laser pulses in a nonlinear crystal. *Opt. Comm.*, 245:443–456, 2005.

[116] R.C. Miller. Optical second harmonic generation in piezoelectric crystals. *Appl. Phys. Lett.*, 5(1):17–19, 1964.

[117] M. Schubert and B. Wilhelmi. *Nonlinear Optics and Quantum Electronics*. John Wiley & Sons, 1986.

[118] S. Nakamura, T. Saeki, and Y. Koyamada. Observation of slowly varying envelope approximation breakdown by comparison between the extended finite-difference time-domain method and the beam propagation method for ultrashort-laser-pulse propagation in a silica fiber. *Jpn. J. Appl. Phys.*, 43(10):7015–7025, 2004.

[119] P.E. Powers. *Fundamentals of nonlinear optics*. CRC Press, 2011.

[120] G. New. *Introduction to nonlinear optics*. Cambridge University Press, 2011.

[121] V.G. Dmitriev, G.G. Gurzadyan, and D.N. Nikogosyan. *Handbook of Nonlinear Optical Crystals*. Springer, third edition, 1999.

[122] W. Koechner. *Solid-state laser engineering*. Springer, 2006.

[123] G.D. Boyd and D.A. Kleinman. Parametric interactions of focused gaussian light beams. *J. Appl. Phys.*, 39(8):3597–3638, 1968.

[124] S.A. Akhmanov, A.S. Chirkin, K.N. Drabovich, A.I. Kovrigin, R.V. Khokhlov, and A.P. Sukhorukov. Nonstationary nonlinear optical effects and ultrashort light pulse formation. *IEEE J. Quant. Elect.*, QE-4(10):598–605, 1968.

[125] H. Wang and A.M. Weiner. Efficiency of short-pulse type-I second-harmonic generation with simultaneous spatial walk-off, temporal walk-off, and pump depletion. *IEEE J. Quant. Elect.*, 39(12):1600–1618, 2003.

[126] E.C. Cheung and J.M. Liu. Theory of a synchronously pumped optical paramteric oscillator in steady-state operation. *J. Opt. Soc. Am. B*, 7(8):1385–1401, 1990.

[127] K.D. Shaw. Spatio-temporal evolution of the intra-cavity fields in a pulsed doubly resonant optical parametric oscillator. *Opt. Comm.*, 144:134–160, 1997.

[128] T. Debuisschert. Nanosecond optical parametric oscillators. *Quant. Semiclass. Opt.*, 9:209–219, 1997.

[129] M.D. Feit and J.A. Fleck Jr. Beam nonparaxiality, filament formation, and beam breakup in the self-focusing of optical beams. *J. Opt. Soc. Am. B*, 5(3):633–640, 1988.

[130] M. Lax, J.H. Batteh, and G.P. Agrawal. Channeling of intense electromagnetic beams. *J. Appl. Phys.*, 52(1):109–125, 1981.

[131] P. Pliszka and P.P. Banerjee. Nonlinear transverse effects in second-harmonic generation. *J. Opt. Soc. Am. B*, 10(10), 1993.

[132] G. Arisholm. General numerical methods for simulating second-order nonlinear interactions in birefringent media. *J. Opt. Soc. Am. B*, 14(10):2543–2549, 1997.

[133] A.V. Smith and M.S. Bowers. Phase distortions in sum- and difference-frequency mixing in crystals. *J. Opt. Soc. Am. B*, 12(1):49–57, 1995.

[134] S.-C. Sheng and A.E. Siegman. Nonlinear-optical calculations using fast-transform methods: Second-harmonic generation with depletion and diffraction. *Phys. Rev. A*, 21(2):599–606, 1980.

[135] D. Yevick and B. Hermansson. Efficient beam propagation techniques. *IEEE J. Quant. Elect.*, 26:109–112, 1990.

[136] H.J. Bakker, P.C.M. Planken, and H.G. Muller. Numerical calculation of optical frequency-conversion processes: a new approach. *J. Opt. Soc. Am. B*, 6(9):1665–1672, 1989.

[137] H.J. Bakker, P.C.M. Planken, L. Kuipers, and A. Lagendijk. Phase modulation in second-order nonlinear-optical processes. *Phys. Rev. A*, 42(7):4085–4101, 1990.

[138] T. Nishikawa and N. Uesugi. Effects of walk-off ang group velocity difference on the optical parametric generation in $KTiOPO_4$ crystals. *J. Appl. Phys.*, 77(10):4941–4947, 1995.

[139] U.K. Sapaev, J. Kutzner, and K. Finsterbusch. Optimization of type-II frequency doubling of spatial and temporal limited laser light in nonlinear crystals. *Opt. Quant. Electron.*, 37:515–527, 2005.

[140] L.L. Bravo-Roger, K.Z. Nobrega, H.E. Hernandex-Figueroa, and A.P. Lopez-Barbero. Spatio-temporal finite-element propagator for ultrashort optical pulses. *IEEE Photonics Tech. Lett.*, 16(1):132–134, 2004.

[141] W.H. Press, S.A. Teukolsky, W.T. Vetterling, and B.P. Glannery. *Numerical recipes in C.* Cambridge Univ. Press, 1995.

[142] A. Bertolani, A. Cucinotta, S. Selleri, L. Vincetti, and M. Zololi. Overview on finite-element time-domain approaches for optical propagation analysis. *Opt. Quant. Electron.*, 35:1005–1023, 2003.

[143] P.W. Milonni. *The Quantum Vacuum*. Academic Press, 1994.

[144] G. Arisholm. Quantum noise initiation and macroscopic fluctuations in optical parametric oscillators. *J. Opt. Soc. Am. B*, 16(1):117–127, 1999.

[145] P. Baum, S. Lochbrunner, and E. Riedle. Tunable sub-10-fs ultraviolet pulses generated by achromatic frequency doubling. *Opt. Lett.*, 29(14):1686–1688, 2004.

[146] R. Buffa. Transient second-harmonic generation with spatially nonuniform nonlinear coefficients. *Opt. Lett.*, 27(12):1058–1060, 2002.

[147] U.K. Sapaev and D.T. Reid. General second-harmonic pulse shaping in grating-engineered quasi-phase-matched nonlinear crystals. *Opt. Express*, 13(9):3264–3276, 2005.

[148] A. Umbrasas, J.-C. Diels, J. Jacob, G. Valiulis, and A. Piskarskas. Generation of femtosecond pulses through second-harmonic compression of the output of a Nd:YAG laser. *Opt. Lett.*, 20(21):2228–2230, 1995.

[149] A. Dubietis, G. Valiulis, G. Tamosauskas, R. Danielius, and A. Piskarskas. Nonlinear second-harmonic pulse compression with tilted pulses. *Opt. Lett.*, 22(14):1071–1073, 1997.

[150] A. Umbrasas, J.-C. Diels, J. Jacob, and A. Piskarskas. Parametric oscillation and compression in KTP crystals. *Opt. Lett.*, 19(21):1753–1755, 1994.

[151] H. Wang and A.M. Weiner. A femtosecond waveform transfer technique using type II second harmonic generation. *IEEE J. Quant. Elect.*, 40:937–945, 2004.

[152] R. Trebino. *Frequency-resolved optical gating: the measurement of ultrashort laser pulses*. Kluwer Academic Publishers, 2000.

[153] W. Wasilewski, P. Wasylczyk, and C. Radzewicz. Femtosecond laser pulses measured with a photodiode - FROG revisited. *Appl. Phys. B*, 78, 2004.

[154] C. Iaconis and I.A. Walmsley. Spectral phase interferometry for direct electric-field reconstruction of ultrashort optical pulses. *Opt. Lett.*, 23(10):792–794, 1998.

[155] D.L. Mills. *Nonlinear Optics*. Springer, 1991.

[156] F. Zernike and J.E. Midwinter. *Applied Nonlinear Optics*. John Wiley & Sons, 1973.

[157] D.R. White, E.L. Dawes, and J.H. Marburger. Theory of second-harmonic generation with high-conversion efficiency. *IEEE J. Quant. Elect.*, QE-6:793–796, 1970.

[158] G. Arisholm, R. Paschotta, and T. Sudmeyer. Limits to the power scalability of high-gain optical parametric amplifiers. *J. Opt. Soc. Am. B*, 21(3):578–590, 2004.

[159] D.J. Armstrong, W.J. Alford, T.D. Raymond, A.V. Smith, and M.S. Bowers. Parametric amplification and oscillation with walkoff-compensating crystals. *J. Opt. Soc. Am. B*, 14(2):460–474, 1997.

[160] V. Magni. Optimum beam for second harmonic generation. *Opt. Comm.*, 176:245–251, 2000.

[161] J.-J. Zondy. Comparative theory of walkoff-limited type-II versus type-I second harmonic generation with guassian beams. *Opt. Comm.*, 81(6):427–440, 1991.

[162] G.D. Boyd and A. Ashkin. Theory of parametric oscillator threshold with single-mode optical masers and observation of amplification in $LiNbO_3$. *Phys. Rev.*, 146(1):187–198, 1966.

[163] S. Guha, F.-J. Wu, and J. Falk. The effects of focusing on parametric oscillation. *IEEE J. Quant. Elect.*, QE-18(5):907–912, 1982.

[164] J.-J. Zondy. The effects of focusing in type-I and type-II difference-frequency generations. *Opt. Comm.*, 149:181–206, 1998.

[165] A.E. Siegman. *Lasers*. University Science Books, 1986.

[166] J.-J. Zondy, D. Touahri, and O. Acef. Absolute value of the d_{36} nonlinear coefficient of $AgGaS_2$: prospect for a low-threshold doubly resonant oscillator-based 3:1 frequency divider. *J. Opt. Soc. Am. B*, 14(10):2481–2497, 1997.

[167] S. Guha and J. Falk. The effects of focusing in the three-frequency parametric upconverter. *J. Appl. Phys.*, 51(1):50–60, 1980.

[168] T. Freegarde, J. Coutts, J. Walz, D. Leibfried, and T.W. Hansch. General analysis of type I second-harmonic generation with elliptical Gaussian beams. *J. Opt. Soc. Am. B*, 14(8):2010–2016, 1997.

[169] A. Steinbach, M. Rauner, F.C. Cruz, and J.C. Bergquist. CW second harmonic generation with elliptical Gaussian beams. *Opt. Comm.*, 123:207–214, 1996.

[170] F.M. Librecht and J.A. Simons. Second-harmonic generation in birefringent crystals by a Gaussian beam with an elliptical cross section. *IEEE J. Quant. Elect.*, QE-11:850–852, 1975.

[171] M.V. Pack, D.J. Armstrong, A.V. Smith, and M.E. Amiet. Second harmonic generation with focused beams in a pair of walkoff-compensating crystals. *Opt. Comm.*, 221:211–221, 2004.

[172] J. Friebe, K. Moldenhauer, E.M. Rasel, W. Ertmer, L. Isaenko, A. Yelisseyev, and J.-J. Zondy. β-BaB_2O_4 deep UV monolithic walk-off compensating tandem. *Opt. Comm.*, 261:300–309, 2006.

[173] H.E. Major, C.B.E. Gawith, and P.G.R. Smith. Gouy phase compensation in quasi-phase matching. *Opt. Comm.*, 281:5036–5040, 2008.

[174] J.R. Fienup. Phase retrieval algorithms: a comparison. *Appl. Opt.*, 21(15):2758–2769, 1982.

[175] A.R. Pandey, J.W. Haus, P.E. Powers, and P.P. Yaney. Optical field measurements for accurate modeling of nonlinear parametric interactions. *J. Opt. Soc. Am. B*, 26(2):218–227, 2009.

[176] C. Yan and J.-C. Diels. Imaging with femtosecond pulses. *Appl. Opt.*, 31(32):6869–6873, 1992.

[177] G.W. Faris and M. Banks. Upconverting time gate for imaging through highly scattering media. *Opt. Lett.*, 19(22):1813–1815, 1994.

[178] J. Watson, P. Georges, T. Lepine, B. Alonzi, and A. Brun. Imaging in diffuse media with ultrafast degenerate optical parametric amplification. *Opt. Lett.*, 20(3):231–233, 1995.

[179] F. Devaux, E. Guiot, and E. Lantz. Image restoration through aberrant media by optical phase conjugation in a type II three-wave mixing interaction. *Opt. Lett.*, 23(20):1597–1599, 1998.

[180] L. Lefort and A. Barthelemy. Revisiting optical phase conjugation by difference-frequency generation. *Opt. Lett.*, 21(12):848–850, 1996.

[181] M. Bondani, A. Allevi, and A. Andreoni. Holography by nondegenerate $\chi^{(2)}$ interactions. *J. Opt. Soc. Am. B*, 20(1):1–13, 2003.

[182] V.N. Mikhailov, M. Bondani, F. Paleari, and A. Andreoni. Optical phase conjugation in difference-frequency generation. *J. Opt. Soc. Am. B*, 20(8):1715–1723, 2003.

[183] M. Bondani, A. Allevi, A. Brega, E. Puddu, and A. Andreoni. Difference-frequency-generated holograms of two-dimensional objects. *J. Opt. Soc. Am. B*, 21(2):280–288, 2004.

[184] B.Ya. Zel'dovich, N.F. Pilipetsky, and V.V. Shkunov. *Principles of phase conjugation*. Springer-Verlag, 1985.

[185] S. Brustlein, E. Lantz, and F. Devaux. Absolute radiance imaging using parametric image amplification. *Opt. Lett.*, 32(10):1278–1280, 2007.

[186] S.-K. Choi, M. Vasilyev, and P. Kumar. Noiseless optical amplification of images. *Phys. Rev. Lett.*, 83(10):1938–1941, 1999.

[187] O. Aytur and P. Kumar. Pulsed twin beams of light. *Phys. Rev. Lett.*, 65(13):1551–1554, 1990.

[188] M.L. Marable, S.-K. Choi, and P. Kumar. Measurement of quantum-noise correlations in parametric image amplification. *Opt. Express*, 2(3):84–92, 1998.

[189] T.B. Pittman, Y.H. Shih, D.V. Strekalov, and A.V. Sergienko. Optical imaging by means of two-photon quantum entanglement. *Phys. Rev. A*, 52(5):R3429–R3432, 1995.

[190] E. Puddu, A. Andreoni, I.P. Degiovanni, M. Bondani, and S. Castelletto. Ghost imaging with intense fields from chaotically seeded parametric downconversion. *Opt. Lett.*, 32(9):1132–1134, 2007.

[191] R. Dorn, S. Quabis, and G. Leuchs. Sharper focus for a radially polarized light beam. *Phys. Rev. Lett.*, 91(23):233901–1–4, 2003.

[192] G. Chang, C.J. Divin, C.-H. Liu, S.L. Williamson, A. Galvanauskas, and T.B. Norris. Generation of radially polarized terahertz pulses via velocity-mismatched optical rectification. *Opt. Lett.*, 32(4):433–435, 2007.

[193] A.E. Siegman. Defining the effective radius of curvature for a nonideal optical beam. *IEEE J. Quant. Elect.*, 27(5):1146–1148, 1991.

[194] A.V. Smith, W.J. Alford, T.D. Raymond, and M.S. Bowers. Comparison of a numerical model with measured performance of a seeded, nanosecond KTP optical parametric oscillator. *J. Opt. Soc. Am. B*, 12(11):2253–2267, 1995.

[195] B.A. Richman, S.E. Bisson, R. Trebino, E. Sidick, and A. Jacobson. Efficient broadband second-harmonic generation by dispersive achromatic nonlinear conversion using only prisms. *Opt. Lett.*, 23(7):497–499, 1998.

[196] T. Yanagawa, H. Kanbara, O. Tadanaga, M. Asobe, H. Suzuki, and J. Yumoto. Broadband difference frequency generation around phase-match singularity. *Appl. Phys. Lett.*, 86:161106–1–3, 2005.

[197] A.V. Smith. Group-velocity-matched three-wave mixing in birefringent crystals. *Opt. Lett.*, 26(10):719–721, 2001.

[198] S. Ashihara, T. Shimura, and K. Kuroda. Group-velocity matched second-harmonic generation in tilted quasi-phase-matched gratings. *J. Opt. Soc. Am. B*, 20(5):853–856, 2002.

[199] A.M. Schober, M. Charbonneau-Lefort, and M.M. Fejer. Broadband quasi-phase-matched second-harmonic generation of ultrashort optical pulses with spectral angular dispersion. *J. Opt. Soc. Am. B*, 22(8):1699–1713, 2005.

[200] Y. Furukawa, H. Sakata, and T. Yagi. Sum-frequency generation in periodically poled $KTiOPO_4$ with large tolerances of temperature and wavelength. *Jpn. J. Appl. Phys.*, 43(8B):5867–5870, 2004.

[201] M.A. Arbore, O. Marco, and M.M. Fejer. Pulse compression during second-harmonic generation in aperiodic quasi-phase-matching gratings. *Opt. Lett.*, 22(12):865–867, 1997.

[202] J. Huang, J.R. Kurz, C. Langrock, A.M. Schober, and M.M. Fejer. Quasi-group-velocity matching using integrated-optic structures. *Opt. Lett.*, 29(21):2482–2484, 2004.

[203] X. Liu, R. Trebino, and A. V. Smith. Numerical simulations of ultrasimple ultrashortlaser-pulse measurement. *Opt. Express*, 15(8):4585–4596, 2007.

[204] Y. Takagi, Y. Yamada, K. Ishikawa, S. Shimizu, and S. Sakabe. Ultrafast single-shot optical oscilloscope based on time-to-space conversion due to temporal and spatial walk-off effects in nonlinear mixing crystals. *Jpn. J. Appl. Phys.*, 44(9A):6546–6549, 2005.

[205] T. Traub, F. Ruebel, and J.A. L'huillier. Efficient injection-seeded kHz picosecond LBO optical parametric generator. *Appl. Phys. B*, 28:25–29, 2010.

[206] A. Cavanna, F. Just, P.R. Sharapova, M. Taheri, G. Leuchs, and M.V. Chekhova. Tunable optical parametric generator based on the pump spatial walk-off. *Opt. Lett.*, 41(3):646–649, 2016.

[207] R. Danielius, A. Piskarskas, A. Stabinis, G.P. Banfi, P. Di Trapani, and R. Righini. Traveling-wave parametric generation of widely tunable, highly coherent femtosecond light pulses. *J. Opt. Soc. Am. B*, 10(11):2222–2232, 1993.

[208] P.S. Hsu, S. Roy, and J.R. Gord. Development of a nearly transform-limited, low-repetition-rate, picosecond optical parametric generator. *Opt. Comm.*, 281:6068–6071, 2008.

[209] S.M. Lee, B.K. Rhee, M. Choi, and S.-H. Park. Optical parametric spectral broadening of picosecond laser pulses in β-barium borate. *Appl. Phys. Lett.*, 83(9):1722–1724, 2003.

[210] X. Xie, A.M. Schober, C. Langrock, R.V. Roussev, J.R. Kurz, and M.M. Fejer. Picojoule threshold, picosecond optical parametric generation in reverse proton-exchanged lithium niobate waveguides. *J. Opt. Soc. Am. B*, 21(7):1397–1402, 2004.

[211] X. Xie and M.M. Fejer. Cascaded optical parametric generation in reverse-proton-exchange lithium niobate waveguides. *J. Opt. Soc. Am. B*, 24(3):585–591, 2007.

[212] M. Marangoni, M. Lobino, and R. Ramponi. Optical parametric generation of nearly transform-limited mid-infrared pulses in dispersion-engineered nonlinear waveguides. *Opt. Lett.*, 33(18):2107–2109, 2008.

[213] B. Bareika, A. Birmontas, G. Dikchyus, A. Piskarskas, V. Sirutkaitis, and A. Stabinis. Parametric generation of picosecond continuum in near-infrared and visible ranges on the basis of a quadratic nonlinearity. *Sov. J. Quantum Electron.*, 12(12):1654–1655, 1982.

[214] M. Levenius, M. Conforti, F. Baronio, V. Pasiskevicius, F. Laurell, C. De Angelis, and K. Gallo. Multistep quadratic cascading in broadband optical parametric generation. *Opt. Lett.*, 37(10):1727–1729, 2012.

[215] P.S. Kuo, K.L. Vodopyanov, M.M. Fejer, D.M. Simanovskii, X. Yu, J.S. Harris, D. Bliss, and D. Weyburne. Optical parametric generation of a mid-infrared continuum in orientation-patterned GaAs. *Opt. Lett.*, 31(1):71–73, 2006.

[216] H.-H. Lim, O. Prakash, B.-J. Kim, K. Pandiyan, M. Cha, and B.K. Rhee. Ultra-broadband optical parametric generation and simultaneous RGB generation in periodically poled lithium niobate. *Opt. Express*, 15(26):18294–18299, 2007.

[217] P.E. Britton, N.G.R. Broderick, D.J. Richardson, P.G.R. Smith, G.W. Ross, and D.C. Hanna. Wavelength-tunable high-power picosecond pulses from a fiber-pumped diode-seeded high-gain parametric amplifier. *Opt. Lett.*, 23(20):1588–1590, 1998.

[218] S.C. Kumar, P.G. Schunemann, K.T. Zawilski, and M. Ebrahim-Zadeh. Advances in ultrafast optical parametric sources for the mid-infrared based on $CdSiP_2$. *J. Opt. Soc. Am. B*, 33(11):D44–D56, 2016.

[219] H. Xu, F. Yang, Y. Chen, K. Liu, S. Du, N. Zong, J. Yang, Y. Bo, Q. Peng, J. Zhang, D. Cui, and Z. Xu. Millijoule-level picosecond mid-infrared optical parametric amplifier based on MgO-doped periodically poled lithium niobate. *Appl. Opt.*, 54(9):2489–2494, 2015.

[220] U. Bader, T. Mattern, T. Bauer, J. Bartschke, M. Rahm, A. Borsutzky, and R. Wallenstein. Pulsed nanosecond optical parametric generator based on periodically poled lithium niobate. *Opt. Comm.*, 217:375–380, 2003.

[221] J.-P. Feve, B. Boulanger, B. Menaert, and O. Pacaud. Continuous tuning of a microlaser-pumped optical parametric generator by use of a cylindrical periodically poled lithium niobate crystal. *Opt. Lett.*, 28(12):1028–1030, 2003.

[222] S. Lambert-Girard, M. Allard, M. Piche, and F. Babin. Broadband and tunable optical parametric generator for remote detection of gas molecules in the short and mid-infrared. *Appl. Opt.*, 54(10):2594–2605, 2015.

[223] M. Missey, V. Dominic, P. Powers, and K.L. Schepler. Aperture scaling effects with monolithic periodically poled lithium niobate optical parametric oscillators and generators. *Opt. Lett.*, 25(4):248–250, 2000.

[224] L. Xu, H.-Y. Chan, S. Alam, D.J. Richardson, and D.P. Shepherd. High-energy, near- and mid-IR picosecond pulses generated by a fiber-MOPA-pumped optical parametric generator and amplifier. *Opt. Express*, 23(10):12613–12618, 2015.

[225] S.V. Marchese, E. Innerhofer, R. Paschotta, S. Kurimura, K. Kitamura, G. Arisholm, and U. Keller. Room temperature femtosecond optical parametric generation in MgO-doped stoichiometric $LiTaO_3$. *Appl. Phys. B*, 81:1049–1052, 2005.

[226] G. Arisholm. General analysis of group velocity effects in collinear optical parametric amplifiers and generators. *Opt. Express*, 15(10):6513–6527, 2007.

[227] Y.-C. Chiu, Y.-C. Huang, and C.-H. Chen. Parametric laser pulse shortening. *Opt. Lett.*, 39(16):4792–4795, 2014.

[228] U. Bader, J.-P. Meyn, J. Bartschke, T. Weber, A. Borsutzky, R. Wallenstein, R.G. Batchko, M.M. Fejer, and R.L. Byer. Nanosecond periodically poled lithium niobate optical parametric generator pumped at 532 nm by a single-frequency passively Q-switched Nd:YAG laser. *Opt. Lett.*, 24(22):1608–1610, 1999.

[229] M.D. Cocuzzi, K.L. Schepler, and P.E. Powers. Narrow-bandwidth, subnanosecond, infrared pulse generation in PPLN pumped by a fiber amplifier-microchip oscillator. *IEEE J. Quant. Elect.*, 15(2):372–376, 2009.

[230] H. Linnenbank, T. Steinle, and H. Giessen. Narrowband cw injection seeded high power femtosecond double-pass optical parametric generator at 43 MHz: gain and noise dynamics. *Opt. Express*, 24(17):19558–19566, 2016.

[231] H. Linnenbank and S. Linden. High repetition rate femtosecond double pass optical parametric generator with more than 2 W tunable output in the NIR. *Opt. Express*, 22(15):18072–18077, 2014.

[232] M. Rahm, U. Bader, G. Anstett, J.-P. Meyn, R. Wallenstein, and A. Borsutzky. Pulse-to-pulse wavelength tuning of an injection seeded nanosecond optical parametric generator with 10 kHz repetition rate. *Appl. Phys. B*, 75:47–51, 2002.

[233] P.E. Powers, P.K. Bojja, R. Alkuwari, E. Vershure, and K.L. Schepler. High-energy seeded optical parametric generation with elliptical beams is quasi-phase-matched crystals. *J. Opt. Soc. Am. B*, 22(10):2169–2177, 2005.

[234] T.H. Jeys. Multipass optical parametric amplifier. *Opt. Lett.*, 21(16):1229–1231, 1996.

[235] K.W. Aniolek, P.E. Powers, T.J. Kulp, B.A. Richman, and S.E. Bisson. Cavity ringdown laser absorption spectroscopy with a 1 kHz mid-infrared periodically poled lithium niobate optical parametric generator/optical parametric amplifier. *Chem. Phys. Lett.*, 302:555–562, 1999.

[236] M. Marangoni, R. Osellame, R. Ramponi, G. Cerullo, A. Steinmann, and U. Morgner. Near-infrared optical parametric amplifier at 1 MHz directly pumped by a femtosecond oscillator. *Opt. Lett.*, 32(11):1489–1491, 2007.

[237] P.E. Powers, K.W. Aniolek, T.J. Kulp, B.A. Richman, and S.E. Bisson. Periodically poled lithium niobate optical parametric amplifier seeded with the narrow-band filtered output of an optical parametric generator. *Opt. Lett.*, 23(24):1886–1888, 1998.

[238] S. Alisauskas, R. Butkus, A. Piskarskas, K. Regelskis, and V. Smilgevicius. Modulation of spatial spectrum in tunable two crystal optical parametric generation. *Opt. Comm.*, 280:463–467, 2007.

[239] K. Druhl. Dispersion-induced generation of higher order transversal modes in singly-resonant optical parametric oscillators. *Opt. Comm.*, 145:5–8, 1998.

[240] K. Druhl. Diffractive effects in singly resonant continuous-wave parametric oscillators. *Appl. Phys. B*, 66:677–683, 1998.

[241] S. Guha. Focusing dependence of the efficiency of a singly resonant optical parametric oscillator. *Appl. Phys. B*, 66:663–675, 1998.

[242] S. Schiller, K. Schneider, and J. Mlynek. Theory of an optical parametric oscillator with resonant pump and signal. *J. Opt. Soc. Am. B*, 16(9):1512–1524, 1999.

[243] R. Paschotta, P. Kurz, R. Henking, S. Schiller, and J. Mlynek. 82% efficient continuous-wave frequency doubling of 1.06 μm with a monolithic MgO:$LiNbO_3$ resonator. *Opt. Lett.*, 19(17):1325–1327, 1994.

[244] G.T. Moore. Resonant sum-frequency generation. *IEEE J. Quant. Elect.*, 38(1):12–18, 2002.

[245] S. Schiller, R. Bruckmeier, and A.G. White. Classical and quantum properties of the subharmonic-pumped parametric oscillator. *OC*, 138:158–171, 1997.

[246] S. Schiller, G. Breitenbach, R. Paschotta, and J. Mlynek. Subharmonic-pumped continuous-wave parametric oscillator. *Appl. Phys. Lett.*, 68(24):3374–3376, 1996.

[247] C.A. Denman, P.D. Hillman, G.T. Moore, J.M. Telle, J.E. Preston, J.D. Drummond, and R.Q. Fugate. Realization of a 50-watt facility-class sodium guidestar pump laser. *Proceedings of SPIE*, 5705:46–49, 2005.

[248] S. Schiller and R.L. Byer. Quadruply resonant optical parametric oscillation in a monolithic total-internal-reflection resonator. *J. Opt. Soc. Am. B*, 10(9):1696–1707, 1993.

[249] C. Zimmermann, R. Kallenbach, T.W. Hansch, and J. Sandberg. Doubly-resonant second-harmonic generation in β-barium-borate. *Opt. Comm.*, 71(3,4):229–234, 1989.

[250] L. Longchambon, N. Treps, T. Coudreau, J. Laurat, and C. Fabre. Experimental evidence of spontaneous symmetry breaking in intracavity type II second-harmonic generation with triple resonance. *Opt. Lett.*, 30(3):284–286, 2005.

[251] M. van Herpen, S. te Lintel Hekkert, S.E. Bisson, and F.J.M. Harren. Wide single-mode tuning of a 3.0-3.8-μm, 700-mW, continuous-wave Hd:YAG-pumped optical parametric oscillator based on periodically poled lithium niobate. *Opt. Lett.*, 27(8):640–642, 2002.

[252] M.E. Klein, P. Gross, K.-J. Boller, M. Auerbach, P. Wessels, and C. Fallnich. Rapidly tunable continuous-wave optical parametric oscillator pumped by a fiber laser. *Opt. Lett.*, 28(11):920–922, 2003.

[253] P. Gross, M.E. Klein, H. Ridderbusch, D.-H. Lee, J.-P. Meyn, R. Wallenstein, and K.-J. Boller. Wide wavelength tuning of an optical parametric oscillator through electro-optic shaping of the gain spectrum. *Opt. Lett.*, 27(16):1433–1435, 2002.

[254] L.B. Kreuzer. Single and multimode oscillation of the singly resonant optical parametric oscillator. *Proc. of the joint conf. on lasers and optoelectronics (Institution of Electronic and Radio Engineers, London)*, pages 52–63, 1969.

[255] C.R. Phillips and M.M. Fejer. Stability of the singly resonant optical parametric oscillator. *J. Opt. Soc. Am. B*, 27(12):2687–2699, 2010.

[256] S. Zaske, D.-H. Lee, and C. Becher. Green-pumped cw singly resonant optical parametric oscillator based on MgO:PPLN with frequency stabilization to an atomic resonance. *Appl. Phys. B*, 98:729–735, 2010.

[257] A.J. Henderson, M.J. Padgett, J. Zhang, W. Sibbett, and M.H. Dunn. Continuous frequency tuning of a cw optical parametric oscillator through tuning of its pump source. *Opt. Lett.*, 20(9):1029–1031, 1995.

[258] A.J. Henderson, P.M. Roper, L.A. Borschowa, and R.D. Mead. Stable, continuously tunable operation of a diode-pumped doubly resonant optical parametric oscillator. *Opt. Lett.*, 25(17):1264–1266, 2000.

[259] M. Bode, P.K. Lam, I. Freitag, A. Tunnermann, H.-A. Bachor, and H. Welling. Continuously-tunable doubly resonant optical parametric oscillator. *Opt. Comm.*, 148:117–121, 1998.

[260] I. Ribet, C. Drag, M. Lefebvre, and E. Rosencher. Widely tunable single-frequency pulses optical parametric oscillator. *Opt. Lett.*, 27(4):255–257, 2002.

[261] P. Suret, M. Lefranc, D. Derozier, J. Zemmouri, and S. Bielawski. Periodic mode hopping induced by thermo-optic effects in continuous-wave optical parametric oscillators. *Opt. Lett.*, 26(18):1415–1417, 2001.

[262] T. Ikegami, S. Slyusarev, and S. Ohshima. Characteristics of continuous-wave, doubly-resonant optical parametric oscillators as spectroscopic tools. *Proceedings of SPIE*, 4269:210–216, 2001.

[263] A. Douillet, J.-J. Zondy, A. Yelisseyev, S. Lobanov, and L. Isaenko. Stability and frequency tuning of thermally loaded continuous-wave $AgGaS_2$ optical parametric oscillators. *J. Opt. Soc. Am. B*, 16(9):1481–1498, 1999.

[264] D.K. Serkland, R.C. Eckardt, and R.L. Byer. Continuous-wave total-internal-reflection optical parametric oscillator pumped at 1064 nm. *Opt. Lett.*, 19(14):1046–1048, 1994.

[265] P.L. Hansen and P. Buchhave. Thermal self-frequency locking of a doubly resonant optical parametric oscillator. *Opt. Lett.*, 22(14):1074–1076, 1997.

[266] D.-H. Lee, M.E. Klein, and K.-J. Boller. Intensity noise of pump-enhanced continuous-wave optical parametric oscillators. *Appl. Phys. B*, 66:747–753, 1998.

[267] M. Scheidt, M.E. Klein, and K.J. Boller. Spiking in pump enhanced idler resonant optical parametric oscillators. *Opt. Comm.*, 149:108–112, 1998.

[268] M.J. Lawrence, R.L. Byer, M.A. Arbore, and J.D. Kmetec. Wide-bandwidth 25-dB amplitude noise suppression in a pump-and-signal-resonant optical parametric oscillator. *Opt. Lett.*, 26(14):1087–1089, 2001.

[269] I. Breunig, D. Haertle, and K. Buse. Continuous-wave optical parametric oscillators: recent developments and prospects. *Appl. Phys. B*, 105:99–111, 2011.

[270] X. Wei, N. Wu, X. Liu, and X. Li. Theoretical study of relaxation oscillation in triply resonant OPOs. *Appl. Phys. B*, 79(7):841–844, 2004.

[271] A. Amon and M. Lefranc. Topological signature of deterministic chaos in short nonstationary signals from an optical parametric oscillator. *Phys. Rev. Lett.*, 92(9):094101–1–4, 2004.

[272] C. Richy, K.I. Petsas, E. Giacobino, C. Fabre, and L. Lugiato. Observation of bistability and delayed bifurcation in a triply resonant optical parametric oscillator. *J. Opt. Soc. Am. B*, 12(3):456–461, 1995.

[273] C. Izus, M. Santagiustina, M. San Miguel, and P. Colet. Pattern formation in the presence of walk-off for a type II optical parametric oscillator. *J. Opt. Soc. Am. B*, 16(9):1592–1596, 1999.

[274] S. Trillo, M. Haelterman, and A. Sheppard. Stable topological spatial solitons in optical parametric oscillators. *Opt. Lett.*, 22(13):970–972, 1997.

[275] M. Vaupel, A. Maitre, and C. Fabre. Observation of pattern formation in optical parametric oscillators. *Phys. Rev. Lett.*, 83(25):5278–5281, 1999.

[276] U. Simon, S. Waltman, I. Loa, F.K. Tittel, and L. Hollberg. External-cavity difference-frequency source near 3.2 μm, based on combining a tunable diode laser with a diode-pumped Nd:YAG laser in $AgGaS_2$. *J. Opt. Soc. Am. B*, 12(2):323–327, 1995.

[277] K.P. Petrov, S. Waltman, U. Simon, R.F. Curl, F.K. Tittel, E.J. Dlugokencky, and L. Hollberg. Detection of methane in air using diode-laser pumped difference-frequency generation near 3.2 μm. *Appl. Phys. B*, 61:553–558, 1995.

[278] J.-J. Zondy, V. Vedenyapine, T. Kaing, D. Lee, A. Yelisseyev, L. Isaenko, and S. Lobanov. Doppler spectroscopy of NH_3 and SF_6 in the 10-μm range with a tunable $AgGaS_2$ difference-frequency spectrometer. *Appl. Phys. B*, 78(3-4):457–463, 2004.

[279] B. Lai, N.C. Wong, and L.K. Cheng. Continuous-wave tunable light source at 1.6 μm by difference-frequency mixing in $CsTiOAsO_4$. *Opt. Lett.*, 20(17):1779–1781, 1995.

[280] E. Peters, S.A. Diddams, P. Fendel, S. Reinhardt, T.W. Hansch, and Th. Udem. A deep-UV optical frequency comb at 205 nm. *Opt. Express*, 17(11):9183–9190, 2009.

[281] F.O. Ilday and F.X. Kartner. Cavity-enhanced optical parametric chirped-pulse amplification. *Opt. Lett.*, 31(5):637–639, 2006.

[282] A. Esteban-Martin, O. Kokabee, K. Moutzouris, and M. Ebrahim-Zadeh. High-harmonic-repetition-rate, 1 GHz femtosecond optical parametric oscillator pumped by a 76 MHz Ti:sapphire laser. *Opt. Lett.*, 34(4):428–430, 2009.

[283] O. Kokabee, A. Esteban-Martin, and M. Ebrahim-Zadeh. Extended-cavity, tunable, GHz-repetition-rate femtosecond optical parametric oscillator pumped at 76 MHz. *Opt. Express*, 17(18):15635–15640, 2009.

[284] J. Jiang and T. Hasama. Synchronously pumped femtosecond optical parametric oscillator based on an improved pumping concept. *Opt. Comm.*, 220:193–202, 2003.

[285] J.D. Rowley, S. Yang, and F. Ganikhanov. Power and tuning characteristics of a broadly tunable femtosecond optical parametric oscillator based on periodically poled stoichiometric lithium tantalate. *J. Opt. Soc. Am. B*, 28(5):1026–1036, 2012.

[286] E.O. Potma, W.P. de Boeij, M.S. Pshenichnikov, and D.A. Wiersma. 30-fs, cavity-dumped optical parametric oscillator. *Opt. Lett.*, 23(22):1763–1765, 1998.

[287] T.P. Lamour and D.T. Reid. 650-nJ pulses from a cavity-dumped Yb:fiber-pumped ultrafast optical parametric oscillator. *Opt. Express*, 19(18):17557–17562, 2011.

[288] B. Ruffing, A. Nebel, and R. Wallenstein. All-solid-state cw mode-locked picosecond $KTiOAsO_4$ (KTA) optical parametric oscillator. *Appl. Phys. B*, 67:537–544, 1998.

[289] L. Lefort, K. Puech, S.D. Butterworth, Y.P. Svirko, and D.C. Hanna. Generation of femtosecond pulses from order-of-magnitude pulse compression in a synchronously pumped optical parametric oscillator based on periodically poled lithium niobate. *Opt. Lett.*, 24(1):28–30, 1999.

[290] J. Prawiharjo, H.S.S. Hung, D.C. Hanna, and D.P. Shepherd. Numerical investigations of parametric transfer in synchronously pumped optical parametric oscillators for indirect mid-infrared pulse shaping. *J. Opt. Soc. Am. B*, 24(9):2484–2493, 2007.

[291] Z. Zhang, J. Sun, T. Gardiner, and D.T. Reid. Broadband conversion in an Yb:KYW-pumped ultrafast optical parametric oscillator with a long nonlinear crystal. *Opt. Express*, 19(18):17127–17132, 2011.

[292] H.S.S. Hung, J. Prawiharjo, N.K. Daga, D.C. Hanna, and D.P. Shepherd. Experimental investigation of parametric transfer in synchronously pumped optical parametric oscillators. *J. Opt. Soc. Am. B*, 24(12):2998–3006, 2007.

[293] C.-K. Min and T. Joo. Near-infrared cavity-dumped femtosecond optical parametric oscillator. *Opt. Lett.*, 30(14):1855–1857, 2005.

[294] D. Artigas and D.T. Reid. Efficient femtosecond optical parametric oscillators based on aperiodically poled nonlinear crystals. *Opt. Lett.*, 27(10):851–853, 2002.

[295] K.A. Tillman, D.T. Reid, D. Artigas, J. Hellstrom, V. Pasiskevicius, and F. Laurell. Low-threshold, high-repetition-frequency femtosecond optical parametric oscillator based on chirped-pulse frequency conversion. *J. Opt. Soc. Am. B*, 20(6):1309–1316, 2003.

[296] M. Ghotbi, A. Esteban-Martin, and M. Ebrahim-Zadeh. BiB_3O_6 femtosecond optical parametric oscillator. *Opt. Lett.*, 31(21):3128–3130, 2006.

[297] D.T. Reid, C. McGowan, M. Ebrahimzadeh, and W. Sibbett. Characterization and modeling of a noncollinearly phase-matched femtosecond optical parametric oscillator based on KTA and operating to beyond 4 μm. *IEEE J. Quant. Elect.*, 33(1):1–9, 1997.

[298] K.-J. Han, D.-W. Jang, J.-H. Kim, C.-K. Min, T.-H. Joo, Y.-S. Lim, D. Lee, and K.-J. Yee. Synchronously pumped optical parametric oscillator based on periodically poled MgO-doped lithium niobate. *Opt. Express*, 16(8):5299–5304, 2008.

[299] Z.P. Zhang, J. Hebling, J. Kuhl, W.W. Ruhle, L. Palfalvi, and H. Giessen. Femtosecond near-IR optical parametric oscillator with efficient intracavity generation of visible light. *J. Opt. Soc. Am. B*, 19(10):2479–2488, 2002.

[300] F. Kienle, P.S. Teh, D. Lin, S. Alam, J.H.V. Price, D.C. Hanna, D.J. Richardson, and D.P. Shepherd. High-power, high repetition-rate, green-pumped, picosecond LBO optical parametric oscillator. *Opt. Express*, 20(7):7008–7014, 2012.

[301] M.E. Fermann, V.I. Kruglov, B.C. Thomsen, J.M. Dudley, and J.D. Harvey. Self-similar propagation and amplification of parabolic pulses in optical fibers. *Phys. Rev. Lett.*, 84(26):6010–6013, 2000.

[302] V.I. Kruglov and J.D. Harvey. Asymptotically exact parabolic solutions of the generalized nonlinear Schrodinger equation with varying parameters. *J. Opt. Soc. Am. B*, 23(12):2541–2550, 2006.

[303] F. Wang, G. Xie, P. Yuan, L. Qian, and D. Tang. Similaritions formation in synchronously pumped singly resonant optical parametric oscillators. *arXiv*, 1312.4651:1–4, 2013.

[304] D.T. Reid, J.M. Dudley, M. Ebrahimzadeh, and W. Sibbett. Soliton formation in a femtosecond optical parametric oscillator. *Opt. Lett.*, 19(11):825–827, 1994.

[305] F. Hache, A. Zeboulon, G. Gallot, and G.M. Gale. Cascaded second-order effects in the femtosecond regime in β-barium borate: self-compression in a visible femtosecond optical parametric oscillator. *Opt. Lett.*, 20(14):1556–1558, 1995.

[306] G.M. Gale, M. Cavallari, and F. Hache. Femtosecond visible optical parametric oscillator. *J. Opt. Soc. Am. B*, 15(2):702–714, 1998.

[307] E.S. Wachman, D.C. Edelstein, and C.L. Tang. Continuous-wave mode-locked and dispersion-compensated femtosecond optical parametric oscillator. *Opt. Lett.*, 15(2):136–138, 1990.

[308] J. Seres and J. Hebling. Nonstationary theory of synchronously pumped femtosecond optical parametric oscillators. *J. Opt. Soc. Am. B*, 17(5):741–750, 2000.

[309] R. Paschotta. Noise of mode-locked lasers (part I): numerical model. *Appl. Phys. B*, 79:153–162, 2004.

[310] G. D'Alessandro and C.B. Laforet. Giant noise amplification in synchronously pumped optical parametric oscillators. *Opt. Lett.*, 34(5):614–616, 2009.

[311] T. Land, T. Binhammer, S. Rausch, G. Palmer, M. Emons, M. Schultze, A. Harth, and U. Morgner. High power ultra-widely tunable femtosecond pulses from a non-collinear optical parametric oscillator (NOPO). *Opt. Express*, 20(2):912–917, 2011.

[312] A.J. Scroggie, G. D'Alessandro, N. Langford, and G.-L. Oppo. Pulse compression by slow saturable absorber action in an optical parametric oscillator. *Opt. Comm.*, 160:119–124, 1999.

[313] X. Zhang and H. Giessen. Four-wave mixing based on cascaded second-order nonlinear processes in a femtosecond optical parametric oscillator operating near degeneracy. *Appl. Phys. B*, 79:441–447, 2004.

[314] J.E. Schaar, K.L. Vodopyanov, and M.M. Fejer. Intracavity terahertz-wave generation in a synchronously pumped optical parametric oscillator using quasi-phase-matched GaAs. *Opt. Lett.*, 32(10):1284–1286, 2007.

[315] K. Puech, L. Lefort, and D.C. Hanna. Broad tuning around degeneracy in a singly resonant synchronously pumped parametric oscillator by means of a diffraction grating. *J. Opt. Soc. Am. B*, 16(9):1533–1538, 1999.

[316] R. Gebs, T. Dekorsy, S.A. Diddams, and A. Bartels. 1-GHz repetition rate femtosecond OPO with stabilized offset between signal and idler frequency combs. *Opt. Express*, 16(8):5397–5405, 2008.

[317] T.I. Ferreiro, J. Sun, and D.T. Reid. Frequency stability of a femtosecond optical parametric oscillator frequency comb. *Opt. Express*, 19(24):24159–24164, 2011.

[318] N. Coluccelli, H. Fonnum, M. Haakestad, A. Gambetta, D. Gatti, M. Marangoni, P. Laporta, and G. Galzerano. 250-MHz synchronously pumped optical parametric oscillator at 2.25-2.6 μm and 4.1-4.9 μm. *Opt. Express*, 20(20):22042–22047, 2012.

[319] S.T. Wong, K.L. Vodopyanov, and R.L. Byer. Self-phase-locked divide-by-2 optical parametric oscillator as a broadband frequency comb source. *J. Opt. Soc. Am. B*, 27(5):876–882, 2003.

[320] C.W. Rudy, A. Marandi, K.A. Ingold, S.J. Wolf, K.L. Vodopyanov, R.L. Byer, L. Yang, P. Wan, and J. Liu. Sub-50 fs pulses around 2070 nm from a synchronously-pumped, degenerate OPO. *Opt. Express*, 20(25):27589–27595, 2012.

[321] K.F. Lee, J. Jiang, C. Mohr, J. Bethge, M.E. Fermann, N. Leindecker, K.L. Vodopyanov, P.G. Schunemann, and I. Hartl. Carrier envelope offset frequency of a doubly resonant, nondegenerate, mid-infrared GaAs optical parametric oscillator. *Opt. Lett.*, 38(8):1191–1193, 2013.

[322] N. Forget, S. Bahbah, C. Drag, F. Bretenaker, M. Lefebvre, and E. Rosencher. Actively mode-locked optical parametric oscillator. *Opt. Lett.*, 31(7):972–974, 2006.

[323] J.-M. Melkonian, N. Forget, F. Bretenaker, C. Drag, M. Lefebvre, and E. Rosencher. Active mode locking of continuous-wave doubly and singly resonant optical parametric oscillators. *Opt. Lett.*, 32(12):1701–1703, 2007.

[324] K. Devi, S.C. Kumar, and M. Ebrahim-Zadeh. Mode-locked, continuous-wave, singly resonant optical parametric oscillator. *Opt. Lett.*, 37(18):3909–3911, 2012.

[325] A. Esteban-Martin, G.K. Samanta, K. Devi, S.C. Kumar, and M. Ebrahim-Zadeh. Frequency-modulation-mode-locked optical parametric oscillator. *Opt. Lett.*, 37(1):115–117, 2012.

[326] R. Laenen and T. Roth. Numerical study and experimental results for a synchronously pumped optical parametric oscillator in the saturation regime. *J. Opt. Soc. Am. B*, 14(2):454–459, 1997.

[327] A.V. Smith, R.J. Gehr, and M.S. Bowers. Numerical models of broad-bandwidth nanosecond optical parametric oscillators. *J. Opt. Soc. Am. B*, 16(4):609–619, 1999.

[328] C. Canalias and V. Pasiskevicius. Mirrorless optical parametric oscillator. *Nature Photonics*, 1:459–462, 2007.

[329] A.K. Popov, S.A. Myslivets, and V.M. Shalaev. Microscopic mirrorless negative-index optical parametric oscillator. *Opt. Lett.*, 34(8):1165–1167, 2009.

[330] G. Rustad, G. Arishold, and O. Farsund. Effect of idler absorption in pulsed optical parametric oscillators. *Opt. Express*, 19(3):2815–2830, 2011.

[331] D.J. Armstrong and A.V. Smith. 90% pump depletion and good beam quality in a pulse-injection-seeded nanosecond optical parametric oscillator. *Opt. Lett.*, 31(3):380–382, 2006.

[332] G.T. Moore and K. Koch. Efficient high-gain two-crystal optical parametric oscillator. *IEEE J. Quant. Elect.*, 31(5):761–768, 1995.

[333] A.V. Smith. Bandwidth and group-velocity effects in nanosecond optical parametric amplifiers and oscillators. *J. Opt. Soc. Am. B*, 22(9):1953–1965, 2005.

[334] D.J. Armstrong and A.V. Smith. Tendency of nanosecond optical parametric oscillators to produce purely phase-modulated light . *Opt. Lett.*, 21(20):1634–1636, 1996.

[335] D.J. Armstrong and A.V. Smith. Demonstration of a frequency-modulated, pulsed optical parametric oscillator. *Appl. Phys. Lett.*, 70(10):1227–1229, 1997.

[336] A. Borsutzky. Frequency control of pulsed optical parametric oscillators. *Quant. Semiclass. Opt.*, 9:191–207, 1997.

[337] J.G. Haub, R.M. Hentschel, M.J. Johnson, and B.J. Orr. Controlling the performance of a pulsed optical parametric oscillator: a survey of techniques and spectroscopic applications. *J. Opt. Soc. Am. B*, 12(11):2128–2141, 1995.

[338] F. Ganikhanov, T. Caughey, and K.L. Vodopyanov. Narrow-linewidth middle-infrared $ZnGeP_2$ optical parametric oscillator. *J. Opt. Soc. Am. B*, 18(6):818–822, 2001.

[339] J. Saikawa, M. Fujii, H. Ishizuki, and T. Taira. 52 mJ narrow-bandwidth degenerated optical parametric system with a large-aperture periodically poled MgO:$LiNbO_3$ device. *Opt. Lett.*, 31(21):3149–3151, 2006.

[340] J. Saikawa, M. Fujii, H. Ishizuki, and T. Taira. High-energy, narrow-bandwidth periodically poled Mg-doped $LiNbO_3$ optical parametric oscillator with a volume Bragg grating. *Opt. Lett.*, 32(20):2996–2998, 2007.

[341] M. Henriksson, L. Sjoqvist, V. Pasiskevicius, and F. Laurell. Mode spectrum of multi-longitudinal mode pumped near-degenerate OPOs with volume Bragg grating output couplers. *Opt. Express*, 17(20):17582–17589, 2009.

[342] B. Jacobsson, V. Pasiskevicius, F. Laurell, E. Rotari, V. Smirnov, and L. Glebov. Tunable narrowband optical parametric oscillator using a transversely chirped Bragg grating. *Opt. Lett.*, 34(4):449–451, 2009.

[343] P. Blau, S. Pearl, S. Fastig, and R. Lavi. Single-mode operation of a mid-infrared optical parameteric oscillator using volume-Bragg-grating cavity mirrors. *IEEE J. Quant. Elect.*, 44(9):867–871, 2008.

[344] J.E. Bjorkholm and H.G. Danielmeyer. Frequency control of a pulsed optical parametric oscillator by radiation injection. *Appl. Phys. Lett.*, 15(6):171–173, 1969.

[345] Y. He, G.W. Baxter, and B.J. Orr. Locking the cavity of a pulsed periodically poled lithium niobate optical parametric oscillator to the wavelength of a continuous-wave injection seeder by an 'intensity-dip' method. *Rev. Sci. Inst.*, 70:3203–3213, 1999.

[346] T.W. Hansch and B. Couillaud. Laser frequency stabilization by polarization spectroscopy of a reflecting reference cavity. *Opt. Comm.*, 35(3):441–444, 1980.

[347] R.W.P. Drever, J.L. Hall, F.V. Kowalski, J. Hough, G.M. Ford, A.J. Munley, and H. Ward. Laser phase and frequency stabilization using an optical resonator. *Appl. Phys. B*, 31(2):97–105, 1983.

[348] Y. He and B.J. Orr. Narrowband tuning of an injection-seeded pulsed optical parametric oscillator based on a self-adaptive, phase-conjugate cavity mirror. *Opt. Lett.*, 29(18):2169–2171, 2004.

[349] Y. He and B.J. Orr. Self-adaptive, narrowband tuning of a pulsed optical parametric oscillator and a continuous-wave diode laser via phase-conjugation photorefractive cavity reflectors: verification by high-resolution spectroscopy. *Appl. Phys. B*, 96(2-3):545–560, 2009.

[350] M. Lefebvre, B. Scherrer, and J.-C. Lestel. Raman injected optical parametric oscillator. *Opt. Comm.*, 139:241–246, 1997.

[351] S. Haidar and H. Ito. Injection-seeded optical parametric oscillator for efficient difference frequency generation in mid-IR. *Opt. Comm.*, 171:171–176, 1999.

[352] T.D. Raymond, W.J. Alford, A.V. Smith, and M.S. Bowers. Frequency shifts in injection-seeded optical parametric oscillators with phase mismatch. *Opt. Lett.*, 19(19):1520–1522, 1994.

[353] R.T. White, Y. He, B.J. Orr, M. Kono, and K.G.H. Baldwin. Control of frequency chirp in nanosecond-pulsed laser spectroscopy. 3. Spectro-temporal dynamics of an injection-seeded optical parametric oscillator. *J. Opt. Soc. Am. B*, 24(10):2601–2609, 2007.

[354] R.T. White, Y. He, B.J. Orr, M. Kono, and K.G.H. Baldwin. Control of frequency chirp in nanosecond-pulsed laser spectroscopy. 2. A long-pulse optical parametric oscillator for narrow optical bandwidth. *J. Opt. Soc. Am. B*, 21(9):1586–1594, 2004.

[355] D.C. Hovde, J.H. Timmermans, G. Scoles, and K.K. Lehmann. High power injection seeded optical parametric oscillator. *Opt. Comm.*, 86:294–300, 1991.

[356] R.T. White, Y. He, B.J. Orr, M. Kono, and K.G.H. Baldwin. Transition from single-mode to multimode operation of an injection-seeded pulsed optical parametric oscillator. *Opt. Express*, 12:5655–5660, 2004.

[357] J.H. Marquardt, R.W. Mackes, and D.D. Smith. Single-mode, tunable output from a midwave-infrared-seeded optical parametric oscillator system. *Appl. Opt.*, 41(6):1163–1168, 2002.

[358] Y. He and B.J. Orr. Tunable single-mode operation of a pulsed optical parametric oscillator pumped by a multimode laser. *Appl. Opt.*, 40(27):4836–4848, 2001.

[359] B. Hardy, A. Berrou, S. Guilbaud, M. Raybaut, A. Godard, and M. Lefebvre. Compact, single-frequency, doubly resonant optical parametric oscillator pumped in an achromatic phase-adapted double-pass geometry. *Opt. Lett.*, 36(5):678–680, 2011.

[360] B. Scherrer, I. Ribet, A. Godard, E. Rosencher, and M. Lefebvre. Dual-cavity doubly resonant optical parametric oscillators: demonstration of pulsed single-mode operation. *J. Opt. Soc. Am. B*, 17(10):1716–1729, 2000.

[361] C. Drag, A. Desormeaux, M. Lefebvre, and E. Rosencher. Entangled-cavity optical parametric oscillator for mid-infrared pulsed single-longitudinal-mode operation. *Opt. Lett.*, 27(14):1238–1240, 2002.

[362] M. Raybaut, T. Schmid, A. Godard, A.K. Mohamed, M. Lefebvre, F. Marnas, P. Flamant, A. Bohman, P. Geiser, and P. Kaspersen. High-energy single-longitudinal mode nearly diffraction-limited optical parametric source with 3 MHz frequency stability for CO_2 DIAL. *Opt. Lett.*, 34(13):2069–2071, 2009.

[363] Y.J. Ding and J.B. Khurgin. Backward optical paramteric oscillators and amplifiers. *IEEE J. Quant. Elect.*, 32(9):1574–1582, 1996.

[364] H. Su, S. Ruan, and Y. Guo. Generation of mid-infrared wavelengths larger than 4.0 μm in a mirrorless counterpropagating configuration. *J. Opt. Soc. Am. B*, 223(8):1626–1629, 2006.

[365] G. Anstett, A. Borsutzky, and R. Wallenstein. Investigations of the spatial beam quality of pulsed ns-OPOs. *Appl. Phys. B*, 76:541–545, 2003.

[366] X. Liang, J. Bartschke, M. Peltz, and J.A. L'Hullier. Non-collinear nanosecond optical paramteric oscillator based on periodically poled LN with tilted domain walls. *Appl. Phys. B*, 87:649–653, 2007.

[367] A.V. Smith and M.S. Bowers. Image-rotating cavity designs for improved beam quality in nanosecond optical parametric oscillators. *J. Opt. Soc. Am. B*, 18(5):706–713, 2001.

[368] D.J. Armstrong and A.V. Smith. Demonstration of improved beam quality in an image-rotating optical parametric oscillator. *Opt. Lett.*, 27(1):40–42, 2002.

[369] O. Farsund, G. Arisholm, and G. Rustad. Improved beam quality from a high energy optical parametric oscillator using crystals with orthogonal critical planes. *Opt. Express*, 18(9):9229–9235, 2010.

[370] A.V. Smith and D.J. Armstrong. Nanosecond optical parametric oscillator with 90° image rotation: design and performance. *J. Opt. Soc. Am. B*, 19(8):1801–1814, 2002.

[371] S. Pearl, Y. Ehrlich, S. Fastig, and S. Rosenwaks. Nearly diffraction-limited signal generated by a lower beam-quality pump in an optical parametric oscillator. *Appl. Opt.*, 42(6):1048–1051, 2003.

[372] B.C. Johnson, V.J. Newell, J.B. Clark, and E.S. McPhee. Narrow-bandwidth low-divergence optical parametric oscillator for nonlinear

frequency-conversion applications. *J. Opt. Soc. Am. B*, 12(11):2122–2127, 1995.

[373] G. Hansson, H. Karlsson, and F. Laurell. Unstable resonator optical parametric oscillator based on quasi-phase-matched $RbTiOAsO_4$. *Appl. Opt.*, 40(30):5446–5451, 2001.

[374] W.J. Alford, R.J. Gehr, R.L. Schmitt, A.V. Smith, and G. Arisholm. Beam tilt and angular dispersion in broad-bandwidth, nanosecond optical parametric oscillators. *J. Opt. Soc. Am. B*, 16(9):1525–1532, 1999.

[375] M.J. Shelton and D.P. West. Degenerate noncollinear emission from a type I collinear parametric oscillator. *Opt. Express*, 9(1):16–23, 2001.

[376] M. Peckus, K. Staliunas, M. Saffman, G. Slekys, V. Sirutkaitis, V. Smilgevicius, and R. Grigonis. Multiconical emission of a monolithic mini-cavity optical parametric oscillator. *Opt. Comm.*, 251:165–171, 2005.

[377] A.V. Smith, D.J. Armstrong, M.C. Phillips, R.J. Gehr, and G. Arisholm. Degenerate type I nanosecond optical parametric oscillators. *J. Opt. Soc. Am. B*, 20(11):2319–2328, 2003.

[378] M. Vaidyanathan, R.C. Eckardt, V. Dominic, L.E. Myers, and T.P. Grayson. Cascaded optical parametric oscillations. *Opt. Express*, 1(2):49–53, 1997.

[379] M. Bache, H. Guo, and B. Zhou. Generating mid-IR octave-spanning supercontinua and few-cycle pulses with solitons in phase-mismatched quatratic nonlinear crystals. *Opt. Mater.*, 3(10):1647–1657, 2013.

[380] C.R. Phillips, C. Langrock, J.S. Pelc, M.M. Fejer, J. Jiang, M.E. Fermann, and I. Hartl. Supercontinuum generation in quasi-phase-matched $LiNbO_3$ waveguide pumped by a Tm-doped fiber laser system. *Opt. Lett.*, 36(19):3912–3914, 2011.

[381] G. Mennerat, B. Tropheve, and B. Boulanger. Experimental demonstration of five-beam-pumped optical parametric amplification. *Opt. Lett.*, 38(17):3319–3321, 2013.

[382] A. Dubietis, R. Danielius, G. Tamosauskas, and A. Piskarskas. Combining effect in a multiple-beam-pumped optical parametric amplifier. *J. Opt. Soc. Am. B*, 15(3):1135–1139, 1998.

[383] C.R. Phillips, L. Gallmann, and M.M. Fejer. Design of quasi-phasematching gratings via convex optimization. *Opt. Express*, 21(8):10139–10159, 2013.

[384] M. Asobe, O. Tadanaga, H. Miyazawa, Y. Nishida, and H. Suzuki. Multiple quasi-phase-matched $LiNbO_3$ wavelength converter with a continuously phase-modulated domain structure. *Opt. Lett.*, 28(7):558–560, 2002.

[385] C.R. Phillips and M.M. Fejer. Adiabatic optical parametric oscillators: steady-state and dynamical behavior. *Opt. Express*, 20(3):2466–2482, 2012.

[386] T. Umeki, M. Asobe, Y. Nishida, O. Tadanaga, K. Magari, T. Yanagawa, and H. Suzuki. Widely tunable 3.4 μm band difference frequency generation using apodized $\chi^{(2)}$ grating. *Opt. Lett.*, 32(9):1129–1131, 2007.

[387] A. Tehranchi and R. Kashyap. Engineered gratings for flat broadening of second-harmonic phase-matching bandwidth in MgO-doped lithium niobate waveguides. *Opt. Express*, 16(23):18970–18975, 2008.

[388] Y.W. Lee, F.C. Fan, Y.C. Huang, B.Y. Gu, B.Z. Dong, and M.H. Chou. Nonlinear multiwavelength conversion based on an aperiodic optical superlattice in lithium niobate. *Opt. Lett.*, 27(24):2191–2193, 2002.

[389] C.L. Chang, Y.H. Chen, C.H. Lin, and J.Y. Chang. Monolithically integrated multi-wavelength filter and second harmonic generator in aperiodically poled lithium niobate. *Opt. Express*, 16(22):18535–18544, 2008.

[390] M.A. Arbore, A. Galvanauskas, D. Harter, M.H. Chou, and M.M. Fejer. Engineerable compression of ultrashort pulses by use of second-harmonic generation in chirped-period-poled lithium niobate. *Opt. Lett.*, 22(17):1341–1343, 1997.

[391] G. Imeshev, A. Galvanauskas, D. Harter, M.A. Arbore, M. Proctor, and M.M. Fejer. Engineerable femtosecond pulse shaping by second-harmonic generation with Fourier synthetic quasi-phase-matching gratings. *Opt. Lett.*, 23(11):864–866, 1998.

[392] L. Kornaszewski, M. Kohler, U.K. Sapaev, and D.T. Reid. Designer femtosecond pulse shaping using grating-engineered quasi-phase-matching in lithium niobate. *Opt. Lett.*, 33(4):378–380, 2008.

[393] C. Heese, C.R. Phillips, L. Gallmann, M.M. Fejer, and U. Keller. Ultrabroadband, highly flexible amplifier for ultrashort midinfrared laser pulses based on aperiodically poled Mg:$LiNbO_3$. *Opt. Lett.*, 35(14):2340–2342, 2010.

[394] O. Yaakobi, M. Clerici, L. Caspani, F. Vidal, and R. Morandotti. Complete pump depletion by autoresonant second harmonic generation in a nonuniform medium. *J. Opt. Soc. Am. B*, 30(6):1637–1642, 2013.

[395] G. Porat and A. Arie. Efficient two-process frequency conversion through a dark intermediate state. *J. Opt. Soc. Am. B*, 29(10):2901–2909, 2012.

[396] S. Longhi. Third-harmonic generation in quasi-phase-matched $\chi^{(2)}$ media with missing second harmonic. *Opt. Lett.*, 32(13):1791–1793, 2007.

[397] N.V. Vitanov, T. Halfmann, B.W. Shore, and K. Bergmann. Laser-induced population transfer by adiabatic passage techniques. *Annu. Rev. Phys. Chem.*, 52:763–809, 2001.

[398] U.K. Sapaev and G. Assanto. Engineered quasi-phase matching for multiple parametric generation. *Opt. Express*, 17(5):3765–3770, 2009.

[399] T.S. Ross and G.T. Moore. Nonresonant recirculating type II second-harmonic generator. *Appl. Opt.*, 43(11):2353–2359, 2004.

[400] M.V. Vasnetsov and S.S. Slyusarenko. Optical instability in non-collinear second-harmonic generation. *Opt. Lett.*, 16(8):542–544, 1991.

[401] K. Koch and G.T. Moore. Singly resonant cavity-enhanced frequency tripling. *J. Opt. Soc. Am. B*, 16(3):448–459, 1999.

[402] L.-B. Chang, S.C. Wang, and A.H. Kung. Numerical analysis of fifth-harmonic conversion of low-power pulsed Nd:YAG laser with resonance of second harmonic. *Jpn. J. Appl. Phys.*, 42:4318–4324, 2003.

[403] G. Kalmani, A. Arie, P. Blau, S. Pearl, and A.V. Smith. Polarization-mixing optical parametric oscillator. *Opt. Lett.*, 30(16):2146–2148, 2005.

[404] J.A.C. Terry, K.J. McEwan, and M.J.P. Payne. A tandem OPO route to the mid-IR. *OSA TOPS Adv. Solid St. Lasers*, 19:236–239, 1998.

[405] C. Fabre, E.J. Mason, and N.C. Wong. Theoretical analysis of self-phase locking in a type II phase-matched optical parametric oscillator. *Opt. Comm.*, 170:299–307, 1999.

[406] E.J. Mason and N.C. Wong. Observation of two distinct phase states in a self-phase-locked type II phase-matched optical parametric oscillator. *Opt. Lett.*, 23(22):1733–1735, 1998.

[407] J.-J. Zondy, A. Douillet, A. Tallet, E. Ressayre, and M. Le Berre. Theory of self-phase-locked optical parametric oscillators. *Phys. Rev. A*, 63:023814–1–14, 2001.

[408] D.-H. Lee, M.E. Klein, J.-P. Meyn, R. Wallenstein, P. Gross, and K.-J. Boller. Phase-coherent all-optical frequency division by three. *Phys. Rev. A*, 67:013808–1–13, 2003.

[409] A. Douillet, J.-J. Zondy, G. Santarelli, A. Makdissi, and A. Clairon. A phase-locked frequency divide-by-3 optical parametric oscillator. *IEEE Trans. on Instr. and Meas.*, 50(2):548–551, 2001.

[410] L. Becouarn, E. Lallier, D. Delacourt, and M. Papuchon. Architecture for high-conversion-efficiency optical parametric oscillators. *J. Opt. Soc. Am. B*, 16(10):1712–1718, 1999.

[411] G.T. Moore, K. Koch, and E.C. Cheung. Optical parametric oscillation with intracavity second-harmonic generation. *Opt. Comm.*, 113:463–470, 1995.

[412] A. Shirakawa, H.W. Mao, and T. Kobayashi. Highly efficient generation of blue-orange femtosecond pulses from intracavity-frequency-mixed optical parametric oscillator. *Opt. Comm.*, 123:121–128, 1996.

[413] O. Aytur and Y. Dikmelik. Plane-wave theory of self-doubling optical parametric oscillators. *IEEE J. Quant. Elect.*, 34(3):447–458, 1998.

[414] G.T. Moore and K. Koch. Optical parametric oscillation with intracavity sum-frequency generation. *IEEE J. Quant. Elect.*, 29(3):961–969, 1993.

[415] G.T. Moore and K. Koch. Optical parametric oscillation with detuned intracavity sum-frequency generation. *IEEE J. Quant. Elect.*, 29(8):2334–2341, 1993.

[416] E.C. Cheung, K. Koch, and G.T. Moore. Frequency upconversion by phase-matched sum-frequency generation in an optical parametric oscillator. *Opt. Lett.*, 19(23):1967–1969, 1994.

[417] F. Ruebel, P. Haag, and J.A. L'huillier. Synchronously pumped femtosecond optical parametric oscillator with integrated sum frequency generation. *Appl. Phys. Lett.*, 92:011122–1–3, 2008.

[418] S.T. Lin, Y.Y. Lin, R.Y. Tu, T.D. Wang, and Y.C. Huang. Fiber-laser-pumped CW OPO for red, green, blue laser generation. *Opt. Express*, 18(3):2361–2367, 2010.

[419] G. Porat, H. Suchowski, Y. Silberberg, and A. Arie. Tunable upconverted optical parametric oscillator with intracavity adiabatic sum-frequency generation. *Opt. Lett.*, 35(10):1590–1592, 2010.

[420] Y. Dikmelik, G. Akgun, and O. Aytur. Plane-wave dynamics of optical parametric oscillation with simultaneous sum-frequency generation. *IEEE J. Quant. Elect.*, 35(6):897–912, 1999.

[421] G.T. Moore and K. Koch. The tandem optical parametric oscillator. *IEEE J. Quant. Elect.*, 32(12):2085–2094, 1996.

[422] G.T. Moore, K. Koch, M.E. Dearborn, and M. Vaidyanathan. A simultaneously phase-matched tandem optical parametric oscillator. *IEEE J. Quant. Elect.*, 34(5):803–810, 1998.

[423] D.B. Kolker, A.K. Dmitriev, P. Gorelik, F. Wong, and J.-J. Zondy. Cascade frequency generation regime in an optical parametric oscillator. *Quantum Electronics*, 39(5):431–434, 2009.

[424] I. Breunig, R. Sowade, and K. Buse. Limitations of the tunability of dual-crystal optical parametric oscillations. *Opt. Lett.*, 32(11):1450–1452, 2007.

[425] P.B. Phua, K.S. Lai, R.F. Wu, and T.C. Chong. High-efficiency mid-infrared $ZnGeP_2$ optical parametric oscillator in a multimode-pumped tandem optical parametric oscillator. *Appl. Opt.*, 38(3):563–565, 1999.

[426] K.J. McEwan and J.A.C. Terry. A tandem periodically-poled lithium niobate (PPLN) optical parametric oscillator (OPO). *Opt. Comm.*, 182:423–432, 2000.

[427] D.-W. Chen and K. Masters. Continuous-wave 4.3-μm intracavity difference frequency generation in an optical parametric oscillator. *Opt. Lett.*, 26(1):25–27, 2001.

[428] D.-W. Chen. Continuous-wave tunable midwave infrared generation near 4.5-μm with an intracavity optical parametric oscillator and difference frequency generation. *Opt. Lett.*, 20(7):1527–1529, 2003.

[429] J.-M. Melkonian, A. Godard, M. Lefebvre, and E. Rosencher. Pulsed optical parametric oscillators with intracavity optical parametric amplification: a critical study. *Appl. Phys. B*, 86(4):663–642, 2007.

[430] T. Chen, B. Wu, W. Liu, P. Jiang, J. Kong, and Y. Shen. Efficient parametric conversion from 1.06 to 3.8 μm by an aperiodically poled cascaded lithium niobate. *Opt. Lett.*, 36(6):921–923, 2011.

[431] Y.H. Liu, Z.D. Xie, W. Ling, Y. Yuan, X.J. Lv, J. Lu, X.P. Hu, G. Zhao, and S.N. Zhu. Efficiency-enhanced optical parametric down conversion for mid-infrared generation on a tandem periodically poled MgO-doped stoichiometric lithium tantalate chip. *Opt. Express*, 19(18):17500–17505, 2011.

[432] O.P. Naraniya, M.R. Shenoy, and K. Thyagarajan. Multiple-wavelength quasi-phase-matching for efficient idler generation in $MgO:LiNbO_3$ based nanosecond optical parametric oscillator. *Appl. Opt.*, 51(9):1312–1317, 2012.

[433] G. Porat, O. Gayer, and A. Arie. Simultaneous parametric oscillation and signal-to-idler conversion for efficient downconversion. *Opt. Lett.*, 35(9):1401–1403, 2010.

[434] D. Artigas and D.T. Reid. High idler conversion in femtosecond optical parametric oscillators. *Opt. Comm.*, 210:113–120, 2002.

[435] K.A. Tillman, D.T. Reid, D. Artigas, and T.Y. Jiang. Idler-resonant femtosecond tandem optical parametric oscillator tuning from 2.1 μm to 4.2 μm. *J. Opt. Soc. Am. B*, 21(8):1551–1558, 2004.

[436] M.E. Dearborn, K. Koch, G.T. Moore, and J.C. Diels. Greater than 100% photon-conversion efficiency from an optical parametric oscillator with intracavity difference-frequency mixing. *Opt. Lett.*, 23(10):759–761, 1998.

[437] G.T. Moore, K. Koch, and M.E. Dearborn. Gain enhancement of multi-stage parametric intracavity frequency conversion. *IEEE J. Quant. Elect.*, 33(10):1734–1742, 1997.

[438] S. Falter, K.-M. Du, Y. Liao, M. Quade, J. Zhang, P. Loosen, and R. Poprawe. Dynamics and stability of a laser system with second-order nonlinearity. *Opt. Lett.*, 22(9):609–611, 1997.

[439] T. Baer. Large-amplitude fluctuations due to longitudinal mode coupling in diode-pumped intracavity-doubled Nd:YAG lasers. *J. Opt. Soc. Am. B*, 3(9):1175–1180, 1986.

[440] K.I. Martin, W.A. Clarkson, and D.C. Hanna. Self-suppression of axial mode hopping by intracavity second-harmonic generation. *Opt. Lett.*, 22(6):375–377, 1997.

[441] M.T. Andersen, P.J. Schlosser, J.E. Hastie, P. Tidemand-Lichtenberg, M.D. Dawson, and C. Pedersen. Singly-resonant sum frequency generation of visible light in a semiconductor disk laser. *Opt. Express*, 17(8):6010–6017, 2009.

[442] G. Cerullo, S. De Silvestri, A. Monguzzi, D. Segala, and V. Magni. Self-starting mode locking of a cw Nd:YAG laser using cascaded second-order nonlinearities. *Opt. Lett.*, 20(7):746–748, 1995.

[443] J.-J. Zondy, F.A. Camargo, T. Zanon, V. Petrov, and N.U. Wetter. Observation of strong cascaded Kerr-lens dynamics in an optimally-coupled intracavity frequency-doubled Hd:YLF ring laser. *Opt. Express*, 18(5):4796–4815, 2010.

[444] K. Stankov. Mode locking by a frequency-doubling crystal: generation of transform-limited ultrashort light pulses. *Opt. Lett.*, 14(7):359–361, 1989.

[445] A.A. Mani, D. Lis, L. Grawet, L. Dreesen, P.A. Thiry, A. Peremans, and Ch. Silien. High energy and short pulses generation by Nd:yttrium aluminum garnet laser mode-locked using frequency-doubling nonlinear mirror. *Opt. Comm.*, 276:135–138, 2007.

[446] H. Iliev, D. Chuchumishev, I. Buchvarov, and V. Petrov. Passive mode-locking of a diode-pumped Nd:YVO_4 laser by intracavity SHG in PPKTP. *Opt. Express*, 18(6):5754–5762, 2010.

[447] V. Couderc, F. Louradour, and A. Barthelemy. 2.8 ps pulses from a mode-locked diode pumped Nd:YVO4 laser using quadratic polarization switching. *Opt. Comm.*, 166:103–111, 1999.

[448] D.J.M. Stothard, J.-M. Hopkins, D. Burns, and M.H. Dunn. Stable, continuous-wave, intracavity, optical parametric oscillator pumped by a semiconductor disk laser (VECSEL). *Opt. Express*, 17(13):10648–10658, 2009.

[449] P. Buchhave, P. Tidemand-Lichtenberg, W. Hou, U.L. Andersen, and H. Abitan. Modelling a singly resonant, intracavity ring optical parametric oscillator. *Opt. Comm.*, 216:191–197, 2003.

[450] T. Debuisschert, J. Raffy, J.-P. Pocholle, and M. Papuchon. Intracavity optical parametric oscillator: study of the dynamics in pulsed regime. *J. Opt. Soc. Am. B*, 13(7):1569–1587, 1999.

[451] H. Zhu, G. Zhang, H. Chen, C. Huang, Y. Wei, Y. Duan, Y. Huang, H. Wang, and G. Qiu. High-efficiency intracavity Nd:YVO_4 KTA optical parametric oscillator with 3.6 W output power at 1.53 μm. *Opt. Express*, 17(23):20669–20674, 2009.

[452] R.F. Wu, P.B. Phua, K.S. Lai, Y.L. Lim, E. Lau, A. Chng, C. Bonnin, and D. Lupinski. Compact 21-W 2-μm intracavity optical parametric oscillator. *Opt. Lett.*, 25(19):1460–1462, 2000.

[453] Y.F. Chen and L.Y. Tsai. Comparison between shared and coupled resonators for passively Q-switched Nd:$GdVO_4$ intracavity optical parametric oscillators. *Appl. Phys. B*, 82:403–406, 2005.

[454] A. Velten, A. Zavadilova, V. Kubecek, and J.-C. Diels. Instabilities in intracavity pumped optical parametric oscillators and methods of stabilization. *Appl. Phys. B*, 98:13–25, 2010.

[455] A. Brenier, D. Jaque, and A. Majchrowski. Bi-functional laser and non-linear optical crystals. *Opt. Mater.*, 28:310–323, 2006.

[456] P. Dekker, J.M. Dawed, J.A. Piper, Y. Liu, and J. Wang. 1.1 W cw self-frequency-doubled diode-pumped Yb:$YAl_3(BO_3)_4$ laser. *Opt. Comm.*, 195:431–436, 2001.

[457] M.J. Lederer, M. Hildebrandt, V.Z. Kolev, B. Luther-Davies, B. Taylor, J. Dawes, P. Dekker, J. Piper, H.H. Tan, and C. Jagadish. Passive mode locking of a self-frequency-doubling Yb:$YAl_3(BO_3)_4$ laser. *Opt. Lett.*, 27(6):436–438, 2002.

[458] Q. Ye, L. Shah, J. Eichenholz, D. Hammons, R. Peale, M. Richardson, A. Chin, and B.H.T. Chai. Investigation of diode-pumped, self-frequency doubled RGB lasers from Nd:YCOB crystals. *Opt. Comm.*, 164:33–37, 1999.

[459] M. Raybaut, A. Godard, R. Haidar, M. Lefebvre, P. Kupecek, P. Lemasson, and E. Rosencher. Generation of mid-infrared radiation by self-difference frequency mixing in chromium-doped zinc selenide. *Opt. Lett.*, 31(2):220–222, 2006.

[460] A.R. Geiger, H. Hemmati, W.H. Farr, and N.S. Prasad. Diode-pumped optical parametric oscillator. *Opt. Lett.*, 21(3):201–203, 1996.

[461] P. Kerkoc, S. Lochran, R.T. Bailey, F.R. Cruickshank, D. Pugh, J.N. Sherwood, and A.J. Blake. Thermal properties of the organic nonlinear optical crystal 4-nitro-4′-methylbenzylidene aniline. *J. Appl. Phys.*, 81(2):624–630, 1997.

[462] P. Kerkoc, S. Horinouchi, K. Sasaki, Y. Nagae, and D. Pugh. Thermal effects on second-harmonic generation in biaxial molecular crystals. *J. Opt. Soc. Am. B*, 16(10):1686–1691, 1999.

[463] V.V. Zelenogorskii and E.A. Khazanov. Influence of the photoelastic effect on the thermal lens in a YLF crystal. *Quantum Electronics*, 40(1):40–44, 2010.

[464] R.C. Miller and W.A. Nordland. Absolute signs of second-harmonic generation coefficients of piezoelectric crystal. *Phys. Rev. B*, 2(12):4896–4902, 1970.

[465] G.T. Moore and K. Koch. Phasing of tandem crystals for nonlinear optical frequency conversion. *Opt. Comm.*, 124:292–294, 1996.

[466] W.G. Cady. *Piezoelectricity*. Dover, 1964.

[467] C. Kittel. *Introduction to solid state physics*. John Wiley and Sons, 1956.

[468] P.N. Butcher. *Nonlinear Optical Phenomena*. Ohio State University Engineering Publications, 1965.

[469] R.J. Gehr, W.J. Alford, and A.V. Smith. Simple method of detecting ferroelectric domains with non-phase-matched second-harmonic generation. *Appl. Opt.*, 37(15):3311–3317, 1998.

[470] T. Mitsui, I. Tatsuzaki, and E. Nakamura. *An introduction to the physics of ferroelectrics*. Gordon and Breach Science Publishers, 1976.

[471] H. Hellwig, J. Liebertz, and L. Bohaty. Linear optical properties of the monoclinic bismuth borate BiB_3O_6. *J. Appl. Phys.*, 88(1):240–244, 2000.

[472] N. Umemura, K. Miyata, and K. Kato. New data on the optical properties of BiB_3O_6. *Opt. Mater.*, 30(4):532–534, 2007.

[473] J.P. Meyn, M.E. Klein, D. Woll, R. Wallenstein, and D. Rytz. Periodically poled potassium niobate for second-harmonic generation at 463 nm. *Opt. Lett.*, 24(16):1154–1156, 1999.

[474] G. Rosenman, A. Skliar, D. Eger, M. Oron, and M. Katz. Low temperature periodic electrical poling of flux-grown $KTiOPO_4$ and isomorphic crystals. *Appl. Phys. Lett.*, 73(25):3650–3652, 1998.

[475] S.C. Buchter, T.Y. Fan, V. Liberman, J.J. Zayhowski, M. Rothschild, E.J. Mason, A. Cassanho, H.P. Jenssen, and J.H. Burnett. Periodically poled BaMgF4 for ultraviolet frequency generation. *Opt. Lett.*, 26(21):1693–1695, 2001.

[476] M.V. Hobden. Optical activity in a non-enantiomorphous crystal: $AgGaS_2$. *Acta Cryst.*, A24:676–680, 1968.

[477] B. Boulanger, J.P. Feve, G. Marnier, B. Menaert, X. Cabirol, P. Villeval, and C. Bonnin. Relative sign and absolute magnitude of $d^{(2)}$ nonlinear coefficients of KTP from second-harmonic-generation measurements. *J. Opt. Soc. Am. B*, 11(5):750–757, 1994.

[478] B. Boulanger, J.P. Feve, G. Marnier, C. Bonnin, P. Villeval, and J.J. Zondy. Absolute measurement of quadratic nonlinearities from phase-matched second-harmonic generation in a single KTP crystal cut as a sphere. *J. Opt. Soc. Am. B*, 14(6):1380–1386, 1997.

[479] S.P. Velsko and D. Eimerl. Second-harmonic generation in sodium lanthanum fluoride. *J. Appl. Phys.*, 62(6):2461–2465, 1987.

[480] P. Kerkoc, R.T. Bailey, F.R. Cruickshank, and D. Pugh. Second-harmonic generation in biaxial crystals for a non-depleted fundamental Gaussian beam. *Pure Appl. Opt.*, 7:L27–L32, 1998.

[481] R.C. Eckardt, H. Masuda, Y.X. Fan, and R.L. Byer. Absolute and relative nonlinear optical coefficients of KDP, KDP^*, BaB_2O_4, $LiIO_3$, MgO:$LiNbO_3$, and KTP measured by phase-matched second-harmonic generation. *IEEE J. Quant. Elect.*, 26(5):922–933, 1990.

[482] W.J. Alford and A.V. Smith. Wavelength variation of the second-order nonlinear coefficients of $KNbO_3$, $KTiOPO_4$, $KTiOAsO_4$, $LiNbO_3$, $LiIO_3$, $\beta-BaB_2O_4$, KH_2PO_4, and LiB_3O_5 crystals: a test of Miller wavelength scaling. *J. Opt. Soc. Am. B*, 18(4):524–533, 2001.

[483] R.L. Byer and S.E. Harris. Power and bandwidth of spontaneous parametric emission. *Phys. Rev.*, 168(3):1064–1068, 1968.

[484] I. Shoji, T. Kondo, and R. Ito. Second-order nonlinear susceptibilities of various dielectric and semiconductor materials. *Opt. Quant. Electron.*, 34:797–833, 2002.

[485] I. Shoji, T. Kondo, A. Kitamoto, M. Shirane, and R. Ito. Absolute scale of second-order nonlinear-optical coefficients. *J. Opt. Soc. Am. B*, 14(9):2268–2294, 1997.

[486] R.J. Gehr and A.V. Smith. Separated-beam nonphase-matched second-harmonic method of characterizing nonlinear optical crystals. *J. Opt. Soc. Am. B*, 15(8):2298–2307, 1998.

[487] N. Bloembergen and P.S. Pershan. Light waves at the boundary of nonlinear media. *Phys. Rev.*, 128(2):606–622, 1962.

[488] W.N. Herman and L.M. Hayden. Maker fringes revisited: second-harmonic generation from birefringent or absorbing materials. *J. Opt. Soc. Am. B*, 12(3):416–427, 1995.

[489] N. Okamoto, Y. Hirano, and O. Sugihara. Precise estimation of nonlinear-optical coefficients for anisotropic nonlinear films with $C_{\infty,v}$ symmetry. *J. Opt. Soc. Am. B*, 9(11):2083–2087, 1992.

[490] J. Jerphagnon and S.K. Kurtz. Maker fringes: a detailed comparison of theory and experiment for isotropic and uniaxial crystals. *J. Appl. Phys.*, 41(4):1667–1681, 1970.

[491] D. Chemla and P. Kupecek. Analyse des experiences de generation de second harmonique. *Revue de Physique Appliquee*, 6(1):31–50, 1971.

[492] P. Pavlides and D. Pugh. General theory of Maker fringes in crystals of low symmetry. *J. Phys.:Condens. Matter*, 3:967–988, 1991.

[493] P.D. Maker, R.W. Terhune, M. Nisenoff, and C.M. Savage. Effects of dispersion and focusing on the production of optical harmonics. *Phys. Rev. Lett.*, 8(1):21–22, 1962.

[494] R. Morita, T. Kondo, Y. Kaneda, A. Sugihashi, N. Ogasawara, S. Umegaki, and R. Ito. Multiple-reflection effects in optical second-harmonic generation. *Jpn. J. Appl. Phys.*, 27(6):L1134–L1136, 1988.

[495] S.X. Dou, M.H. Jiang, Z.S. Shao, and X.T. Tao. Maker fringes in biaxial crystals and the nonlinear optical coefficients of thiosemicarbazide cadmium chloride monohydrate. *Appl. Phys. Lett.*, 54(12):1101–1103, 1989.

[496] M.M. Choy and R.L. Byer. Accurate second-order susceptibility measurements of visible and infrared nonlinear crystals. *Phys. Rev. B*, 14(4):1693–1706, 1976.

[497] S.K. Kurtz and T.T. Perry. A Powder technique for the evaluation of nonlinear optical materials. *J. Appl. Phys.*, 39(8):3798–3813, 1968.

[498] M. Kiguchi, M. Kato, M. Okunaka, and Y. Taniguchi. New method of measuring second harmonic generation efficiency using powder crystals. *Appl. Phys. Lett.*, 60(16):1933–1935, 1992.

[499] A.G. Jackson, M.C. Ohmer, and S.R. LeClair. Relationship of the second order nonlinear optical coefficient to energy gap in inorganic non-centrosymmetric crystals. *Infrared Phys. and Tech.*, 38:233–244, 1997.

[500] I. Shoji, H. Nakamura, K. Ohdaira, T. Kondo, R. Ito, T. Okamoto, K. Tatsuki, and S. Kubota. Absolute measurement of second-order nonlinear-optical coefficients of β-BaB_2O_4 for visible to ultraviolet second-harmonic wavelengths. *J. Opt. Soc. Am. B*, 16(4):620–624, 1999.

[501] D. Eimerl, L. Davis, S. Velsko, E.K. Graham, and A. Zalkin. Optical, mechanical, and thermal properties of barium borate. *J. Appl. Phys.*, 62(5):1968–1983, 1987.

[502] S.P. Velsko, M. Webb, L. Davis, and C. Huang. Phase-matched harmonic generation in lithium triborate (LBO). *IEEE J. Quant. Elect.*, 27(9):2182–2192, 1991.

[503] S.N. Rashkeev, S. Limpijumnong, and W.R.L. Lambrecht. Theoretical evaluation of $LiGaO_2$ for frequency upconversion to ultraviolet. *J. Opt. Soc. Am. B*, 16(12):2217–2222, 1999.

[504] J.E. Sipe and E. Ghahramani. Nonlinear optical response of semiconductors in the independent-particle approximation. *Phys. Rev. B*, 48(16):11705–11722, 1993.

[505] C. Aversa and J.E. Sipe. Nonlinear optical susceptibilities of semiconductors: results with a length-guage analysis. *Phys. Rev. B*, 52(20):14636–14645, 1995.

[506] Z. Lin, Z. Wang, C. Chen, S.K. Chen, and M.-H. Lee. Mechanism for linear and nonlinear optical effects in crystals of the $Sr_2Be_2B_2O_7$ family. *J. Appl. Phys.*, 93(12):9717–9723, 2003.

[507] C. Chen, Z. Shao, J. Jiang, J. Wei, J. Lin, J. Wang, N. Ye, J. Lv, B. Wu, M. Jiang, M. Yoshimura, Y. Mori, and T. Sasaki. Determination of the nonlinear optical coefficients of $YCa_4O(BO_3)_3$ crystal. *J. Opt. Soc. Am. B*, 17(4):566–571, 2000.

[508] Z. Lin, J. Lin, Z. Wang, C. Chen, and M.-H. Lee. Mechanism for linear and nonlinear optical effects in LiB_3O_5, CsB_3O_5, and $CsLiB_6O_{10}$ crystals. *Phys. Rev. B*, 62(3):1757–1764, 2000.

[509] Z. Lin, M.-H. Lee, Z.-P. Liu, C. Chen, and C.J. Pickard. Mechanism for linear and nonlinear optical effects in β-BaB_2O_4 crystals. *Phys. Rev. B*, 60(19):13380–13389, 1999.

[510] D. Xue, K. Kitamura, and J. Wang. Structure-nonlinearity relationship of urea crystal: an *ab initio* study. *Opt. Mater.*, 23:319–322, 2003.

[511] S. Lochran, R.T. Bailey, F.R. Cruickshank, D. Pugh, J.N. Sherwood, G.S. Simpson, P.J. Langley, and J.D. Wallis. The nonlinear optical properties of the crystal (S)-3-methyl-5-nitro-N-(1-phenylethyl)-2-pyridinamine. *J. Phys. Chem. B*, 104(29):6710–6716, 2000.

[512] M.V. Pack, D.J. Armstrong, A.V. Smith, G. Aka, B. Ferrand, and D. Pelenc. Measurement of the $\chi^{(2)}$ tensor of $GdCa_4O(BO_3)_3$ and $YCa_4O(BO_3)_3$ crystals. *J. Opt. Soc. Am. B*, 22(2):417–425, 2005.

Index

M^2, *see* beam quality
Δk, *see* phase mismatch
$\chi^{(2)}$ tensor, *see* d-tensor
$\chi^{(3)}$ tensor, 83–90

absorption
  linear, 62
  two photon, 83–90
acceptance angle, 148, 154, 205
acceptance bandwidth, 148, 205
acceptance temperature, 158
autocorrelation, 240

B & K, *see* Boyd & Kleinman
back conversion, *see* optical parametric oscillator, *see* parametric amplification
beacon effect, 263, 285
beam propagation, *see* propagation
beam quality, 299
  M^2 CW, 299
  M^2 pulsed, 302
biaxial crystal
  D-ellipsoid, 14
  diffraction, 184
  eigenpolarizations, 15, 17, 27
  linear optical properties, 13
  optic axis, 16
  principal axes, 14
  principal planes, 17
  propagation equation, 184, 193–194
  refractive index
    hi & lo index surfaces, 19
  walk off, 18–19, 32
birefringent walk off, *see* Poynting vector, walk off
bound wave, *see* driven wave
Boyd & Kleinman, 273–277, 279–287, 290, 410, 416, 420, 445
Brewster's angle, 47

carrier wave, 168–181, 185–195, 199, 202–204
  definition, 8
cascade mixing, 75, 88, 581

applications, 577
supercontinuum generation, 578
temporal soliton, 578
cavity
impedance matching, 405–409
linear cavity stability, 403
ring cavity stability, 401
stable cavity
design, 401–405
linear, 403
mode matching, 405
ring, 401–403
chalcopyrite, 643
coherence length
definition, 60
confocal parameter, *see* Rayleigh range
convolution
angle, 202
time, 199–202
time & angle, 203
CPOPA, *see* parametric amplification, chirped pulse
cross phase modulation, 86
crystal oscilloscope, 335
crystal symmetry
class
1, 649–650
2, 651–654
$2/m$, 655
222, 656
23, 676
3, 667–669
32, 669
$3m$, 670
4, 661–662
$4/m$, 666
$4/mmm$, 666
422, 664
432, 678
$4mm$, 664
6, 671
$6/m$, 675
$6/mmm$, 675
622, 674
$6mm$, 674
$\bar{1}$, 650
$\bar{3}$, 669
$\bar{3}m$, 671
$\bar{4}$, 662–664
$\bar{4}2m$, 665
$\bar{4}3m$, 677
$\bar{6}$, 673
$\bar{6}m2$, 675
m, 654–655
$m3$, 678
$m3m$, 678
$mm2$, 658–660
mmm, 660
classes, 641
d-tensor, 641
enantiomorphism, 645
ferroelectricity, 646
gyrotropy, 646
piezoelectricity, 647
pyroelectricity, 647
system
cubic, 676–678
hexagonal, 671–676
orthorhombic, 656–660
tetragonal, 660–666
triclinic, 648–656
trigonal, 666–671

D-ellipsoid, 22, 27
biaxial crystal, 14
electro-optic effect, 89
d-tensor, 3
absolute signs, 632
crystal symmetry, 641
definition, 629–632
measurement, 699
separated beams method, 707
quantum calculation, 708
d_{eff}
biaxial crystal, 635

definition, 632–638
plane wave, 54
structured beams, 198–204
direction cosine, 682, 683
isotropic crystal, 634
measurement, 681
Maker fringe method, 701
non-phase matched methods, 687
parametric fluorescence, 686
phase matched methods, 681
powder methods, 704
separated beams method, 692
spherical crystal, 682
Miller scaling, 85, 704
sign of, 268, 639–640
surface, 640
uniaxial crystal, 635
dark intermediate state, 581
degeneracy factor, 1
dielectric tensor, 1, 13, 22, 181
difference frequency mixing
cw cavity, 459–474
triply resonant, 470–472
wave one resonant, 460–463
wave three resonant, 473–474
wave two resonant, 463–464
waves one & three resonant, 464–467
waves one & two resonant, 469–470
waves two & three resonant, 468–469
focused beam, 280–287
Gaussian beam, 263–268
short pulse, 226–228
slanted pulse, 324
diffraction
k-space, 169–172
x-space, 171–172, 177
asymmetric, 172–178, 258
biaxial crystal, 184
Huygens construction, 179
negative, 174
uniaxial crystal, 177, 181
uniaxial rates, 258
dispersion length
definition, 7
displacement, 3, 11
driven wave, 689–697

effective nonlinearity, *see* d_{eff}
eigenmode mixing, 78, 581
adiabatic, 581
eigenpolarization, 25
biaxial crystal, 15
definition, 12
electro-optic effect, 89, 626, 627
elliptic functions, *see* Jacobi elliptic functions
enantiomorphism, 645
envelope function
definition, 8

ferroelectric
domains, 126
poling, 126, 646
ferroelectricity, 646
field envelope, 168–181, 185–195, 198–206, 208
definition, 8
field expansion, 8, 168
focus
astigmatism, 260
cylindrical, 256
Gaussian beam
e-wave, 258
o-wave, 257
radius of curvature, 256
Rayleigh range, 256
spherical, 257
Fourier transform, 9, 168, 171
definition, 8
properties, 9
convolution, 9, 201, 202

shift rule, 179
free wave, 689–697
frequency doubler
recirculating cavity, 582
frequency quadrupler, 584
frequency tripler, 584
Fresnel's formulae, 34
FROG, 238, 334
FWHM, 6

Gaussian beam, 5
$1/e^2$ width, 5
effective area, 5
elliptical, 282
FWHM, 6
Gouy phase, 257–260
radius of curvature, 257
Rayleigh range, 256–260
supergaussian, 7
Gaussian pulse, 5
$1/e^2$ width, 5
dispersive length, 215
frequency chirp, 215
FWHM, 5
Gouy phase, 215
GDD, *see* group delay dispersion
Gouy phase
diffractive, 274–293, 404–405
dispersive, 215–217
grenouille, 334
group delay, 188
group delay dispersion, 7, 188–198, 203
apparent, 316
dispersion length, 215
frequency chirp, 215
Gouy phase, 216
group velocity, 187–190
apparent, 314, 316
polarization pulse, 217
group velocity dispersion, 188–198, 203
group velocity matching
quasi phase matched, 329
second harmonic generation, 321–324, 330
three wave mixing, 324
walk off compensation, 333
GVD, *see* group velocity dispersion
gyrotropy, *see* optical activity

Huygen's construction, 179

imaging, 293
parametric amplification, 296
up conversion, 294
intensity dependent refractive index, *see* n_2
intermediate mixing
definition, 63
irradiance
definition, 2

Jacobi elliptic functions, 71

Kerr effect, *see* n_2
Kleinman symmetry, 86, 630, 643, 648–678

laser
intra cavity mixing
difference frequency, 593
instability, 593
parametric oscillator, 594–597
SHG mode locking, 594
sum frequency, 593
laser/nonlinear crystals, 597
linear electro-optic effect, 610

Maker fringe, *see* d_{eff},measurement
Manley-Rowe relation, 56, 73, 74
Maxwell's equations, 1
diffractive propagation, 181–185
monochromatic plane wave, 11, 32
Miller scaling, 85, 201, 704

mixing angle ϑ, 73
  definition, 55
mixing equations
  broadband, 214
  derivation, 50–55
  plane-wave, monochromatic, 54
  short pulse, 214
  spatial & temporal structure, 203–204
  spatial structure, 202–203, 254
  temporal structure, 199–202
  waveguide, 93
mode matching, *see* cavity, stable
modeling
  analytical, 205
  noise simulation, 208
  numerical, 205
    limitations, 208
  numerical beam propagation, 206

n-ellipse, 15, 27
n_2, 83–85
  cross phase modulation, 86
  effective
    cascade mixing, 75, 88
    electro-optic effect, 88
  self focus, 85
  self phase modulation, 84–85
noise
  quantum, 208–211
  thermal, 211
noncritical, *see* phase matching
nonlinear mixing
  broadband, 214, 229
  cascade mixing, 75, 88
  cavity
    constant field approx., 409
    frequency doubler, 582
    frequency quadrupler, 584
    frequency tripler, 584
  elliptical beams, 282
  energy conservation, 56
  Gaussian beams, 410
  inside laser cavity, 593
  intermediate, 63–70, 288–290
    definition, 63
    strong blue wave, 63
    strong red wave, 68
    summary, 70
  Manley-Rowe, 56
  short pulse, 214, 226
    chirped, 227
    pulse shaping, 235–238
  short pulse measurement, 238–241
  strong, 70–83, 269–273, 290–293
    cyclic, 71
    definition, 70
    eigenmode mixing, 78–83
    phase evolution, 73
    photon balanced, 72
  type 1, 274
  type 2, 274
  vector fields, 298
  waveguide, 90–96
  weak, 58–62, 260–268
    definition, 58
    focused beam, 260
    Gaussian pulse, 217
nonlinear refractive index, *see* n_2
NOPA, 162

OPA, *see* parametric amplification
OPCPA, *see* parametric amplification, chirped pulse
OPG, *see* parametric generation
OPO, *see* optical parametric oscillator
optic axis
  biaxial crystal, 16, 26
  uniaxial crystal, 20
optical activity, 36, 646
optical parametric oscillator
  back conversion

reduced by absorption, 592
reduced by frequency mixing, 592
reduced by Raman, 592
cw, 428–459
mean pump field, 431–432
threshold power, 428–431
triply resonant, 455–459
wave one resonant, 432–440
waves one & three resonant, 449–455
waves one & two resonant, 440–449
cw-pumped, mode locked, 524
intracavity DFG, 591
intracavity SFG, 589
intracavity SHG, 589
nanosecond, 531
anomalies & pathologies, 563
back conversion, 538
backward wave, 535, 556
beam quality, 557–563
broadband operation, 542–548
cluster tuning, 554–556
confocal unstable cavity, 560
cross resonant, 534, 542, 556
efficiency, 535–539
image rotating cavity, 561
injection seeding, 539, 551–554
spectral properties, 548–557
threshold, 532
wave one resonant, 533
wave three resonant, 535
wavelength control, 550–557
waves one & two resonant, 533, 541
stability, 152
synch-pumped, 502–503
cavity dumped, 503
frequency combs, 522–524
influence of n_2, 516–520
influence of GDD, 511–516
influence of group velocity, 504–511
rate multiplied, 503
similariton-like pulses, 517–519
soliton-like pulses, 519–520
stability, 517, 520
threshold, 503–524
wave one resonant, 503–521
waves one & two resonant, 521–522
tandem, 590–591
wavelength doubler, 585–587
wavelength times M, 588
wavelength tripler, 587
optical rectification, 89
orientationally patterned GaAs, 634

parametric amplification
angle multiplexed pumping, 578
back conversion, 229, 234
broadband, 228–229, 234–235
chirped pulse, 228, 325–328
focused beam, 290
Gaussian beam, 272–273
imaging, 296
phase conjugation, 296
wavelength multiplexed pumping, 579
parametric fluorescence, 297, 686
parametric gain, 532
cosh function, 63
gain equation, 63
linewidth gain broadening, 65
low pump depletion, 63
saturation, 272
sinh function, 63
parametric generation, 343
bandwidth, 370, 380, 381
beam quality, 370, 380, 381
cascade mixing, 389
conical emission, 385

degenerate, 363
efficiency, 380, 381
gain bandwidth, 347
gain surface, 352
numerical modeling, 348
diffractive, dispersive, 364
dispersive plane wave, 350
noise simulation, 349
practical implementation, 387
Q-switched pump, 361
seeded, 374
beam quality, 377
efficiency, 355, 377
partial, 375
peak irradiance, 377
seed tuning, 375
spatial walk off, 381
spectral shift, 370, 380, 381
temporal walk off, 354
threshold gain, 345
tilt & tune theory, 364
tilt filtered spectra, 370
ultra broadband, 363
unseeded, 355, 368
bandwidth, 355, 371
efficiency, 355
waveguide, 350
paraxial approximation, 171, 180, 184
permutation symmetry, 630
phase amplification, 67
phase conjugation, 296, 585
phase matching
acceptance angle, 148, 154
acceptance bandwidth, 148
achromatic, 322
birefringent, 105, 108
collinear, 105–111
compensated, 131
crystal tilt tolerance, 158
distributed, 232
form birefringent, 107
noncollinear, 111–117, 195–198
noncritical, 117
photonic lattice, 139–148
quasi, 118–131
chirped gratings, 236
d_{eff} modulated, 121–131
eigenmode mixing, 581
group velocity matched, 329–331
nonuniform gratings, 235, 579–581
patterned growth, 128
periodically poled, 126
pulse shaping, 580
spectral shaping, 580
total internal reflection, 130
wafer stack, 128
simultaneous processes, 581
tangential, 113–117
temperature tolerance, 158
temperature tuning, 159
thermal disruption, 616
triple tuning, 152
type I, 106
type II, 106
vector diagram, 103
waveguide
Cerenkov, 137
modal, 94, 135
windowing function, 232
phase mismatch
definition, 54
phasor diagram, 58, 118, 120, 132
photonic lattice, 139–148
bandgap, 145
effective index, 143
piezoelectric effect, 627
piezoelectricity, 647
polarization, 3, 11
Poynting Theorem, 40
Poynting vector, 2, 12, 278
walk off, 18–19, 30, 32, 35, 155, 169–181, 190–198, 255, 260

compensated, 267, 283, 648
principal plane, 17–36
propagation
Gaussian beam, 256–260
Gaussian pulse, 215
modeling, 206
propagation equation
biaxial crystal, 184
coefficients, 194
diffractive, 169–185
diffractive & dispersive, 190–198, 311
dispersive, 185–190
tilted beam, 195–198
uniaxial crystal, 181
pyroelectric effect, 627
pyroelectricity, 647

QPM, *see* phase matching, quasi
quantum noise, 208–211
quasi phase matching, *see* phase matching, quasi

radius of curvature, *see* cavity, *see* Gaussian beam
Raman gain, 88
line width, 87
phonon polariton, 88
Stokes shift, 88
Rayleigh range, 85, 205, 273–277, 281–293, 295, 303, 401–405
definition, 7
recirculating frequency doubler, 582
reflection
coefficient, 39
refractive index
hi & lo surfaces, 19
uniaxial, 172
refractive index ellipse, 608
relaxation oscillation, 454
resonator, *see* cavity

S, *see* Poynting vector
$S_\circ$-reference irradiance
definition, 4
second harmonic generation
acceptance bandwidth, 225
achromatic, 322
chirped pulse, 224
Gaussian beam, 260–263
walk off compensated, 267
group velocity matched, 321, 330
recirculating cavity, 582
short pulse, 218–226
efficiency, 220
Gouy phase, 222
group delay dispersion, 222
spatial & temporal structure, 312–315
temporal walk off, 218
self focus, 85
self phase modulation, 84–85, 241
waveguide, 95
self-steepening, 200
separated beams method, *see* d-tensor,measurement
SHG, *see* second harmonic generation
sinc function
definition, 59
slanted pulses, 312, 313, 315
Snell's law of slants, 331
Snell's law, 37
SNLO, 46, 87, 178, 188, 194, 207, 255
2D-cav-LP, 401, 405, 416, 421, 428, 439, 446, 463, 474, 558–561, 563
2D-mix-LP, 263, 265, 268, 272, 277, 279, 280, 282, 286, 288, 583, 685, 692
2D-mix-SP, 241, 315, 331, 685
Bmix, 36, 111, 636, 640, 683, 701
Cavity, 405

GVM, 115, 322, 324, 327
Ncpm, 118, 153
OPG, 349, 350, 364, 374, 379, 385, 396–398
Opoangles, 116, 327
PW-cav-LP, 401, 414, 415, 418–421, 423, 425, 427, 434, 445, 453, 455, 457, 459, 463, 467, 468, 470, 472, 474, 538, 539, 542
PW-mix-BB, 230, 234, 235, 350, 355, 360, 361, 363, 387, 390, 392–395, 398
PW-mix-LP, 62, 65, 70, 72, 73, 78, 83, 94, 288, 583
PW-mix-SP, 217, 221, 224, 226–229, 238, 241, 328, 352, 389, 692
PW-OPO-BB, 210, 546–548, 552–556
PW-OPO-SP, 210, 506, 508, 509, 511, 513, 516, 518, 520, 525–530
Qmix, 111, 152, 158, 606, 635
QPM, 128, 153, 160, 330, 331, 439
RefInd, 21
SPIDER, 238
SPM, *see* self phase modulation
Stokes shift, 88
strain-optic
effect, 609, 624–626
tensor, 609
sum frequency mixing
broadband, 230–234
cw cavity, 411–428
triply resonant, 425–428
wave one resonant, 411–416
wave three resonant, 421–423
waves one & three resonant, 423–425
waves one & two resonant, 416–421
focused beam, 274–279, 288
Boyd & Kleinman, 274–276, 281–287
Gaussian beam, 263–271
imaging, 294
short pulse, 226–228
slanted pulse, 324
windowing function, 232

temperature
bandwidth, 158
tuning, 159
temporal walk off
compensation, 230, 232
tensor
higher order, 609–610
linear electro-optic, 627
piezoelectric, 627
transformation properties, 610–611
thermal
nonuniform heating, 619–623
phase matching disruption, 616
temperature profile calculation, 620–623
thermal conductivity, 606–608
thermal diffusion time, 618
thermal expansion, 600–606
ellipsoid, 605
thermal lensing, 617
thermal resistivity, 606–608
thermal strain tensor, 604
thermal tilt, 618
thermo-optic effect, 623–624
third order effects, *see* $\chi^{(3)}$
threshold power, *see* optical parametric oscillator
tilt angle, 53
tilted beam, 315
transmission
coefficient, 39

uniaxial crystal
    eigenpolarizations, 19
    linear optical properties, 19
    optic axis, 20
    Poynting vector
        walk off, 19, 31
    propagation equation, 192
    refractive index
        o & *e* surfaces, 20

walk off, *see* Poynting vector or group velocity
waveguide
    channel, 91
    d_{eff}, 92
    effective area, 95
    higher order nonlinearity, 95
    modal overlap, 135
    modal phase matching, 94, 135
    modes, 91
    nonlinear mixing, 90–96
    parametric generation, 350
    planar, 94
    self phase modulation, 95
wurtzite, 643

zinc blende, 643
ZZ_B, 709
ZZ_U, 709